EFFECTS OF CAPILLARITY ON THE MECHANICAL STABILITY OF SMALL-SCALE INTERFACES

A Dissertation
Presented to
The Academic Faculty

by

Jie Zheng

In Partial Fulfillment
of the Requirements for the Degree
Doctor of Philosophy in the
George W. Woodruff School of Mechanical Engineering

Georgia Institute of Technology
November 2004

EFFECTS OF CAPILLARITY ON THE MECHANICAL STABILITY OF SMALL-SCALE INTERFACES

Approved by:

Dr. Jeffrey L. Streator, Advisor
School of Mechanical Engineering

Dr. Richard F. Salant
School of Mechanical Engineering

Dr. G. Paul Neitzel
School of Mechanical Engineering

Dr. J. Carlos Santamarina
School of Civil and Environmental Engineering

Dr. J. Carson Meredith
School of Chemical and Biomolecular Engineering

Date Approved:
November 2004

To my family

ACKNOWLEDGEMENT

I would like to begin by expressing my sincere thanks to my research advisor, Dr. Jeffrey L. Streator, who has consistently supported me pursuing my dream. His guidance has been invaluable over the years. I would also like to thank Dr. Richard F. Salant, Dr. G. Paul Neitzel, Dr. J. Carlos Santamarina, and Dr. J. Carson Meredith, for having served in my thesis committee and for their comments and suggestions. Thanks also goes to all of the members of the tribology research group, a special note of appreciation to Dr. Yeyuan Yang, Joseph Huang and Peter Arthur Kottke, for many insightful discussions from which I learned greatly.

I am grateful to the National Science Foundation for sponsoring my research through NSF Grant No. CMS-0200681.

I am indebted to all my family and friends, and especially to my parents for their love and encouragement. I would like to express my warmest thanks to my husband, Jun Li, who has been a constant source of inspiration and strength throughout my study at Georgia Tech.

Thank you!!

TABLE OF CONTENTS

LIST OF TABLE

LIST OF FIGURES

LIST OF SYMBOLS OR ABBREVIATIONS

A_{LV} Area of liquid-vapor interface

$A_{SL_{1,2}}$ Areas of solid-liquid interfaces on bodies 1 and 2

$A_{SV_{1,2}}$ Areas of solid-vapor interfaces on bodies 1 and 2

a Radius of contact area

a^* Dimensionless contact radius, defined as $a^* = a\sqrt{\frac{H}{V_o}}$

a' Alternative dimensionless contact radius, defined as

$$a' = \frac{a}{\left(\frac{R^2\gamma_{LV}\left(\frac{\cos\theta_1 + \cos\theta_2}{2}\right)}{E'}\right)^{1/3}}$$

B Dimensionless parameter, defined as $B = \frac{b^2}{RH}$

b Radius of wetted area

b^* Dimensionless wetted radius, defined as $b^* = b\sqrt{\frac{H}{V_o}}$

b' Alternative dimensionless wetted radius, defined as

$$b' = \frac{b}{\left(\frac{R^2\gamma_{LV}\left(\frac{\cos\theta_1 + \cos\theta_2}{2}\right)}{E'}\right)^{1/3}}$$

c_1 Coefficient in the jump-off condition

c_2 Coefficient in the jump-off condition

$[c_{ij}]$ Matrix of influence coefficients

$[c_{s11}]$ Upper-left sub-matrix in the decomposed matrix of influence coefficients

$[c_{s12}]$ Upper-right sub-matrix in the decomposed matrix of influence coefficients

$[c_{s21}]$ Lower-left sub-matrix in the decomposed matrix of influence coefficients

$[c_{s22}]$ Lower-right sub-matrix in the decomposed matrix of influence coefficients

$E_{1,2}$ Elastic Moduli of bodies 1 and 2

E' Reduced elastic modulus, $\frac{1}{E'} = \frac{1-\nu_1^2}{E_1} + \frac{1-\nu_2^2}{E_2}$

$\hat{E}$ Complete elliptic integral of the second kind

$\underline{F}$ Vector representation of the system equations

F_A Adhesion force

F_A^* Dimensionless adhesion force, defined as $F_A^* = \frac{F_A}{E'\sqrt{HV_o}}$

F_A' Alternative dimensionless adhesion force, defined as $F_A' = \frac{F_A}{2\pi R\gamma_{LV}(\cos\theta_1 + \cos\theta_2)}$

F_p Pull-off force

F_p^* Dimensionless pull-off force, defined as $F_p^* = \frac{F_p}{E'\sqrt{HV_o}}$

F_p' Alternative dimensionless pull-off force, defined as $F_p' = \frac{F_p}{2\pi R\gamma_{LV}(\cos\theta_1 + \cos\theta_2)}$

G Residual in arc length

H Original rigid surface separation

H^* Dimensionless original minimum surface separation, defined as $H^* = H\sqrt{\frac{R}{V_o}}$

H' Alternative dimensionless original minimum surface separation, defined as $H' = \dfrac{H}{\left(\dfrac{R\gamma_{LV}^2 \left(\dfrac{\cos\theta_1 + \cos\theta_2}{2} \right)^2}{E'^2} \right)^{1/3}}$

h Gap between the deformed surfaces

h^* Dimensionless gap between the deformed surfaces, defined as $h^* = \dfrac{h}{H}$

h' Alternative dimensionless gap between the deformed surfaces, defined as $h' = \dfrac{h}{\left(\dfrac{R\gamma_{LV}^2 \left(\dfrac{\cos\theta_1 + \cos\theta_2}{2} \right)^2}{E'^2} \right)^{1/3}}$

$h_{\min}$ The minimum separation between the deformed surfaces

$\{h_{s1}\}$ Vector representation of gap between the deformed surfaces at the nodes in the contact region

$\{h_{s2}\}$ Vector representation of gap between the deformed surfaces at the nodes out of the contact region

$\underline{\underline{J}}$ Jacobin matrix

K Elastic modulus of the solid bodies used in Maugis' paper, $K = \dfrac{4}{3}E'$

$\hat{K}$ Complete elliptic integral of the first kind

m Ratio of contact radius to wetted radius, $m = \dfrac{a}{b}$

N Number of elements inside/outside the contact region on a discretized domain of interest

N_c Dimensionless critical number for the onset of jump-on instability in the interface between two elastic half-spaces

p Pressure distribution

$\{p_{s1}\}$ Vector representation of pressure distribution at the nodes in the contact region

$\{p_{s2}\}$ Vector representation of pressure distribution at the nodes out of the contact region

R Equivalent radius of contacting spheres, $\frac{1}{R} = \frac{1}{R_{s1}} + \frac{1}{R_{s2}}$

$R_{1,2}$ Local principal radii of curvature of the meniscus

R_a Universal gas constant

R_c Radius of a control volume

$R_{s1,2}$ Radii of spheres 1 and 2

r Radial position

r^* Dimensionless radial position, defined as $r^* = \frac{r}{b}$

r' Alternative dimensionless radial position, defined as

$$r' = \frac{r}{\left(\frac{R^2 \gamma_{LV} \left(\frac{\cos\theta_1 + \cos\theta_2}{2} \right)}{E'} \right)^{1/3}}$$

r_K Kelvin radius

$\{r_{s1}\}$ Vector representation of radial positions of nodes in the contact region

$\{r_{s2}\}$ Vector representation of radial positions of nodes out of the contact region

s Arc length

T Absolute temperature

U_E Elastic strain energy

U_S Surface energy

U_T Total free energy stored in the interface

U_T^* Dimensionless system free energy

u Combined elastic deflection of both surfaces

u^* Dimensionless combined elastic deflection of both surfaces, defined as $u^* = \frac{u}{H}$

$\{u_{s1}\}$ Vector representation of combined deflection of both surfaces at the nodes in the contact region

$\{u_{s2}\}$ Vector representation of combined deflection of both surfaces at the nodes out of the contact region

V_m Molar volume

V_o Liquid volume in the bridge

V_o^* Dimensionless liquid volume, defined as $V_o^* = \frac{V_o}{RH^2}$

$V_o^{'}$ Alternative dimensionless liquid volume, defined as

$$V_o^{'} = \frac{V_o}{\left(\frac{R^5 \gamma_{LV}^4 \left(\frac{\cos\theta_1 + \cos\theta_2}{2} \right)^4}{E^{'4}} \right)^{1/3}}$$

w Surface tension used in Maugis' paper, $w = 2\gamma_{LV}$

X Function of η and m for the calculation of B

$\underline{x}$ Vector representation of unknowns

Y Function of m for the calculation of B

$\underline{y}$ Intermediate variable in the arc-length continuation algorithm

$\underline{z}$ Intermediate variable in the arc-length continuation algorithm

Γ Dimensionless parameter, defined as $\Gamma = \dfrac{\gamma_{LV}{}^2 \left(\dfrac{\cos\theta_1 + \cos\theta_2}{2} \right)^2 V_o}{E'^2 H^5}$

Γ_c Critical values of Γ, at which the surfaces first come into contact

Γ_s Critical values of Γ, at which the contacted surfaces separate

Δp Laplace pressure drop across the meniscus

Δp^* Dimensionless wetted radius, defined as $\Delta p^* = \dfrac{\Delta p}{E'} \sqrt{\dfrac{V_o}{H^3}}$

Δr Increment of the radial position on a discretized domain of interest

Δr_{s1} Increment of the radial position in the contact region

Δr_{s2} Increment of the radial position out of the contact region

$\Delta\gamma$ The Dupré energy of adhesion in dry contact

Φ Dimensionless parameter, defined as $\Phi = \dfrac{\Delta\gamma}{\gamma_{LV}(\cos\theta_1 + \cos\theta_2)} - 1$

Ψ Dimensionless parameter, defined as $\Psi = \dfrac{V_o}{RH^2}$

Ψ_c Critical values of Ψ, which determines if jumps will occur at the interface

γ_{S12} Surface energy of solid-solid interface

γ_{LV} Surface tension of liquid-vapor interface

$\gamma_{SL_{1,2}}$ Surface tensions of solid-liquid interfaces on bodies 1 and 2

$\gamma_{SV_{1,2}}$ Surface tensions of solid-vapor interfaces on bodies 1 and 2

δ Interference in Hertz contact theory

$\delta \underline{x}$ Increment of $\underline{x}$

$\delta\Gamma$ Increment of Γ

ε Local equilibrium separation

η Dimensionless parameter, defined as $\eta = \dfrac{2\Delta pb}{E^{'}H}$

$\theta_{1,2}$ Contact angle of liquid on solid surfaces 1 and 2

λ Dimensionless parameter in Maugis' paper, defined as $\lambda = \dfrac{2\sigma_o}{(\pi w K^2 / R)^{1/3}}$

λ_{1-9} Dimensionless factors in the calculation of dimensionless system free energy, are functions of m

μ Dimensionless parameter, defined as $\mu = \left(\dfrac{R\gamma_{LV}{}^2 \left(\dfrac{\cos\theta_1 + \cos\theta_2}{2} \right)^2}{E^{'2}H^3} \right)^{1/3}$

μ_T Tabor parameter, defined as $\mu_T = \left(\dfrac{R\Delta\gamma^2}{E^{'2}\varepsilon^3} \right)^{1/3}$

$\nu_{1,2}$ Poisson's ratios of bodies 1 and 2

σ_o Constant stress around the contact region in Maugis' paper, equals Δp

ϕ Relative humidity

χ Dimensionless parameter, defined as $\chi = \dfrac{\gamma_{LV}^2 \left(\dfrac{\cos\theta_1 + \cos\theta_2}{2} \right)^2 R^{5/2}}{E^{'2}V_o^{3/2}}$

SUMMARY

Interfacial adhesion and friction are significant factors in determining the reliability of small-scale mechanical devices such as with MEMS and the computer head/disk interface (HDI). As the interface spacing becomes smaller, operational failure via stiction has become a growing concern in these systems. Fundamentally, interface failure is related to mechanical instability of the interface caused by capillary effects.

When liquid is present in a small-scale interface, large concave meniscus curvatures often develop at the liquid-vapor interface, leading to negative pressures in the liquid film and large tensile forces on the surfaces. When the elastic restoring force cannot balance the capillary force, the interface will lose its stability and collapse into intimate contact (jump-on). In addition, when the elastic bodies are then pulled away from contact, separation may occur suddenly and is related to another form of instability (jump-off). The jump-on and jump-off behaviors determine the strength of interfacial adhesion.

In this study, the interaction between two elastic bodies coupled via a small liquid bridge was investigated. Geometries of two half-spaces and two sphere contact were considered. Stable equilibrium configurations were determined, and the mechanical stability of the interface was examined. Jump-on and jump-off conditions were given out. Then the theory was applied to study the approach and detachment processes of two elastic spheres in the presence of a liquid bridge. Critical values of the control variables at jump-on and jump-off were found. The pull-off force was calculated as a measure of interfacial adhesion. The results provide insight on some experimental data in the literature.

CHAPTER I

INTRODUCTION

1.1 Background

In microelectromechanical systems (MEMS) and computer head/disk interface (HDI), the desired spacing between solid surfaces is often on the order of a few tens of nanometers. In such confined geometries, any liquid present, such as from lubricants, moisture or contamination, is readily available to bridge two solid surfaces. Large concave meniscus curvatures then develop at the liquid-vapor interface, leading to large adhesive forces. The strong attractive capillary forces cause the solid surfaces to deflect toward each other. Under certain condition, the elastic members may collapse and permanently adhere together causing a device failure. In this vein a "stiction" phenomenon, which is characterized by large adhesion and/or friction forces, is often observed in MEMS and HDI and remains one of the most widespread hazards threatening the reliability of these systems[1-4]. It is believed that the capillary effect of liquid menisci is one of the main sources of the excessive adhesion and friction forces[1-11], and the catastrophic failure can be related to mechanical instability of the interface induced by capillary effects acting in conjunction with the elasticity of the solid bodies[12-16]. Understanding the fundamentals of this phenomenon is essential for the prevention of failure in small-scale devices.

1.2 Mechanical Collapse by Capillary Force

In MEMS, microstructures are often fabricated on a silicon substrate by deposition and selective etching of multiple layers of structural and sacrificial films. After etch, the structures are rinsed and dried to remove the etchant and etch products and to release the suspended members. During the process, capillary forces can become large enough to bring the suspended members in contact with their underlying substrate. After complete drying, some of the members remain pinned to the substrate rendering them unusable[17]. In 1993, Mastrangelo and Hsu[12] first pointed out that the catastrophic failure involves mechanical collapse and intersolid adhesion of the structures caused by capillary forces. They considered the equilibrium between the adhesion force and elastic restoring force using an energy function formulation that includes the surface energy and elastic energy of the deformed member. Mechanical collapse occurs for those values of control parameters at which a local minimum in the energy disappears by combining with a local maximum[18-20]. They thus specified a critical elastocapillary number and a peel number to determine whether mechanical collapse and intersolid pinning will occur. The numbers set up physical bounds on the dimensions of the elastic member for prevention of failure. They experimentally demonstrated the presence of the failure threshold by constructing an array of progressively weaker suspended elements followed by examination of the sticking condition[13]. They claimed that if the stiffness of the microstructure is high enough, both mechanism can be prevented.

By the end of the last century, in the magnetic recording industry, fly/stiction failure has become a great concern as the head-disk spacing becomes smaller[15,16,21,22]. This failure mode is a special type of head-disc interface stiction that occurs only after a head

has flown over a disc and parked at the laser textured landing zone. It is characterized by exceptional large stiction forces, which flatten the texture bumps. Gui and Marchon[15] related fly/stiction to the mechanical instability of a head-disc interface triggered by the excessive accumulation of liquids at the interface, which happens when the head picks up liquid during flying and transfers to the laser textured landing zone after landing. They conceptually showed how an interface may collapse as the contacting asperities deforms under capillary force and applied load. Later, Schouterden et. al.[16] gave a better description on the functional collapse of the surface texture by showing the variations of capillary force and the elastic response of contacting bumps with surface separation at different liquid volumes and different bump heights. They found that a minimum bump height is required for the laser texture to be effective and for a given bump height, as the liquid volume increases, the interface may collapse spontaneously.

It should be pointed out that the collapse in a head-disc interface results from surface deformation. In MEMS, on the other hand, the focus is on the structural deflection of the flexible members (e.g., bending of a cantilever beam). However, for those microstructures which work at close contact conditions, such as engaging micro-gears, the situation is more like what is in the head-disc interface. Surface deformation due to bulk elasticity becomes significant compared to surface separation. Capillary force in conjunction with the bulk elasticity of the solids may cause the interface to collapse, greatly increasing the contact area and hence create extreme large stiction forces. The problem cannot be avoided simply by increasing the stiffness of microstructures. It has an impact on many contact/adhesion related areas, and thus requires an in-depth investigation. No theoretical study in the literature has addressed the mechanical

instability induced by capillary force except the early works mentioned above. Although energy method proposed by Mastrangelo and Hsu[12] is helpful, the authors did not consider the bulk elasticity of the structures. The theoretical descriptions presented by Gui and Marchon[15] and Schouterden et al.[16] are rather conceptual. Therefore, a more rigorous theory is needed to elucidate the complex effects of capillarity on the mechanical instability of a micro/nano-scale interface.

1.3 Studies on Mechanical Instability in Dry Contact

As limited attention has been paid to the mechanical instability caused by capillary force and solid elasticity, such an effect has been recognized in dry contact for a while, where surface forces (e.g., van der Waals) cause the solid surfaces to jump into or out of contact[23-34,39]. Studies on the mechanical instability in dry contact have yielded some interesting and important results.

In 1970s, JKR theory of elastic contact[23,24] predicted an instability when the contacted bodies were pulled off by tensile load. In the load-area curve, the tensile load reaches a maximum at a non-zero contact area. At this point, the surfaces jump out of contact. The maximum tensile load is defined as the "force of adhesion", which is also called the "pull-off force" and is a measure of surface adhesion. Later, DMT model[25,51] predicted a different pull-off force, and no instability was found during the pull-off process. The discrepancy was explained by Tabor[33]. He noted the transition from the JKR approximation to the DMT approximation (see Table 1.1) when a dimensionless parameter (Tabor parameter), which measures the relative strength of surface energy and

Table 1.1 Features of different elastic contact theories.

	Hertz	JKR	DMT
Contact radius	$a = \sqrt{R\delta}$	Zero interference: $a = \left(\frac{2\pi R^2 \Delta\gamma}{E'}\right)$ Zero load: $a = \left(\frac{9\pi R^2 \Delta\gamma}{2E'}\right)$	Zero interference: 0 Zero load: $a = \left(\frac{9\pi R^2 \Delta\gamma}{2E'}\right)$
Contact profile	$h = \frac{a^2}{\pi R}[\sqrt{\rho^2 - 1} + (\rho^2 - 2)\cos^{-1}\frac{1}{\rho}]$ Where $\rho = r/a > 1$ 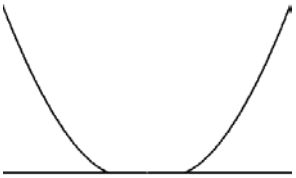	$h = \left(\frac{8a\Delta\gamma}{\pi E'}\right)^{1/2}\cos^{-1}\frac{1}{\rho} + \frac{a^2}{\pi R}[\sqrt{\rho^2 - 1} + (\rho^2 - 2)\cos^{-1}\frac{1}{\rho}]$ Where $\rho = r/a > 1$ 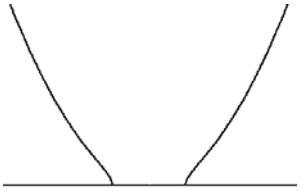	$h = \frac{a^2}{\pi R}[\sqrt{\rho^2 - 1} + (\rho^2 - 2)\cos^{-1}\frac{1}{\rho}]$ Where $\rho = r/a > 1$ 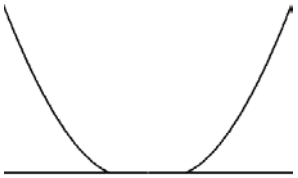
Pull-off force	0	Fixed-grips: $\frac{5}{6}\pi R\Delta\gamma$ Fixed-load: $\frac{3}{2}\pi R\Delta\gamma$	$2\pi R\Delta\gamma$

elasticity, decreases. This transition is then confirmed by Maugis with an analytical solution using Dugdale model[26].

In 1988, Pethica and Sutton[27] discovered that, for small separations and attractive forces, the surfaces could jump into contact owing to the bulk elasticity of two solids. They did a molecular dynamic simulation to the approach of two f.c.c. planes. Each half-crystal was divided into a inner region of 11 atomic lattices free to move under the action of van der Waals forces exerted by other planes, and a outer rigid shoulder which is not relaxed. When a regular displacement was imposed on the shoulder, the corresponding force and energy of interaction and surface separation were determined. Calculations show steep variations in these parameters, indicating the jump. The same phenomenon was observed by Smith et al.[28] with other interaction potential and has been termed as "adhesion avalanche"[28,29].

In 1992, Attard and Parker[30] calculated the deformation and adhesion of elastic bodies interacting via Lennard-Jones pressure by self-consistently solving the elasticity equations. They found that for soft bodies with high surface energy, the precontact deformation is significant. An instability in the force-deformation relation means that the surfaces jump into contact from a finite separation. The jump is an inherent property of the solids and occurs no matter how rigidly the position of the bodies is controlled. By taking a stability criterion, which is the response to the perturbation must be smaller than the perturbation itself for a stable deformation, they derived an analytic expression for the critical separation at which the surfaces jump into contact. They further pointed out that the jump is the origin of adhesion hysteresis[31].

In 1997, another paper on numerical computations of the adhesion of contacting elastic spheres was published by Greenwood[32]. Again, the Lennard-Jones force law and the elastic equations for a half-space are solved self-consistently. The calculations show that, for values of Tabor parameter[33] greater than about unity, the load-approach curve becomes S-shaped or even more convoluted, so that in a fixed-grips apparatus, jumps will occur when the tangent to the curve becomes vertical.

The self-consistent calculation was repeated by Feng[34] in 2000 with more efficient computational methods. It confirmed the observation of Greenwood[32] that turning points appear on the "S-shaped" load-approach curves for large values of Tabor parameter, which correspond to hysteresis discussed by Attard and Parker[30,31]. Passing through a turning point, where the slope of the curve goes to infinity, corresponds to a change of relative stability of a system[35]. With an arc-length continuation algorithm[36], the hysteretic solution branches were tracked around turning points to accurately determine jumping-on and jumping-off behavior of contacting surfaces. With increasing values of the Tabor parameter, the parameters associated with pull-off force and jump-off are found to be well approximated by the JKR model.

In summary, to study the mechanical instability of interface, one must fully investigate the influence of surface forces on the deformation and adhesion of contacting elastic bodies. The load-approach and load-area curves provide information on jumps. When only bulk elasticity of solids is considered (a fixed-grips analysis), jumps are predicted whenever vertical tangents arise.

1.4 Effects of Capillary Force on Elastic Contact

Capillary force, as an important surface force contributing the most to interfacial adhesion[38], has complex effects on elastic deformation and adhesion of contacting bodies. Experimental results on crossed mica cylinders[39-41] have shown that a liquid meniscus can change the shape of the deformed surfaces from a JKR profile[23,24] to a Hertzian profile[24] (see Table 1.1) and significantly affect the pull-off force. Few theoretical studies have attempted to interpret these experimental results.

In 1990, Fogden and White[42] incorporated capillary condensation into a very general "physically consistent approximate theory", through which they obtained a "generalized Hertz theory". Their numerical results show that for small, high modulus spheres in contact with vapor near saturation, the force of adhesion assumes the Laplace pressure force for rigid spheres ($2\pi R\gamma_{LV}(\cos\theta_1+\cos\theta_2)$), whereas for larger softer spheres at relatively low vapor pressures, the force of adhesion is in precisely the form of JKR theory with the surface energy of the solid replaced by that of the liquid ($\frac{3}{2}\pi R\gamma_{LV}$).

Later, Maugis and Gauthier-Manuel[43] applied a fracture mechanics analysis using Dugdale model to the elastic contact in presence of liquid meniscus. Analytical solutions for the load, the penetration and the profile of the air gap were obtained. The results show that when the size of the meniscus increases, there is a continuous transition from the JKR approximation[23,24] to the DMT approximation[25,51] (See Table 1.1). They demonstrated the similarity of their results to those of Fogden and White[42], and showed a good agreement between the theoretical prediction and the experimental results, using one or two adjusting parameters.

The model of Fogden and White[42] and that of Maugis and Gauthier-Manuel[43] treat capillary condensation around a contact. A constant Kelvin radius (or constant Laplace pressure) is assumed for a given humidity. As a result, no coupling occurs between the capillary force and the elastic deformation.

Capillary effects can be quantified by appealing to the well-known Laplace-Young equation, which is given as[44]:

$$\Delta p = \gamma_{LV}\left(\frac{1}{R_1}+\frac{1}{R_2}\right) \tag{1.1}$$

where Δp is the pressure drop across the meniscus, γ_{LV} is the liquid-vapor surface tension, and $R_{1,2}$ are the local principal radii of curvature of the meniscus. The capillary force is then calculated from the pressure drop and the wetted solid area. The values of $R_{1,2}$ greatly depend on the interface geometry. Therefore, when taking into account the elasticity of the structure, it is clear that there is a coupling between the elastic deformation and the capillary force. The surfaces deform according to the capillary force, which is, in turn, altered by the surface deformations.

Makhovskaya and Goryacheva[45] considered this coupling effect in their investigation on the contact of a rigid punch and an elastic half-space with a meniscus of fluid between them. They found out that the capillary forces substantially influence the contact characteristics of the elastic bodies, and in turn, the elastic properties of the interacting bodies have a substantial influence on the capillary-driven adhesion between these bodies. The effect of capillarity is stronger for liquid with higher surface tension and solid bodies with smaller elastic moduli and lager radius of curvatures. Assuming a

fixed liquid volume in the interface, they predicted an adhesion force dependent on the liquid volume.

The dependency of interfacial adhesion on liquid volume has been revealed by the experimental studies on stiction[7,8,16,21,22]. When capillary condensation is taken as the source, it has been found that stiction increases with increasing relative humidity of the atmosphere. In practice, an environment usually has a constant (or slowly varying) relative humidity, which implies a constant Kelvin radius according to the Kelvin equation[44]:

$$\phi = \exp\left\{-\frac{\gamma_{LV} V_m}{R_a T r_K}\right\} \tag{1.2}$$

where ϕ is the relative humidity, γ_{LV} is the liquid-vapor surface tension, V_m is the molar volume, R_a is the universal gas constant, T is the absolute temperature and r_K is the Kelvin radius. Therefore, a fixed Kelvin radius rather than a fixed liquid volume is often assumed in the theoretical studies, like Fogden and White[42] did in their investigation. However, with this assumption, one cannot apply the theory to explain the effect of liquid transfer and accumulation, which exhibit in fly/stiction failure, or to describe the state change of interfaces in MEMS devices during the rinse-and-dry process. In fact, after the condensation has occurred, when surfaces are pressed together or pulled apart, the volume of the condensate is essentially constant[4]. This is because the process of wetting and spreading along with the elastic response of the surface, which give rise to the stiction, generally happen over a time scale that is much shorter than that required for full thermodynamic equilibrium. Thus the actual, operating radius of curvature of the meniscus developed in the interface is determined by the amount of liquid found and the

interface geometry, rather than by the relative humidity. For example in the case of water at 25.0°C (298.15 K), with $\gamma_{LV} = 72.0$ mN/m[46], $V_m = 18.069$ cm^3/mol[47], $R_a = 8.3145$ J/mol-K[46], one gets $\gamma_{LV} V_m / (R_a T) = 0.525$ nm. Therefore to maintain spherical meniscus having a radius of curvature of, say, 1 mm, such as might be the case in a common capillary tube, the Kelvin equation predicts that the required relative humidity is exp[(–0.525×10^{-9}m)(2/.001m)] = 0.99999895, or virtually 100%. In contrast, experience tells us that a meniscus may persist for days in a capillary tube under typical ambient humidity which is much lower (e.g., 40% to 80% RH). Based on this argument, the assumption of a fixed liquid volume in the interface seems more appropriate for theoretical studies on stiction problem.

1.5 Scope of the Present Work

The aim of this research is to provide a systematic description on the effect of liquid meniscus on the contact between elastic bodies. First, an analysis is performed on the case of two elastic half-spaces. Then the interaction between two elastic spheres is considered. The role of various geometric and material properties on interface instability and pull-off force is investigated. The results of this study should assist in the design of components to control interfacial adhesion and friction and reduce the risk of stiction failure.

CHAPTER II

A LIQUID BRIDGE BETWEEN TWO ELASTIC HALF-SPACES

2.1 Equilibrium Configuration without Contact

Consider two elastic semi-infinite spaces initially separated by a uniform gap, H (Figure 2.1). If the surfaces are perfectly flat and smooth, when a small volume of liquid, V_o, is introduced into the interface, it will wet a circular area of radius b. For small H, a highly curved meniscus is formed at the liquid-air boundary. The pressure drop across the meniscus, Δp, can be determined from the Laplace-Young equation if the radii of curvature of the meniscus are known. Meanwhile, we know that in the absence of solid-solid contact, the normal (gage) pressure exerted on each surface satisfies

$$p(r) = \begin{cases} -\Delta p, & 0 \le r \le b \\ 0, & r > b \end{cases} \tag{2.1.1}$$

Here, the effect of gravity is neglected because, in most cases of interest, H is so small that the hydrostatic pressure is negligible when compared to the Laplace pressure. For example, assuming a perfectly wetting condition, water in a 100 nm gap will create 1.5 MPa pressure drop across the meniscus according to Laplace-Young equation[44], while the hydrostatic pressure is less than 1 mPa. The effect of surface tension at the periphery of the wetted area is also neglected. This surface tension force can be estimated by $2\pi b\gamma_{LV}$, while the force contributed by the Laplace pressure drop can be estimated by

$\pi b^2 \Delta p = \frac{\pi b^2 \gamma_{LV} (\cos\theta_1 + \cos\theta_2)}{h(b)}$, where $\theta_{1,2}$ are the liquid-solid contact angles at two solid surfaces, and $h(b)$ represents the surface separation at the edge of the wetted area. Since, $\theta_{1,2}$ are usually close to zero, the ratio of the surface tension force to the Laplace pressure force is mainly determined by $\frac{h(b)}{b}$. For most interfaces of interest, b is very much greater than $h(b)$, therefore, the surface tension force is negligible when compared with the Laplace pressure force.

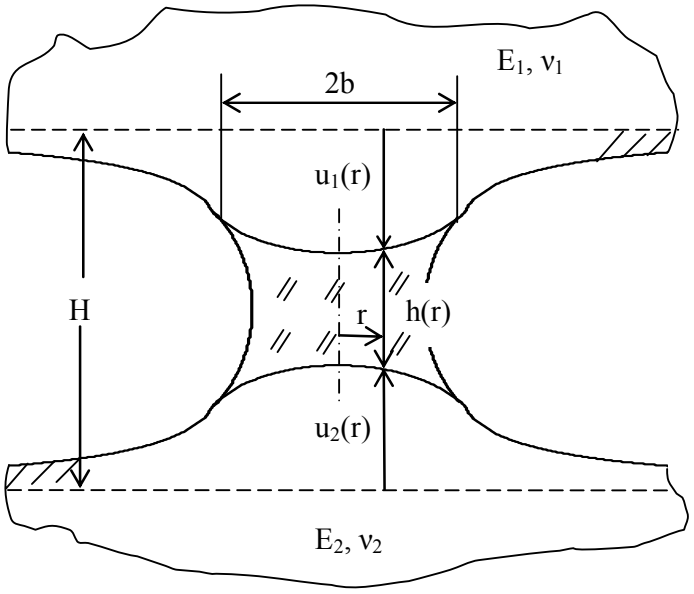

Figure 2.1 Schematic of the deformed interface between two elastic half-space connecting by a liquid bridge of volume V_o, without solid-solid contact.

Assuming there is no plastic deformation, the combined elastic deflection, $u(r)$, of both surfaces caused by this pressure is given by[24]

$$u(r)=\begin{cases}\dfrac{4\Delta pb}{\pi E'}\hat{E}\left(\dfrac{r}{b}\right), & r\le b\\ \dfrac{4\Delta pr}{\pi E'}\left[\hat{E}\left(\dfrac{b}{r}\right)-\left(1-\dfrac{b^2}{r^2}\right)\hat{K}\left(\dfrac{b}{r}\right)\right], & r>b\end{cases} \tag{2.1.2}$$

where, $\hat{E}(r/b)$ is the complete elliptic integral of the second kind with modulus (r/b). $\hat{K}(b/r)$ is the complete elliptic integral of the first kind with modulus (b/r). And

$$\frac{1}{E'}=\frac{1-\nu_1^2}{E_1}+\frac{1-\nu_2^2}{E_2} \tag{2.1.3}$$

where $E_{1,2}$ and $\nu_{1,2}$ are the elastic moduli and Poisson's ratios, respectively, of the two half-spaces. The gap $h(r)$ between the deformed surfaces can be represented in the form

$$h(r)=H-u(r) \tag{2.1.4}$$

Therefore, once the pressure drop, Δp, and the radius of wetted area, b, are determined, the interfacial configuration is known.

If we assume that the volume of the liquid bridge remains fixed, then

$$V_o=\int_0^b 2\pi r h(r)dr=\int_0^b 2\pi r(H-u(r))dr \tag{2.1.5}$$

Using equation (2.1.2) in (2.1.5) and integrating yields

$$V_o=\pi Hb^2-\frac{16}{3E'}\Delta pb^3 \tag{2.1.6}$$

The total free energy stored in the interface is the sum of the surface energy (U_S) and elastic strain energy (U_E):

$$U_T=U_S+U_E \tag{2.1.7}$$

For elastic deformation, the increase of the system elastic energy equals the work done by an external force. Therefore the elastic strain energy can be determined by

$$U_E = \frac{1}{2}\int_0^b 2\pi r(-p(r))u(r)\,dr \tag{2.1.8}$$

Substituting equations (2.1.1) and (2.1.2) into equation (2.1.8) gives

$$U_E = \frac{8}{3E'}\Delta p^2 b^3 \tag{2.1.9}$$

The surface energy consists of the energy at the solid-vapor, solid-liquid and liquid-vapor interfaces, so that

$$U_S = A_{SV_1}\gamma_{SV_1} + A_{SV_2}\gamma_{SV_2} + A_{SL_1}\gamma_{SL_1} + A_{SL_2}\gamma_{SL_2} + A_{LV}\gamma_{LV} \tag{2.1.10}$$

where γ_{SV}, γ_{SL} and γ_{LV} are, respectively, the surface tension of the solid- vapor, solid-liquid and liquid- vapor interfaces, while A_{SV}, A_{SL} and A_{LV} are the corresponding areas. The subscripts 1 and 2 refer to the upper and lower surfaces respectively. Taking R_c as the radius of a control volume, the areas of the solid-vapor and solid-liquid interfaces are given by

$$A_{SL_1} = A_{SL_2} = \pi b^2 \tag{2.1.11}$$

$$A_{SV_1} = A_{SV_2} = \pi(R_c{}^2 - b^2) \tag{2.1.12}$$

The liquid-vapor meniscus area (A_{LV}) can be neglected because the gap H is assumed to be very small compared to the wetted radius, b. The surface energy is then given by

$$U_S = \pi(R_c{}^2 - b^2)(\gamma_{SV_1} + \gamma_{SV_2}) + \pi b^2(\gamma_{SL_1} + \gamma_{SL_2}) \tag{2.1.13}$$

and the total free energy stored in the interface is expressed as

$$U_T = \pi(R_c{}^2 - b^2)(\gamma_{SV_1} + \gamma_{SV_2}) + \pi b^2(\gamma_{SL_1} + \gamma_{SL_2}) + \frac{8}{3E'}\Delta p^2 b^3 \tag{2.1.14}$$

A stable equilibrium configuration is that which minimizes the total free energy for the given liquid volume (V_o). By computing the free energy corresponding to all

provisional equilibrium configurations, as represented by all combinations of Δp and b consistent with a given liquid volume (V_o) and with the deformation relations (2.1.2), the actual equilibrium state can be determined.

For convenience, we now introduce a dimensionless parameter, η, such that

$$\eta = \frac{2\Delta p b}{E' H} \tag{2.1.15}$$

Since

$$h_{\min} = H - u(0) = H - \frac{2\Delta p b}{E'} = H(1-\eta) \tag{2.1.16}$$

the parameter η can be used to indicate the extent of surface approach. When $\eta = 0$, the surfaces are at the original separation, H, while, when $\eta = 1$, the surfaces come into point contact.

Using η to replace $\frac{2\Delta p b}{E' H}$ in equation (2.1.6), we get

$$V_o = \pi H(1 - \frac{8}{3\pi}\eta) b^2 \tag{2.1.17}$$

So

$$b = \sqrt{\frac{V_o}{\pi H(1 - \frac{8}{3\pi}\eta)}} \tag{2.1.18}$$

Then

$$\Delta p = \frac{\eta H E'}{2b} = \frac{1}{2} \frac{\eta H E'}{\sqrt{\frac{V_o}{\pi H(1 - \frac{8}{3\pi}\eta)}}} \tag{2.1.19}$$

Substituting equations (2.1.18) and (2.1.19) into equation (2.1.14), we get the total free energy as a function of η:

$$U_T = \pi R_c^{\,2}(\gamma_{SV_1} + \gamma_{SV_2}) - \frac{\left[(\gamma_{SV_1} - \gamma_{S_1L}) + (\gamma_{SV_2} - \gamma_{SL_2})\right]V_o}{H(1-\frac{8}{3\pi}\eta)} + \frac{2}{3}E'H^2\eta^2\sqrt{\frac{V_o}{\pi H(1-\frac{8}{3\pi}\eta)}} \tag{2.1.20}$$

Assuming the validity of Young's equation[44], we have

$$\gamma_{SV} - \gamma_{SL} = \gamma_{LV}\cos\theta \tag{2.1.21}$$

where θ is the contact angle of the liquid at the surfaces. Using this relation, the total free energy may be written as

$$U_T = \pi R_c^{\,2}(\gamma_{SV_1} + \gamma_{SV_2}) - \frac{\gamma_{LV}(\cos\theta_1 + \cos\theta_2)V_o}{H(1-\frac{8}{3\pi}\eta)} + \frac{2}{3}E'H^2\eta^2\sqrt{\frac{V_o}{\pi H(1-\frac{8}{3\pi}\eta)}} \tag{2.1.22}$$

For convenience, we now define a dimensionless system free energy U_T^* according to

$$U_T^* = \frac{U_T - \pi R_c^{\,2}(\gamma_{SV_1} + \gamma_{SV_2})}{\sqrt{\pi}E'H^{3/2}V_o^{1/2}} = \frac{\frac{2}{3\pi}\eta^2}{(1-\frac{8}{3\pi}\eta)^{1/2}} - 2\sqrt{\frac{\Gamma}{\pi}}\frac{1}{(1-\frac{8}{3\pi}\eta)} \tag{2.1.23}$$

where the dimensionless parameter Γ, defined as

$$\Gamma = \frac{\gamma_{LV}^{\,2}\left(\frac{\cos\theta_1 + \cos\theta_2}{2}\right)^2 V_o}{E'^2H^5} \tag{2.1.24}$$

provides a measure of the relative effects of capillarity and elasticity.

It can be seen that U_T^* depends only on η and Γ, where Γ specifies the condition of the interface and η represents the response. As an indicator of a provisional non-contact configuration, η may take any value between zero to one. However only a value that (locally) minimizes the dimensionless free energy U_T^*, represents an equilibrium configuration. For a given value of Γ, the dimensionless system free energy (U_T^*) is plotted as a function of η in Figure 2.2, where several curves are shown at different values of Γ.

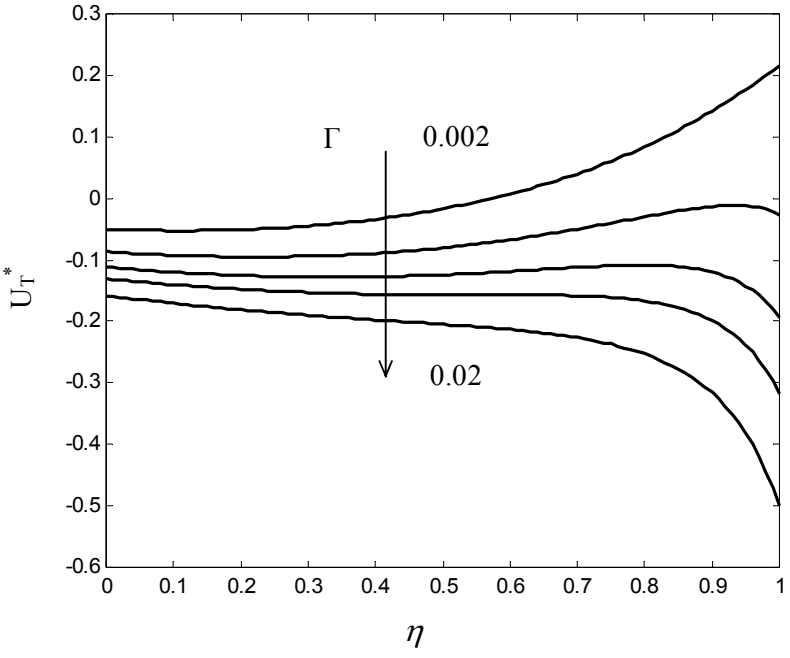

Figure 2.2 Dimensionless total free energy for all provisional equilibrium configurations of the interface between two elastic half-space before solid-solid contact appears. Curves are shown for different values of Γ, from top to bottom: 0.002, 0.006, 0.01, 0.0136, 0.02.

At a stable equilibrium, the dimensionless free energy U_T^* reaches a minimum, at which point $\frac{dU_T^*}{d\eta} = 0$ and $\frac{d^2U_T^*}{d\eta^2} > 0$. Differentiating equation (2.1.23), we get

$$\frac{dU_T^*}{d\eta} = -\frac{16}{3\pi}\sqrt{\frac{\Gamma}{\pi}}\left(1-\frac{8}{3\pi}\eta\right)^{-2} + \frac{4}{3\pi}\eta\left(1-\frac{8}{3\pi}\eta\right)^{-1/2} + \frac{8}{9\pi^2}\eta^2\left(1-\frac{8}{3\pi}\eta\right)^{-3/2} \tag{2.1.25}$$

and

$$\frac{d^2U_T^*}{d\eta^2} = -\frac{256}{9\pi^2}\sqrt{\frac{\Gamma}{\pi}}\left(1-\frac{8}{3\pi}\eta\right)^{-3} + \frac{4}{3\pi}\left(1-\frac{8}{3\pi}\eta\right)^{-1/2} + \frac{32}{9\pi^2}\eta\left(1-\frac{8}{3\pi}\eta\right)^{-3/2} + \frac{32}{9\pi^3}\eta^2\left(1-\frac{8}{3\pi}\eta\right)^{-5/2} \tag{2.1.26}$$

After setting the RHS of equation (2.1.25) to zero and simplifying, we obtain the following condition on η for equilibrium

$$\eta^2\left(1-\frac{2}{\pi}\eta\right)^2\left(1-\frac{8}{3\pi}\eta\right) = \frac{16\Gamma}{\pi} \tag{2.1.27}$$

For this equation to be stable, equation (2.1.26) requires

$$\eta < 0.5577 \tag{2.1.28}$$

The solution space of equation (2.1.27) for $0 \le \eta \le 1$ is plotted in Figure 2.3, where η_{eq} represents the value of η satisfying equation (2.1.27) for a given value of Γ. When η_{eq} is less than 0.5577, it is associated with a local minimum free energy and therefore represents a stable equilibrium configuration.

When the equilibrium configuration is found, we can calculate b and Δp at equilibrium by substituting η_{eq}, E', H and V_o into equation (2.1.18) and (2.1.19),

respectively. We now define a non-dimensional equilibrium wetted radius and a non-dimensional equilibrium pressure drop as

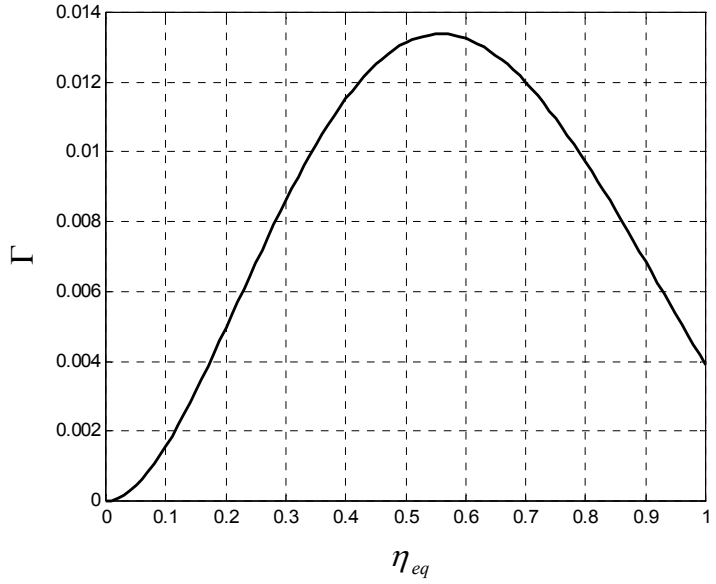

Figure 2.3 The solution space of equation (2.1.27) in the range of $0 \le \eta \le 1$, where η_{eq} represents the value of η satisfying equation (2.1.27) for a given value of Γ.

$$b_{eq}^{*} = b_{eq}\sqrt{\frac{H}{V_o}} = \sqrt{\frac{1}{\pi(1-\frac{8}{3\pi}\eta_{eq})}} \tag{2.1.29}$$

$$\Delta p_{eq}^{*} = \frac{\Delta p_{eq}}{E'}\sqrt{\frac{V_o}{H^3}} = \frac{1}{2}\eta_{eq}\sqrt{\pi(1-\frac{8}{3\pi}\eta_{eq})} \tag{2.1.30}$$

Figure 2.4 shows the dependence of Δp_{eq}^{*} and b_{eq}^{*} on Γ. Both Δp_{eq}^{*} and b_{eq}^{*} increase with Γ.

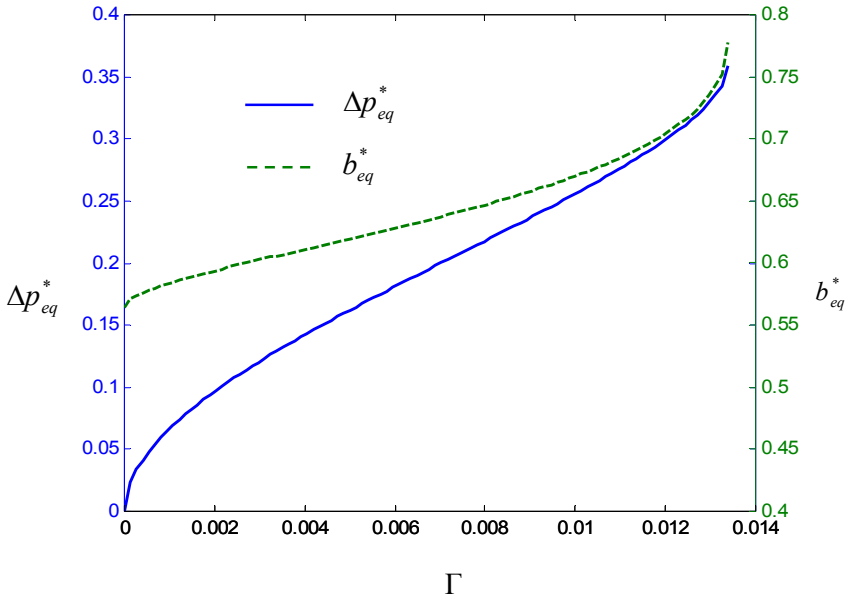

Figure 2.4 Variations of dimensionless equilibrium pressure drop, Δp^*_{eq}, and wetted radius, b^*_{eq}, with Γ, for the interface between two elastic half-spaces before solid-solid contact occurs.

It is worth noting that equation (2.1.27) can be written as

$$\eta_{eq} = \frac{4\sqrt{\Gamma}}{\sqrt{\pi(1-\frac{8}{3\pi}\eta_{eq})}}\frac{1}{(1-\frac{2}{\pi}\eta_{eq})} \tag{2.1.31}$$

Then using this result in (2.1.19) gives

$$\Delta p_{eq} = 2E'H\sqrt{\frac{H}{V_o}}\frac{\sqrt{\Gamma}}{(1-\frac{2}{\pi}\eta_{eq})} = \frac{\gamma_{LV}(\cos\theta_1+\cos\theta_2)}{H(1-\frac{2}{\pi}\eta_{eq})} \tag{2.1.32}$$

Now using (2.1.2) and (2.1.4), the surface separation at the liquid-solid contact line is given by

$$h_{eq}(b_{eq}) = H - 2u(b_{eq}) = H - \frac{2}{\pi}\eta_{eq}H = H(1-\frac{2}{\pi}\eta_{eq}) \tag{2.1.33}$$

So, from (2.1.31) we have

$$\Delta p_{eq} = \frac{\gamma_{LA}(\cos\theta_1 + \cos\theta_2)}{h_{eq}(b_{eq})} \tag{2.1.34}$$

Equation (2.1.34) is often used in the literature[10,45,48] to quantify the capillary effects in interfacial adhesion. It can be derived from the Laplace-Young equation by assuming a circular shape for meniscus with contact angles $\theta_{1,2}$, ignoring any deviations from parallelism between the surfaces. Here we get exactly the same result from an energy analysis.

With b and Δp, the adhesion force at equilibrium, F_{Aeq}, can be easily computed from

$$F_{Aeq} = \pi b_{eq}^2 \Delta p_{eq} \tag{2.1.35}$$

when there is no solid-solid contact. We then define the dimensionless equilibrium adhesion force, F_{Aeq}^*, as

$$F_{Aeq}^* = \frac{F_{Aeq}}{E'\sqrt{HV_o}} = \pi b_{eq}^{*2} \Delta p_{eq}^* \tag{2.1.36}$$

The variation of F_{Aeq}^* with Γ is shown in Figure 2.5. It can be seen that F_{Aeq}^* increases with Γ monotonically and the slope of the curve increases quickly when Γ is larger than 0.012. When Γ reaches 0.01336, the tangent of the curve is almost vertical.

If we define the dimensionless radial variable, r^* and combined surface deflection, u^* as

$$r^* = \frac{r}{b} \tag{2.1.37}$$

$$u^* = \frac{u}{H} \tag{2.1.38}$$

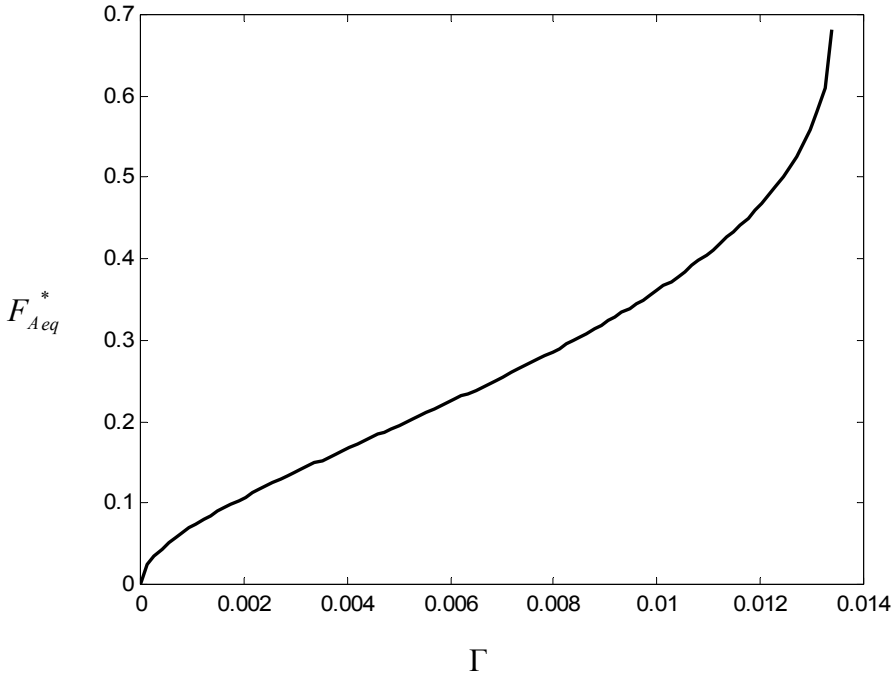

Figure 2.5 Variations of dimensionless equilibrium adhesion force, F^*_{Aeq}, with Γ, for the interface between two elastic half-spaces before solid-solid contact occurs.

then, from equation (2.1.2), the dimensionless equilibrium combined surface deflection u^*_{eq} can be written as

$$u^*_{eq}(r^*) = \begin{cases} \dfrac{2\eta_{eq}}{\pi}\hat{E}(r^*), & r^* \le 1 \\ \dfrac{2\eta_{eq}}{\pi}\left[\hat{E}\left(\dfrac{1}{r^*}\right) - \left(1 - \dfrac{1}{r^{*2}}\right)\hat{K}\left(\dfrac{1}{r^*}\right)\right], & r^* \ge 1 \end{cases} \tag{2.1.39}$$

The dimensionless equilibrium gap, h^*_{eq}, is thus given by

$$h^*_{eq} = \frac{h_{eq}}{H} = 1 - u^*_{eq} \tag{2.1.40}$$

Various gaps are shown in Figure 2.6. The curves are associated with different values of Γ.

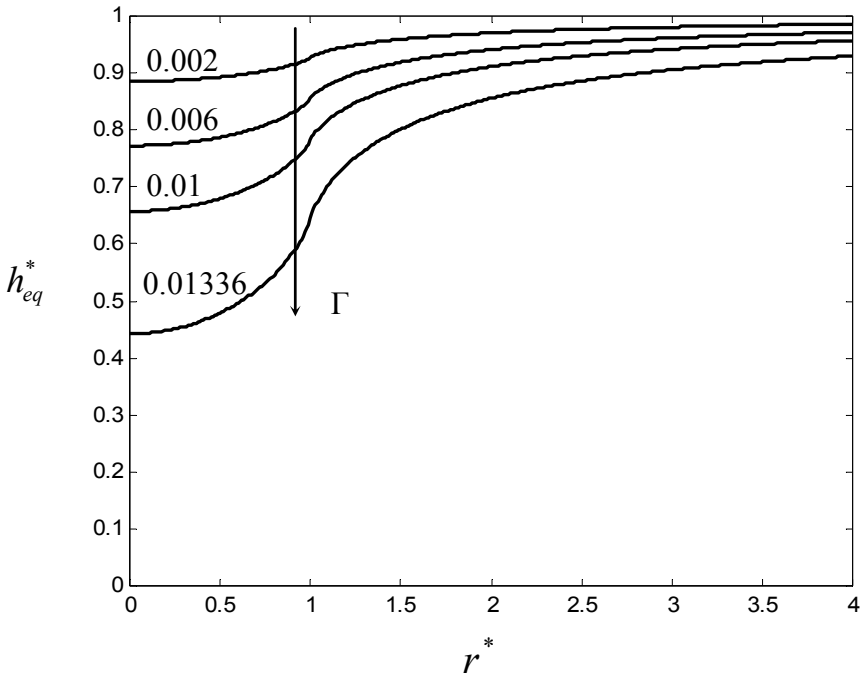

Figure 2.6 Profile of the dimensionless equilibrium gap between two elastic half-spaces before contact, for various Γ.

The above analysis shows that all dimensionless equilibrium parameters of the interface can be expressed in terms of η_{eq}, which itself is determined solely by the value of Γ (see equation 2.1.27). Therefore, the non-dimensionalized system has only one degree of freedom with Γ as the control variable.

2.2 Jump-on Condition

Inequality (2.1.28) determines an upper bound for equilibrium surface approach ($\eta_{eq} < 0.5577$). Figure 2.6 shows what happens when the original gap H is gradually reduced, which corresponds to increasing Γ (see equation (2.1.24)). However, when $\Gamma = 0.01336$, the maximum surface deflection reaches the limit, $0.5577H$. No curve is shown beyond that. One may wonder what happens when Γ keeps increasing. Figure 2.5 shows that the tangent of the $F_A^* \sim \Gamma$ curve becomes vertical when Γ reaches 0.01336. In a fixed-grips (i.e., controlled displacement) test, this means jump will occur at that point[32].

From Figures 2.2 and 2.3 we can clearly see how the interface becomes unstable as Γ increases. It can be seen that when the dimensionless parameter Γ takes on different values, the character of the solution of equation (2.1.27) changes. When $\Gamma < 0.00392$, there is only one η_{eq} in the range from 0 to 1 (Figure 2.3). This value corresponds to a local and global minimum in the total free energy figure (Figure 2.2). When $0.00392 \le \Gamma < 0.01336$, there are two values of η_{eq} in the range, corresponding to a local maximum and a local minimum in Figure 2.2, respectively. When $\Gamma = 0.01336$ (@ $\eta_{eq} = 0.5577$), the local maximum and the local minimum merge to an inflection point. A global minimum appears at η=1, which indicates a state with solid-solid contact. At the inflection point, the equilibrium is unstable. That is, whenever there is a disturbance causing a small increase in η beyond η_{eq}, the system will "slide down" to the point of global minimum free energy ($\eta_{eq} = 1$) meaning that the solid surfaces jump into contact. When $\Gamma > 0.01336$, there is no solution in the range of interest, and no stationary point

appears on the energy curve (see Figure 2.2). In this case, the interface will go immediately from its initial configuration to solid-solid contact. For convenience, we can define a non dimensionless number, N_c, to specify the critical condition for the onset of instability, whereby

$$N_c = \frac{\Gamma}{0.01336} = 74.85 \frac{\gamma_{LV}{}^2 \left(\frac{\cos\theta_1 + \cos\theta_2}{2} \right)^2 V_o}{E'^2 H^5} \tag{2.2.1}$$

When $N_c < 1$, stable equilibrium can be achieved at the interface without solid-solid contact. Two solid surfaces gradually approach until maximum surface deflection exceeds $0.5577H$. When $N_c \geq 1$, the interface is unstable. Two solid surfaces spontaneously jump into contact.

2.3 Equilibrium Configuration with Contact

Once solid-solid contact is initiated, what kind of equilibrium configuration can be reached at the interface? This is the question to be answered in this section. We know that if the interface is able to reach an equilibrium configuration after solid-solid contact appears, the equilibrium configuration should look like the one shown in Figure 2.7. Three quantities, the pressure drop across the meniscus (Δp), the meniscus position (b) and the contact radius (a), are now required to specify the interface configuration.

Since solid-solid contact affects the pressure distribution and the surface deflection in the interface, equations (2.1.1) and (2.1.2) are no longer valid. Instead the pressure distribution, $p(r)$, and the surface deflection, $u(r)$, satisfy the following conditions: In the

contact region, where $r \le a$, the pressure is unknown, while the total surface deflection is equal to $u(r) = H$. Outside the contact region the deflection is unknown, while the pressure is piecewise uniform, equaling $-\Delta p$ in the annulus $a < r \le b$ and zero in the region of $r > b$. To obtain the unknown surface deflection (u) outside of the contact region (i.e., $r > a$) along with the unknown pressure distribution (p) within the contact region (i.e., $r \le a$), we use pressure-based flexibility influence coefficients.

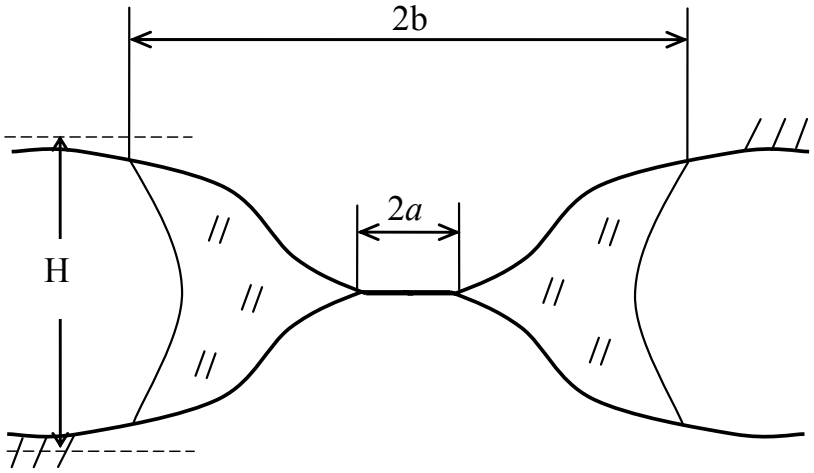

Figure 2.7 Schematic of the deformed interface between two elastic half-space connecting by a liquid bridge of volume V_o, with solid-solid contact.

First, we discretize the domain of interest. In this work, the domain of interest is a circle area of radius b, which includes the contact region ($0 \le r \le a$) and the liquid-wetted annulus ($a < r \le b$). Since the problem is axisymmetric, the region is divided into many small annular elements. The position of an element is specified by the radial

position of the inner boundary of the element. The deformed surface shape and the pressure distribution are represented by adjacent columns of uniform deflection or pressure acting on discrete segments of the surface (Figure 2.8). For example, for the i^{th} annular element, the radial position is r_i; the surface deflection is u_i; and the pressure is p_i. In this analysis, because the relative size of the contact zone changes, in order to maintain enough elements in and out of the contact zone to guarantee high accuracy of computation, the whole region of interest is unevenly divided, N uniform subintervals in the region of $r \le a$ and another N uniform subintervals in the region of $a < r \le b$. Therefore the continuous radial position, r, can be discretely represented by a vector of size ($2N$+1) by 1 with each elements given by

$$r_i = \begin{cases} (i-1)\dfrac{a}{N}, & 1 \le i \le N+1 \\ a + (i-N-1)\dfrac{b-a}{N}, & N+1 \le i \le 2N+1 \end{cases} \tag{2.3.1}$$

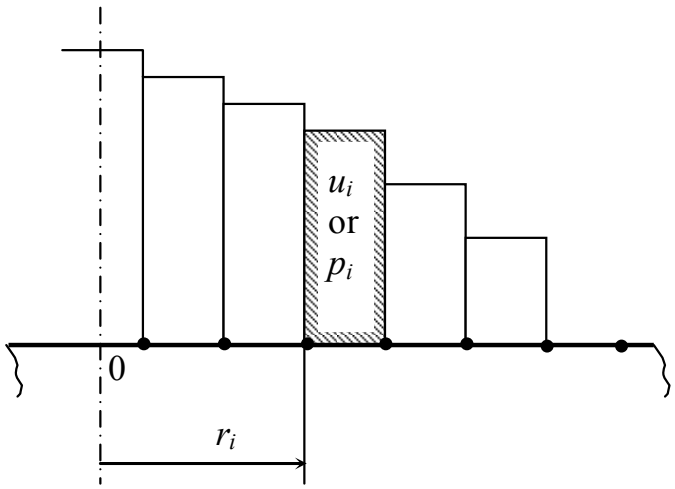

Figure 2.8 Discrete pressure and deformation elements.

The influence coefficient c_{ij} is defined on the discretized domain as the deflection at position r_i due to a unit pressure applied at position r_j. The value of c_{ij} can be determined in the following way: Suppose we wish to find the normal deflection at some radius r_i caused by a thin circular ring of constant pressure at radius r_j. By superposition we can view the pressurized ring as a combination of a uniform pressure circle of radius $r_j+\Delta r_j$ with a uniform tension circle of radius r_j (Figure 2.9). The magnitudes of pressure and tension are the same. Then the normal deflection at radius r_i can be write as

$$u(r_i)=\begin{cases}\dfrac{4p(r_j)r_j}{\pi E'}\left[(1+\dfrac{\Delta r_j}{r_j})\hat{E}(\dfrac{r_i}{r_j+\Delta r_j})-\hat{E}(\dfrac{r_i}{r_j})\right], & r_i \le r_j \\ \dfrac{4p(r_j)r_j}{\pi E'}\left[\begin{array}{l}(1+\dfrac{\Delta r_j}{r_j})\hat{E}(\dfrac{r_i}{r_j+\Delta r_j})-\dfrac{r_i}{r_j}\hat{E}(\dfrac{r_j}{r_i})+ \\ \dfrac{r_j}{r_i}(\dfrac{r_i^{\,2}}{r_j^{\,2}}-1)\hat{K}(\dfrac{r_j}{r_i})\end{array}\right], & r_j < r_i < r_j+\Delta r_j \\ \dfrac{4p(r_j)r_j}{\pi E'}\left[\begin{array}{l}\dfrac{r_i}{r_j}\hat{E}(\dfrac{r_i}{r_j+\Delta r_j})-\dfrac{r_i}{r_j}\hat{E}(\dfrac{r_j}{r_i})+(\dfrac{r_i}{r_j}-\dfrac{r_j}{r_i})\hat{K}(\dfrac{r_j}{r_i})- \\ \dfrac{r_i}{r_j}(1-\dfrac{(r_j+\Delta r_j)^2}{r_i^{\,2}})\hat{K}(\dfrac{r_j+\Delta r_j}{r_i})\end{array}\right], & r_i \ge r_j+\Delta r_j\end{cases} \tag{2.3.2}$$

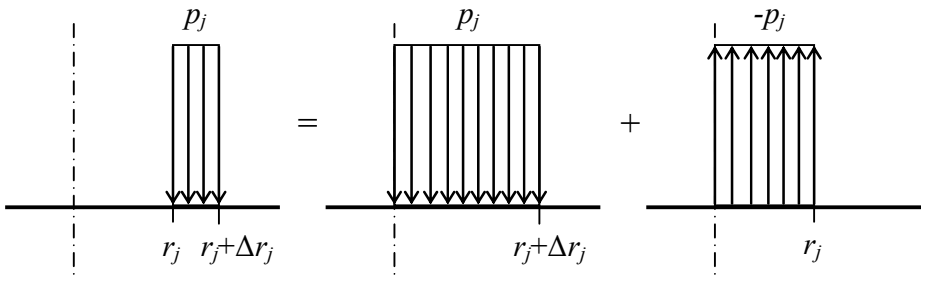

Figure 2.9 Equivalency of a pressurized ring to the superposition of a uniform pressure circle of radius $r_j+\Delta r_j$ with a uniform tension circle of radius r_j.

where $r_{i,j}$ are specified by equation (2.3.1) and $\Delta r_{i,j}$ are given by

$$\Delta r_i = \begin{cases} \dfrac{a}{N}, & 1 \le i \le N \\ \dfrac{b-a}{N}, & N+1 \le i \le 2N+1 \end{cases} \tag{2.3.3}$$

By definition, the influence coefficient is

$$c_{ij} = \frac{u(r_i)}{p(r_j)} = \begin{cases} \dfrac{4r_j}{\pi E'}\left[(1+\dfrac{\Delta r_j}{r_j})\hat{E}(\dfrac{r_i}{r_j+\Delta r_j}) - \hat{E}(\dfrac{r_i}{r_j})\right], & r_i \le r_j \\ \dfrac{4r_j}{\pi E'}\left[\begin{array}{l}(1+\dfrac{\Delta r_j}{r_j})\hat{E}(\dfrac{r_i}{r_j+\Delta r_j}) - \dfrac{r_i}{r_j}\hat{E}(\dfrac{r_j}{r_i}) + \\ \dfrac{r_j}{r_i}(\dfrac{r_i^2}{r_j^2}-1)\hat{K}(\dfrac{r_j}{r_i})\end{array}\right], & r_j < r_i < r_j + \Delta r_j \\ \dfrac{4r_j}{\pi E'}\left[\begin{array}{l}\dfrac{r_i}{r_j}\hat{E}(\dfrac{r_i}{r_j+\Delta r_j}) - \dfrac{r_i}{r_j}\hat{E}(\dfrac{r_j}{r_i}) + (\dfrac{r_i}{r_j}-\dfrac{r_j}{r_i})\hat{K}(\dfrac{r_j}{r_i}) - \\ \dfrac{r_i}{r_j}(1-\dfrac{(r_j+\Delta r_j)^2}{r_i^2})\hat{K}(\dfrac{r_j+\Delta r_j}{r_i})\end{array}\right], & r_i \ge r_j + \Delta r_j \end{cases} \tag{2.3.4}$$

Now we can see that the matrix of influence coefficient, $[c_{ij}]$ is a $(2N+1)$ by $(2N+1)$ matrix with all its elements determined by equation (2.3.4) when a and b are given.

Once the influence coefficient matrix $[c_{ij}]$ is generated, the deflection and pressure satisfy the system of linear equations

$$\{u_i\} = [c_{ij}]\{p_j\} \tag{2.3.5}$$

For convenience, we use vectors $\{r_{s1}\}$ and $\{r_{s2}\}$, $\{u_{s1}\}$ and $\{u_{s2}\}$, $\{p_{s1}\}$ and $\{p_{s2}\}$ to represent the radial position, surface deflection and the pressure distribution, where the subscript $s1$ and $s2$ indicate that the quantities are for the region inside or outside the contact zone, respectively. Now

$$r_{s1i} = (i-1)\frac{a}{N}, \qquad 1 \le i \le N+1 \tag{2.3.6}$$

$$r_{s2i} = a + i\frac{b-a}{N}, \qquad 1 \le i \le N \tag{2.3.7}$$

$$\Delta r_{s1} = \frac{a}{N} \tag{2.3.8}$$

$$\Delta r_{s2} = \frac{b-a}{N} \tag{2.3.9}$$

and

$$u_{s1i} = H, \qquad 1 \le i \le N+1 \tag{2.3.10}$$

$$p_{s2i} = -\Delta p, \qquad 1 \le i \le N \tag{2.3.11}$$

Then the unknowns $\{p_{s1}\}$ and $\{u_{s2}\}$ can be solved for by decomposing the system of equations (2.3.5) to two linear subsystems

$$\begin{Bmatrix} u_{s1} \\ u_{s2} \end{Bmatrix} = \begin{bmatrix} c_{s11} & c_{s12} \\ c_{s21} & c_{s22} \end{bmatrix} \begin{Bmatrix} p_{s1} \\ p_{s2} \end{Bmatrix} \tag{2.3.12}$$

i.e.,

$$\{u_{s1}\} = [c_{s11}]\{p_{s1}\} + [c_{s12}]\{p_{s2}\} \tag{2.3.13}$$

$$\{u_{s2}\} = [c_{s21}]\{p_{s1}\} + [c_{s22}]\{p_{s2}\} \tag{2.3.14}$$

where $[c_{s11}]$, $[c_{s12}]$, $[c_{s21}]$ and $[c_{s22}]$ are the corresponding sub-matrices in the influence coefficient matrix $[c_{ij}]$. $[c_{s11}]$ takes all $(N+1)$ by $(N+1)$ elements of $[c_{ij}]$ at the upper-left corner; $[c_{s12}]$ takes all $(N+1)$ by N elements of $[c_{ij}]$ at the upper-right corner; $[c_{s21}]$ takes all N by $(N+1)$ elements of $[c_{ij}]$ at the lower-left corner; $[c_{s12}]$ takes all N by N elements of $[c_{ij}]$ at the lower-right corner. Therefore, the unknown pressures and deflections are given by

$$\{p_{s1}\} = [c_{s11}]^{-1}\{\{u_{s1}\} - [c_{s12}]\{p_{s2}\}\} \tag{2.3.15}$$

$$\{u_{s2}\} = [c_{s21}]\{p_{s1}\} + [c_{s22}]\{p_{s2}\} \tag{2.3.16}$$

Similarly, vectors $\{h_{s1}\}$ and $\{h_{s2}\}$ can be used to represent the gap between the deformed surfaces inside the contact region and outside the contact region, respectively. Now

$$h_{s1i} = 0, \qquad 1 \le i \le N+1 \tag{2.3.17}$$

$$h_{s2i} = H - u_{s2i}, \qquad 1 \le i \le N \tag{2.3.18}$$

Therefore, the conservation of the liquid volume can be expressed by

$$\begin{aligned} V_o &= \int_a^b 2\pi r h(r) dr \\ &\approx \pi H(b^2 - a^2) - \sum_{i=1}^{N} 2\pi r_{s2i} u_{s2i} \Delta r_{s2} \end{aligned} \tag{2.3.19}$$

The elastic strain energy is determined by

$$\begin{aligned} U_E &= \frac{1}{2}\int_0^b 2\pi r(-p(r))u(r)dr \\ &\approx \frac{1}{2}\left[\sum_{i=1}^{N+1} 2\pi r_{s1i} p_{s1i} u_{s1i} \Delta r_{s1} + \sum_{i=1}^{N} 2\pi r_{s2i} p_{s2i} u_{s2i} \Delta r_{s2}\right] \end{aligned} \tag{2.3.20}$$

The surface energy is now computed by

$$\begin{aligned} U_S &= \pi(R_c{}^2 - b^2)(\gamma_{SV_1} + \gamma_{SV_2}) \\ &\quad + \pi(b^2 - a^2)(\gamma_{SL_1} + \gamma_{SL_2}) + \pi a^2 \gamma_{S12} \\ &= \pi R_c{}^2(\gamma_{SV_1} + \gamma_{SV_2}) - \pi b^2 \gamma_{LV}(\cos\theta_1 + \cos\theta_2) \\ &\quad - \pi a^2(\gamma_{SL_1} + \gamma_{SL_2}) + \pi a^2 \gamma_{S12} \end{aligned} \tag{2.3.21}$$

where γ_{S12} is the surface energy of the solid-solid interface. The total free energy stored in the interface is then written as

$$
\begin{aligned}
U_T &= U_E + U_S \\
&\approx \frac{1}{2}\left[\sum_{i=1}^{N+1} 2\pi r_{s1i} p_{s1i} u_{s1i} \Delta r_{s1} + \sum_{i=1}^{N} 2\pi r_{s2i} p_{s2i} u_{s2i} \Delta r_{s2}\right] \\
&\quad + \pi {R_c}^2 (\gamma_{SV_1} + \gamma_{SV_2}) - \pi b^2 \gamma_{LV} (\cos\theta_1 + \cos\theta_2) \\
&\quad - \pi a^2 (\gamma_{SL_1} + \gamma_{SL_2}) + \pi a^2 \gamma_{S12}
\end{aligned} \tag{2.3.22}
$$

Scaling,

$$r^* = \frac{r}{b} \tag{2.3.23}$$

$$m = \frac{a}{b} \tag{2.3.24}$$

$$u^* = \frac{u}{H} \tag{2.3.25}$$

$$p^* = \frac{p}{\Delta p} \tag{2.3.26}$$

gives

$$r_i^* = \begin{cases} (i-1)\dfrac{m}{N}, & 1 \le i \le N+1 \\ m + (i-N-1)\dfrac{1-m}{N}, & N+1 \le i \le 2N+1 \end{cases} \tag{2.3.27}$$

$$\Delta r_i^* = \begin{cases} \dfrac{m}{N}, & 1 \le i \le N \\ \dfrac{1-m}{N}, & N+1 \le i \le 2N+1 \end{cases} \tag{2.3.28}$$

$$r_{s1i}^* = (i-1)\frac{m}{N}, \qquad 1 \le i \le N+1 \tag{2.3.29}$$

$$r_{s2i}^* = m + i\frac{1-m}{N}, \qquad 1 \le i \le N \tag{2.3.30}$$

$$\Delta r_{s1}^* = \frac{m}{N} \tag{2.3.31}$$

$$\Delta r_{s2}^{*} = \frac{1-m}{N} \tag{2.3.32}$$

$$u_{s1i}^{*} = 1, \qquad 1 \le i \le N+1 \tag{2.3.33}$$

$$p_{s2i}^{*} = -1, \qquad 1 \le i \le N \tag{2.3.34}$$

And defining the dimensionless influence coefficient matrix $[c_{ij}^{*}]$ as

$$\left[c_{ij}^{*}\right] = \left[c_{ij}\right] \Big/ \frac{4b}{\pi E'} \tag{2.3.35}$$

results in

$$c_{ij}^{*} = \begin{cases} r_j^{*}\left[(1+\dfrac{\Delta r_j^{*}}{r_j^{*}})\hat{E}(\dfrac{r_i^{*}}{r_j^{*}+\Delta r_j^{*}}) - \hat{E}(\dfrac{r_i^{*}}{r_j^{*}})\right], & r_i^{*} \le r_j^{*} \\ r_j^{*}\left[\begin{array}{l}(1+\dfrac{\Delta r_j^{*}}{r_j^{*}})\hat{E}(\dfrac{r_i^{*}}{r_j^{*}+\Delta r_j^{*}}) - \dfrac{r_i^{*}}{r_j^{*}}\hat{E}(\dfrac{r_j^{*}}{r_i^{*}}) + \\ \dfrac{r_j^{*}}{r_i^{*}}(\dfrac{r_i^{*2}}{r_j^{*2}}-1)\hat{K}(\dfrac{r_j^{*}}{r_i^{*}})\end{array}\right], & r_j^{*} < r_i^{*} < r_j^{*} + \Delta r_j^{*} \\ r_j^{*}\left[\begin{array}{l}\dfrac{r_i^{*}}{r_j^{*}}\hat{E}(\dfrac{r_i^{*}}{r_j^{*}+\Delta r_j^{*}}) - \dfrac{r_i^{*}}{r_j^{*}}\hat{E}(\dfrac{r_j^{*}}{r_i^{*}}) + (\dfrac{r_i^{*}}{r_j^{*}} - \dfrac{r_j^{*}}{r_i^{*}})\hat{K}(\dfrac{r_j^{*}}{r_i^{*}}) - \\ \dfrac{r_i^{*}}{r_j^{*}}(1 - \dfrac{(r_j^{*}+\Delta r_j^{*})^2}{r_i^{*2}})\hat{K}(\dfrac{r_j^{*}+\Delta r_j^{*}}{r_i^{*}})\end{array}\right], & r_i^{*} \ge r_j^{*} + \Delta r_j^{*} \end{cases} \tag{2.3.36}$$

One can see that besides indices i and j $[c_{ij}^{*}]$ depends only on m and N.

From equations (2.3.15) and (2.3.16), the dimensionless unknown pressures, $\{p_{s1}^{*}\}$, and deflections, $\{u_{s2}^{*}\}$, are solved as

$$\{p_{s1}^{*}\} = \frac{\pi E' H}{4b\Delta p}\left[c_{s11}^{*}\right]^{-1}\{u_{s1}^{*}\} - \left[c_{s11}^{*}\right]^{-1}\left[c_{s12}^{*}\right]\{p_{s2}^{*}\} \tag{2.3.37}$$

$$\{u_{s2}^{*}\} = \frac{4b\Delta p}{\pi E' H}\left[c_{s21}^{*}\right]\{p_{s1}^{*}\} + \frac{4b\Delta p}{\pi E' H}\left[c_{s22}^{*}\right]\{p_{s2}^{*}\} \tag{2.3.38}$$

Introducing η defined (as before) by

$$\eta = \frac{2\Delta p b}{E^{'} H} \tag{2.3.39}$$

results in

$$\left\{p_{s1}^{*}\right\} = \frac{\pi}{2\eta}\left\{p_{s11}^{*}\right\} - \left\{p_{s12}^{*}\right\} \tag{2.3.40}$$

where

$$\left\{p_{s11}^{*}\right\} = \left[c_{s11}^{*}\right]^{-1}\left\{u_{s1}^{*}\right\} \tag{2.3.41}$$

$$\left\{p_{s12}^{*}\right\} = \left[c_{s11}^{*}\right]^{-1}\left[c_{s12}^{*}\right]\left\{p_{s2}^{*}\right\} \tag{2.3.42}$$

and

$$\begin{aligned}\left\{u_{s2}^{*}\right\} &= \frac{2\eta}{\pi}\left[c_{s21}^{*}\right]\left\{p_{s1}^{*}\right\} + \frac{2\eta}{\pi}\left[c_{s22}^{*}\right]\left\{p_{s2}^{*}\right\} \\ &= \left\{u_{s21}^{*}\right\} - \frac{2\eta}{\pi}\left(\left\{u_{s22}^{*}\right\} - \left\{u_{s23}^{*}\right\}\right)\end{aligned} \tag{2.3.43}$$

with

$$\left\{u_{s21}^{*}\right\} = \left[c_{s21}^{*}\right]\left[c_{s11}^{*}\right]^{-1}\left\{u_{s1}^{*}\right\} \tag{2.3.44}$$

$$\left\{u_{s22}^{*}\right\} = \left[c_{s21}^{*}\right]\left[c_{s11}^{*}\right]^{-1}\left[c_{s12}^{*}\right]\left\{p_{s2}^{*}\right\} \tag{2.3.45}$$

$$\left\{u_{s23}^{*}\right\} = \left[c_{s22}^{*}\right]\left\{p_{s2}^{*}\right\} \tag{2.3.46}$$

Use of equation (2.3.19) leads to

$$\begin{aligned}V_o &= \pi H b^2 (1 - m^2) - 2\pi H b^2 \sum_{i=1}^{N} r_{s2i}^{*} u_{s2i}^{*} \Delta r_{s2}^{*} \\ &= \pi H b^2 (1 - m^2 - \lambda_1 + \lambda_2 \eta)\end{aligned} \tag{2.3.47}$$

where

$$\lambda_1 = 2\sum_{i=1}^{N} r_{s2i}^{*} \Delta r_{s2}^{*} u_{s21i}^{*} \tag{2.3.48}$$

$$\lambda_2 = \frac{4}{\pi}\sum_{i=1}^{N} r_{s2i}^{*}\Delta r_{s2}^{*}(u_{s22i}^{*} - u_{s23i}^{*}) \tag{2.3.49}$$

Therefore, the wetted radius b is given by

$$b = \sqrt{\frac{V_o}{\pi H(1 - m^2 - \lambda_1 + \lambda_2\eta)}} \tag{2.3.50}$$

The elastic strain energy can be written as

$$\begin{aligned} U_E &= \pi H b^2 \Delta p\left[\sum_{i=1}^{N+1} r_{s1i}^{*} p_{s1i}^{*} u_{s1i}^{*}\Delta r_{s1}^{*} + \sum_{i=1}^{N} r_{s2i}^{*} p_{s2i}^{*} u_{s2i}^{*}\Delta r_{s2}^{*}\right] \\ &= \left(\frac{\pi^2 E' H^2}{4}\lambda_3 - \frac{\pi E' H^2}{2}\lambda_4\eta - E' H^2\lambda_5\eta^2\right)b \end{aligned} \tag{2.3.51}$$

where

$$\lambda_3 = \sum_{i=1}^{N+1} r_{s1i}^{*}\Delta r_{s1}^{*} p_{s11i}^{*} u_{s1i}^{*} \tag{2.3.52}$$

$$\lambda_4 = \sum_{i=1}^{N+1} r_{s1i}^{*}\Delta r_{s1}^{*} p_{s12i}^{*} u_{s1i}^{*} - \sum_{i=1}^{N} r_{s2i}^{*}\Delta r_{s2}^{*} p_{s2i}^{*} u_{s21i}^{*} \tag{2.3.53}$$

$$\lambda_5 = \sum_{i=1}^{N} r_{s2i}^{*}\Delta r_{s2}^{*} p_{s2i}^{*}(u_{s22i}^{*} - u_{s23i}^{*}) \tag{2.3.54}$$

From equation (2.3.22), the total free energy stored in the interface is then given by

$$\begin{aligned} U_T &= \pi R_c^{\,2}(\gamma_{SV_1} + \gamma_{SV_2}) \\ &\quad - \pi b^2 \gamma_{LV}(\cos\theta_1 + \cos\theta_2)\left(1 + m^2\frac{(\gamma_{SL_1} + \gamma_{SL_2}) - \gamma_{S12}}{\gamma_{LA}(\cos\theta_1 + \cos\theta_2)}\right) \\ &\quad + \left(\frac{\pi^2 E' H^2}{4}\lambda_3 - \frac{\pi E' H^2}{2}\lambda_4\eta - E' H^2\lambda_5\eta^2\right)b \end{aligned} \tag{2.3.55}$$

A dimensionless system free energy U_T^{*} may be defined as

$$U_T^{*} = \frac{U_T - \pi R_c^2(\gamma_{SV_1} + \gamma_{SV_2})}{\sqrt{\pi}E' H^{3/2} V_o^{1/2}} \tag{2.3.56}$$

Substituting equation (2.3.50) into equation (2.3.55) and nondimensionalizing gives

$$U_T^{\ *} = -2\sqrt{\frac{\Gamma}{\pi}}\frac{(1+\Phi m^2)}{(1-m^2-\lambda_1+\lambda_2\eta)} + \frac{(\frac{\pi}{4}\lambda_3 - \frac{1}{2}\lambda_4\eta - \frac{1}{\pi}\lambda_5\eta^2)}{\sqrt{(1-m^2-\lambda_1+\lambda_2\eta)}} \tag{2.3.57}$$

where

$$\Gamma = \frac{\gamma_{LV}{}^2\left(\frac{\cos\theta_1+\cos\theta_2}{2}\right)^2 V_o}{E'^2 H^5} \tag{2.3.58}$$

as before, and

$$\Phi = \frac{(\gamma_{SL_1}+\gamma_{SL_2})-\gamma_{S12}}{\gamma_{LV}(\cos\theta_1+\cos\theta_2)} \tag{2.3.59}$$

Applying the Young's equation (equation (2.1.21)), it can be rewritten as

$$\begin{aligned}\Phi &= \frac{(\gamma_{SV_1}+\gamma_{SV_2}-\gamma_{S12})-\gamma_{LV}(\cos\theta_1+\cos\theta_2)}{\gamma_{LV}(\cos\theta_1+\cos\theta_2)} \\ &= \frac{\Delta\gamma}{\gamma_{LV}(\cos\theta_1+\cos\theta_2)} - 1\end{aligned} \tag{2.3.60}$$

where $\Delta\gamma$ is the Dupré energy of adhesion in dry contact. Therefore, it is seen that Φ is a measure of the relative strength of solid-solid interaction to the meniscus capillarity.

Now factors $\lambda_1 \sim \lambda_5$ depend on *m* and *N*. When *N* goes to infinity, $\lambda_1 \sim \lambda_5$ converge to certain functions of *m* (Figures 2.10-2.14). The convergence can be checked from the relative approximate error, which is less than 1% when *N* increases from 100 to 150. Then, by curve fitting, we get

$$\lambda_1 = 1.2878m - 0.9242m^2 - 0.6635m^3 + 0.7092m^4 - 0.4073m^5 \tag{2.3.61}$$

$$\lambda_2 = -\frac{8}{3\pi} + 1.2971m - 0.0252m^2 - 0.6381m^3 + 0.4596m^4 - 0.2458m^5 \tag{2.3.62}$$

$$\lambda_3 = 0.4037m \tag{2.3.63}$$

$$\lambda_5 = -\frac{2}{3} + 1.0387m - 0.1035m^2 - 0.2148m^3 - 0.1035m^4 + 0.0505m^5 \tag{2.3.64}$$

The relative errors of all these curvefittings are less than 0.3%. In Figure 2.13, λ_4 does vary with m. However, it is noted that the values of λ_4 approach zero when N increases. When compared with the corresponding values of λ_1~ λ_3 and λ_5, the values of λ_4 are two order less, except for m close to zero. Therefore, the effect of λ_4 can be neglected for most conditions. So, for simplicity, λ_4 is set to be zero independent of m.

$$\lambda_4 = 0 \tag{2.3.65}$$

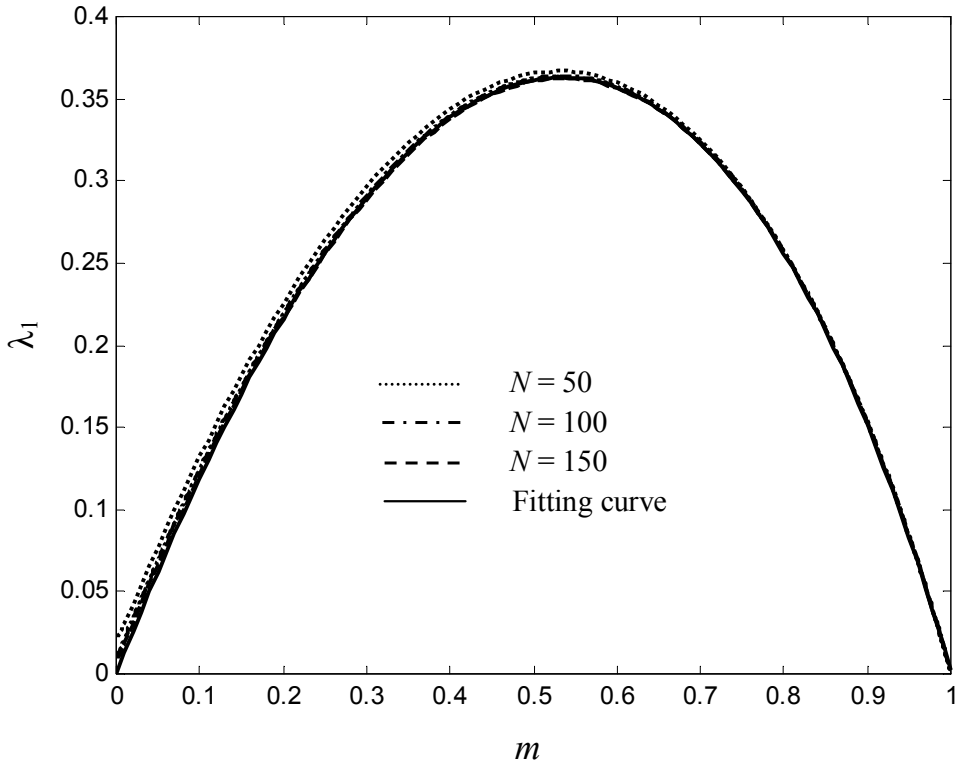

Figure 2.10 Variation of coefficient λ_1 with m and N.

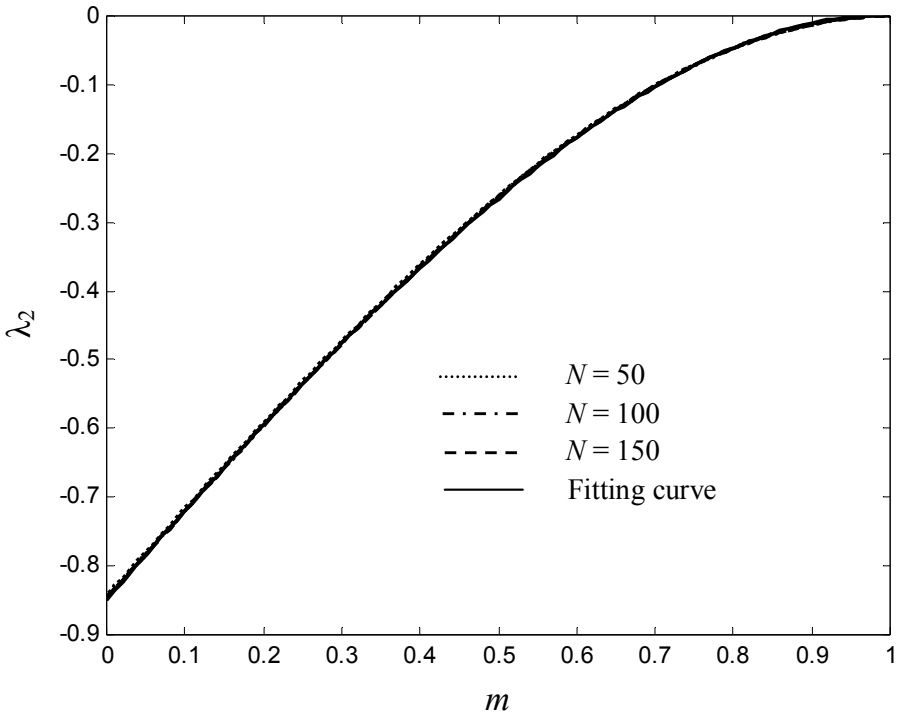

Figure 2.11 Variation of coefficient λ_2 with m and N.

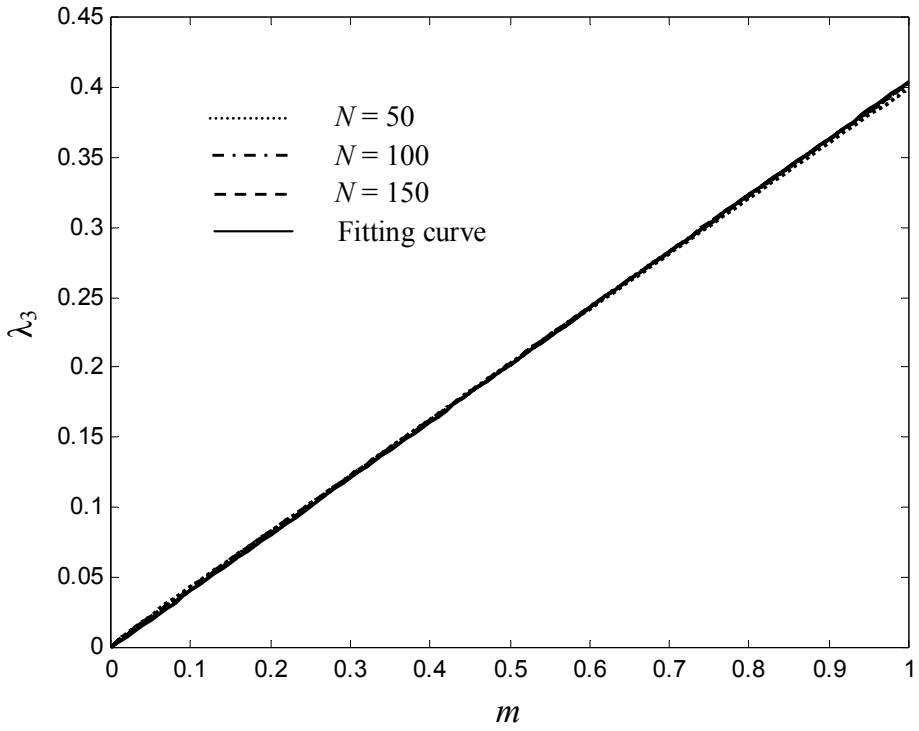

Figure 2.12 Variation of coefficient λ_3 with m and N.

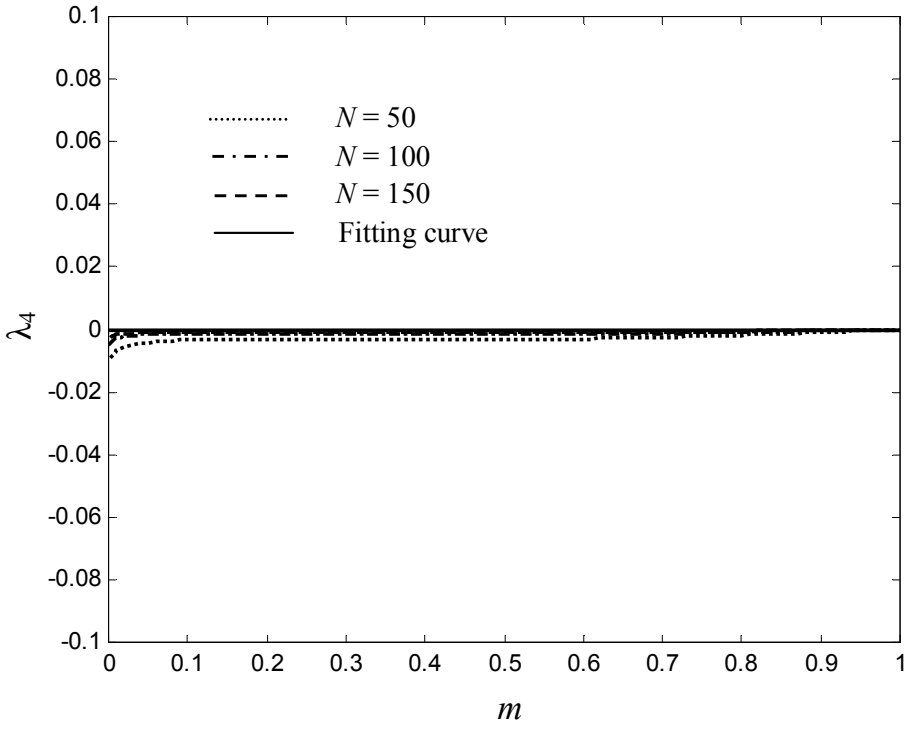

Figure 2.13 Variation of coefficient λ_4 with m and N.

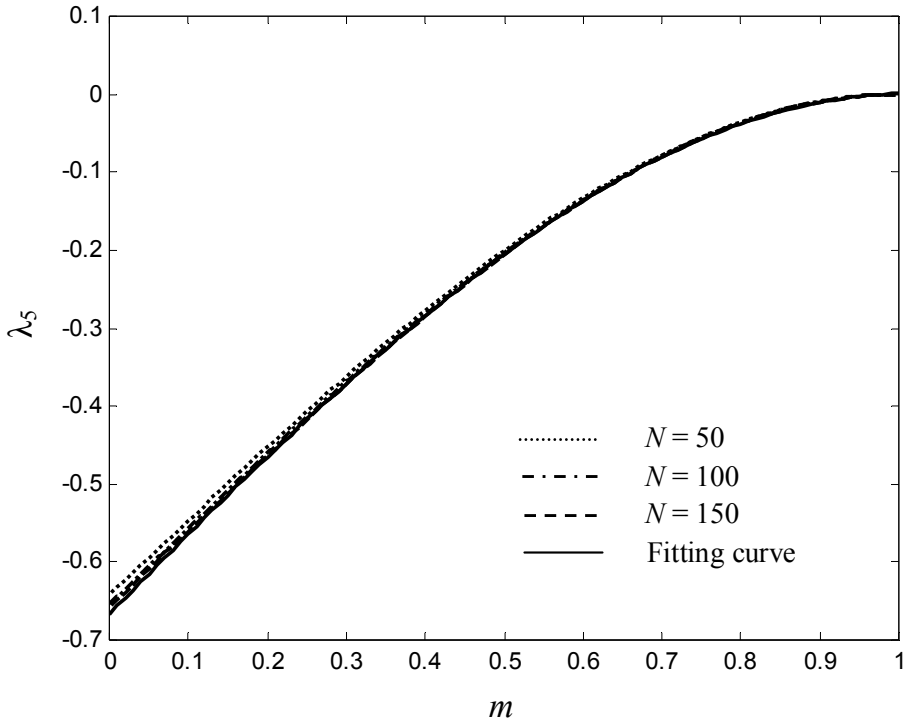

Figure 2.14 Variation of coefficient λ_5 with m and N.

Substituting equations (2.3.61-2.3.65) into equation (2.3.57), we can compute the dimensionless system free energy U_T^* directly from η, m, Γ, and Φ. And by controlling the accuracy of convergence and curve fitting, the relative error of U_T^* calculated this way can be very small. It should be pointed out that equation (2.3.57) reduces to equation (2.1.23) when $m = 0$, so the dimensionless system free energy U_T^* is continuous at $\eta = 1$.

For a given set of Γ and Φ, a particular combination of η and m represents a provisional equilibrium contact configuration, which yields a deflection profile $u(r)$ and associated pressure distribution $p(r)$, that (i) satisfy equation (2.3.5), (ii) prevent surface

interpenetration, and (iii) conserve liquid volume. When the configuration corresponds to a local energy minimum, a stable equilibrium is reached. To form a provisional equilibrium contact configuration, η and m must satisfy some conditions. First, to avoid surface penetration, m must be greater than 0 ($m > 0$) except for point contact where $\eta = 1$ and $m = 0$. Second, to keep a positive liquid volume in the interface, from equation (2.3.47), it is necessary that

$$1 - m^2 - \lambda_1 + \lambda_2 \eta > 0 \tag{2.3.66}$$

These constraints delineate a feasible region on $m - \eta$ plane for any provisional equilibrium contact configuration (Figure 2.15). By looking for a local energy minimum in this region, we may be able to obtain the actual equilibrium contact configuration for the given Γ, and Φ.

Figures 2.16 shows the energy surfaces for $\Gamma = 0.01336$ (when the interface just lost its stability) with $\Phi = 0.001$ and $\Phi = 1000$, respectively. As observed, there are no local minima on the energy surfaces and the lowest values of energy are found on the boundary of the feasible region, which is specified by $1 - m^2 - \lambda_1 + \lambda_2 \eta = 0$. From equation (2.3.50) it is see that, the wetted radius b goes to infinity on this boundary, and as does the contact radius a, since m (equals a/b) is finite. Hence no stable equilibrium contact configuration exists once the interface lost its stability and the surfaces go from separation into full contact. For a real structure, the details of the boundary supports will determine the final interface configuration. Nevertheless much of the interface may be in solid-solid contact. This kind of interface geometry may induce large adhesion forces (e.g., stiction) and cause operational failure.

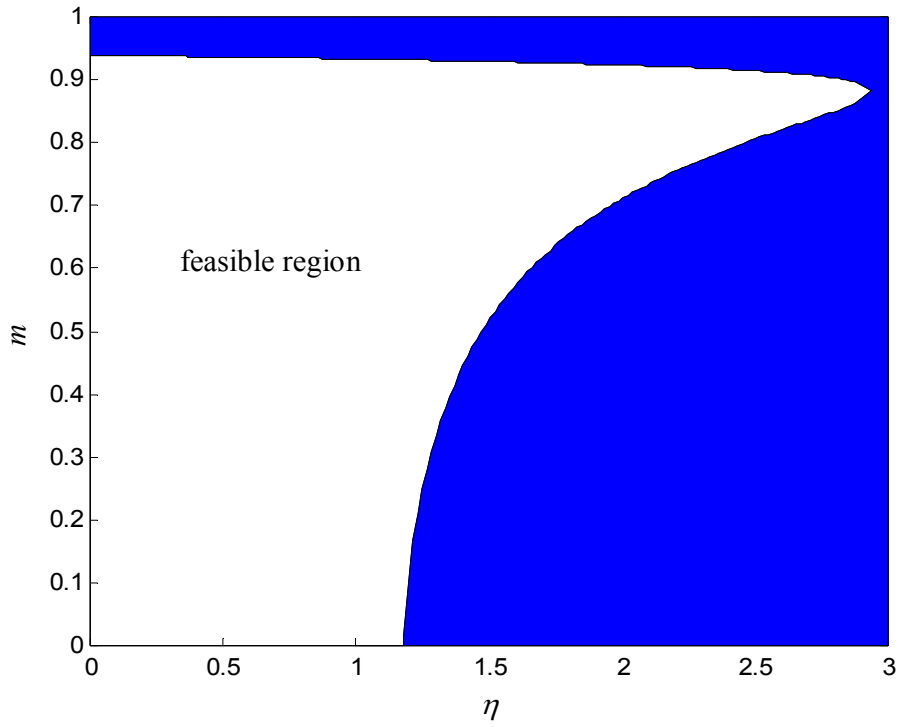

Figure 2.15 Feasible region for a provisional equilibrium contact configuration of the interface between two elastic half-spaces.

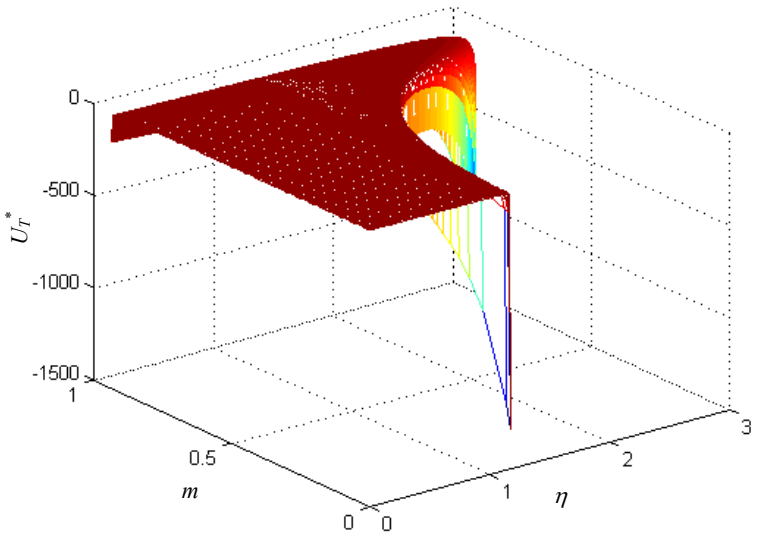

(a)

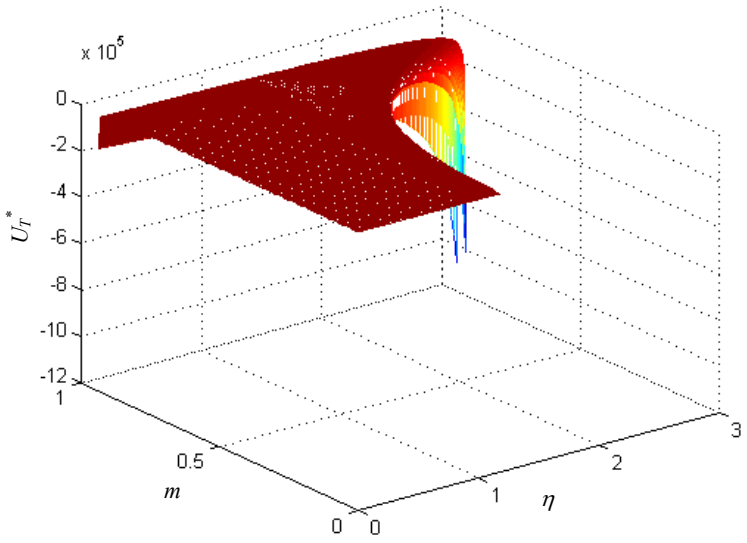

(b)

Figure 2.16 Dimensionless total free energy for all provisional equilibrium configurations of the interface between two elastic half-space after solid-solid contact appears. Energy surfaces are shown for $\Gamma = 0.01336$ (when the interface just lost its stability) with (a) $\Phi = 0.001$ and (b) $\Phi = 1000$.

2.4 Conclusions

The interaction between two elastic half-spaces bridged by a fixed volume of liquid was investigated and the mechanical stability of the structure was examined. From the analysis, the following conclusions can be drawn:

1) The non-dimensionalized system before contact is one-degree-of-freedom system in that all dimensionless equilibrium parameters of the interface can be expressed in terms of Γ, where $\Gamma = \dfrac{\gamma_{LV}{}^2 \left(\dfrac{\cos\theta_1 + \cos\theta_2}{2} \right)^2 V_o}{E'^2 H^5}$.

2) A dimensionless number $N_c = 74.85\Gamma$ was found to determine the structure stability. When $N_c < 1$, the system can reach equilibrium without solid-solid contact. When $N_c \geq 1$, the interface jumps into solid-solid contact.

3) No equilibrium state exists after solid-solid contact appears. Once contact is initiated, the contact region will continue to expand until the two surfaces are in full contact.

CHAPTER III

A LIQUID BRIDGE BETWEEN TWO ELASTIC SPHERES

3.1 Equilibrium Configuration without Contact

Now consider two elastic spheres of radii R_1 and R_2 coupled via a small liquid bridge of volume, V_o (Figure 3.1). They are initially separated by a minimum gap, H. And like in the half-space case, b is the radius of wetted area; $E_{1,2}$ and $\nu_{1,2}$ are the elastic moduli and Poisson's ratios, respectively, of the two spheres.

Assuming b is very small compared to R_1 and R_2, we can ignore the influence of body curvature and adopt the half-space approximations for the surface deformation. Therefore, equations (2.1.1) and (2.1.2) still can be used to represent the normal pressure on each surface, $p(r)$, and the combined elastic deflection, $u(r)$, of both surfaces. However, the gap $h(r)$ between the deformed surfaces is now represented in the form

$$h(r) = H + \frac{r^2}{2R} - u(r) \tag{3.1.1}$$

where

$$\frac{1}{R} = \frac{1}{R_{s1}} + \frac{1}{R_{s2}} \tag{3.1.2}$$

And conservation of liquid volume is expressed by

$$V_o = \int_0^b 2\pi r h(r) dr = \int_0^b 2\pi r (H + \frac{r^2}{2R} - u(r)) dr \tag{3.1.3}$$

which yields

$$V_o = \pi H b^2 - \frac{16}{3E'} \Delta p b^3 + \frac{\pi}{4R} b^4 \tag{3.1.4}$$

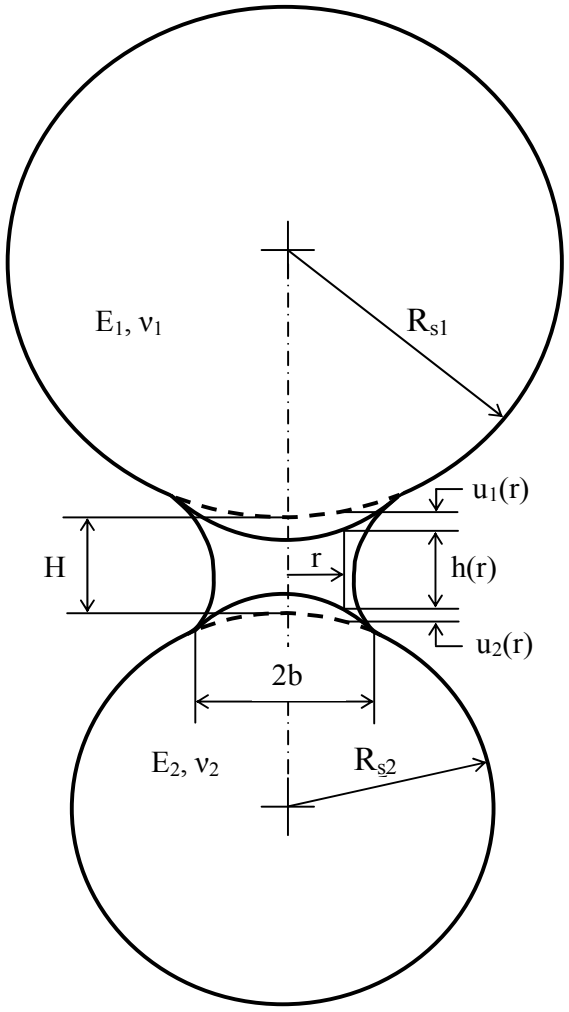

Figure 3.1 Schematic of the deformed interface between two elastic spheres connecting by a liquid bridge of volume V_o, without solid-solid contact.

The total free energy U_T can still be computed from equation (2.1.14), i.e.,

$$\begin{aligned} U_T &= \pi(R_c^{\,2} - b^2)(\gamma_{SV_1} + \gamma_{SV_2}) + \pi b^2(\gamma_{SL_1} + \gamma_{SL_2}) + \frac{8}{3E'}\Delta p^2 b^3 \\ &= \pi R_c^{\,2}(\gamma_{SV_1} + \gamma_{SV_2}) - \pi b^2 \gamma_{LV}(\cos\theta_1 + \cos\theta_2) + \frac{8}{3E'}\Delta p^2 b^3 \end{aligned} \tag{3.1.5}$$

For non-dimensionalization, we introduce dimensionless quantities

$$\eta = \frac{2\Delta p b}{E'H} \tag{3.1.6}$$

$$B = \frac{b^2}{RH} \tag{3.1.7}$$

$$\Psi = \frac{V_o}{RH^2} \tag{3.1.8}$$

$$\Gamma = \frac{\gamma_{LV}^{\,2}\left(\frac{\cos\theta_1 + \cos\theta_2}{2}\right)^2 V_o}{E'^2 H^5} \tag{3.1.9}$$

and define the dimensionless system free energy U_T^* as

$$U_T^{\,*} = \frac{U_T - 2\pi R_c^{\,2}(\gamma_{SV_1} + \gamma_{SV_2})}{\pi E' H^{5/2} R^{1/2}} \tag{3.1.10}$$

Dividing both sides of equation (3.1.4) by RH^2 and replacing $\frac{2\Delta p b}{E'H}$ by η, $\frac{b^2}{RH}$ by B, we get

$$\Psi = \pi(1 - \frac{8}{3\pi}\eta)B + \frac{\pi}{4}B^2 \tag{3.1.11}$$

Solving equation (3.1.11) for B yields

$$B = -2(1 - \frac{8}{3\pi}\eta) + 2\sqrt{(1 - \frac{8}{3\pi}\eta)^2 + \frac{\Psi}{\pi}} \tag{3.1.12}$$

Therefore

$$b = \sqrt{RHB} = -2RH(1 - \frac{8}{3\pi}\eta) + \sqrt{4R^2H^2(1 - \frac{8}{3\pi}\eta)^2 + \frac{4RV_o}{\pi}} \tag{3.1.13}$$

and

$$\Delta p = \frac{\eta H E'}{2b} = \frac{1}{2}\frac{\eta H E'}{\sqrt{-2RH(1-\frac{8}{3\pi}\eta)+\sqrt{4R^2H^2(1-\frac{8}{3\pi}\eta)^2+\frac{4RV_o}{\pi}}}} \tag{3.1.14}$$

Non-dimensionalizing the total free energy U_T in equation (3.1.5) according to equation (3.1.10), we get

$$U_T^* = -2\sqrt{\frac{\Gamma}{\Psi}}B + \frac{2}{3\pi}\eta^2 B^{1/2} \tag{3.1.15}$$

The dimensionless system free energy U_T^* depends only on η, Γ and Ψ. And like in the half-space case, η indicates the extent of surface approach and its value represents a provisional equilibrium configuration of the interface. The parameter Γ evaluates the combined effects of solid elasticity, meniscus capillarity, volume of liquid bridge and the interface geometry. The new dimensionless parameter Ψ can be seen as a normalized measure of liquid bridge volume. By taking the ratio of Γ and Ψ another dimensionless parameter can be introduced, according to

$$\mu^3 = \frac{\Gamma}{\Psi} = \frac{R\gamma_{LV}{}^2\left(\frac{\cos\theta_1+\cos\theta_2}{2}\right)^2}{E'^2H^3} \tag{3.1.16}$$

It can be seen that μ, which is analogous to the Tabor parameter[33] in dry contact ($\mu_T^3 = \frac{R\Delta\gamma^2}{E'^2\varepsilon^3}$, where ε is the local equilibrium separation), is another measure of the relative strength of meniscus capillarity to the solid elasticity. From equation (3.1.15), we can see that η, μ and Ψ may be a better set of parameters to describe the system. However, in order to be consistent with the results of Chapter II, η, Γ and Ψ will continue to be used in this analysis.

For given values of Γ and Ψ, the variation of the dimensionless system free energy with η is shown in Figure 3.2. At equilibrium, the dimensionless free energy U_T^* reaches a minimum, at which point $\frac{dU_T^*}{d\eta} = 0$. After differentiating and simplifying, following condition for equilibrium is obtained

$$\frac{\frac{\Psi}{8}\left(\frac{1}{3\pi}\eta^2 + \frac{1}{2}\eta\sqrt{(1-\frac{8}{3\pi}\eta)^2 + \frac{\Psi}{\pi}}\right)^2}{-(1-\frac{8}{3\pi}\eta) + \sqrt{(1-\frac{8}{3\pi}\eta)^2 + \frac{\Psi}{\pi}}} = \Gamma \tag{3.1.17}$$

The solution space of equation (3.1.17) for $0 \le \eta \le 1$ is plotted in Figure 3.3. As the function represented by the left-hand-side (LHS) of equation (3.1.17) depends on Ψ, several curves are shown in Figure 3.3 at different values of Ψ.

From Figures 3.2 and 3.3 we can see that when the dimensionless parameters Γ and Ψ take different values, the character of the solution of equation (3.1.17) changes. When $\Psi < 0.6143$, the solution space (Figure 3.3) is similar to the half-space case in that the curve has local maximum. Also for sufficiently small Γ, there is only one corresponding η_{eq}. This value corresponds to a local minimum in the total free energy figure (Figure 3.2). As Γ increases to a certain level (for a given Ψ), two values of η_{eq} appear in the range, corresponding to a local maximum and a local minimum in Figure 3.2, respectively. A local minimum on the energy curve refers to a stable equilibrium configuration without solid-solid contact. Therefore for these small to moderate values of Γ, stable equilibrium configurations can be achieved in the interface without solid-solid contact, and the two surfaces of the interface gradually approach each other as Γ increases. Then, for given Ψ, when Γ reaches the local maximum (Figure 3.3), the two

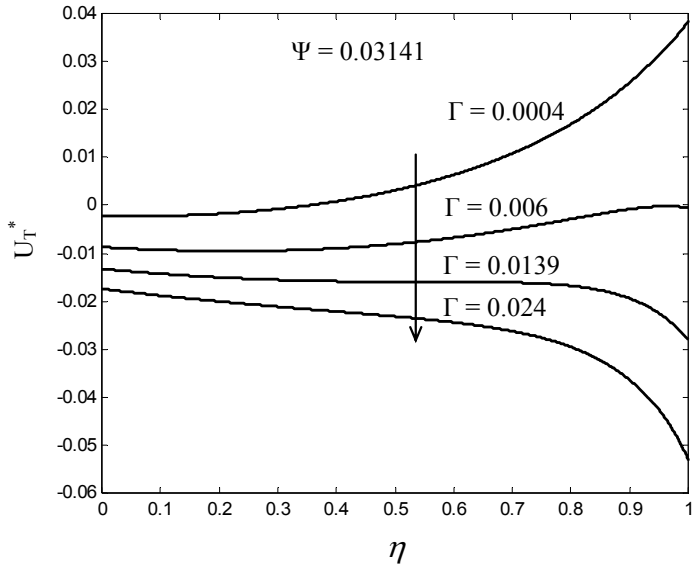

(a)

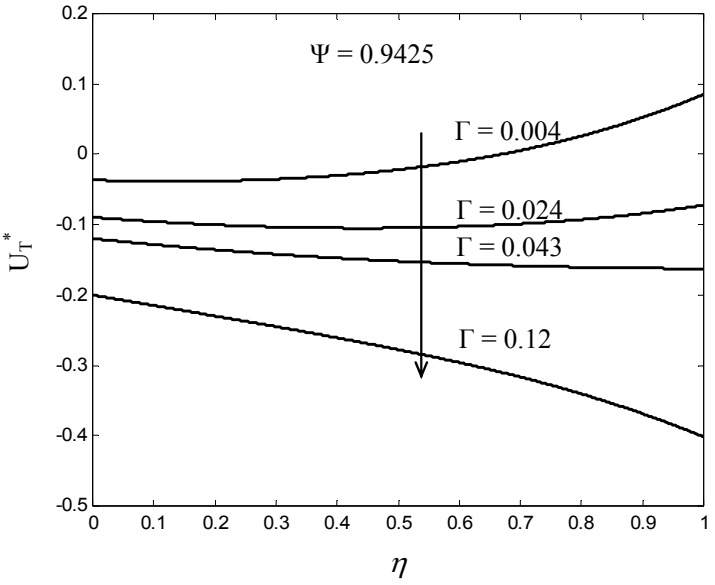

(b)

Figure 3.2 Typical dimensionless free energy curves as a function of η for the interface between two elastic spheres before solid-solid contact occurs:

(a) $\Psi < 0.6143$; (b) $\Psi \geq 0.6143$.

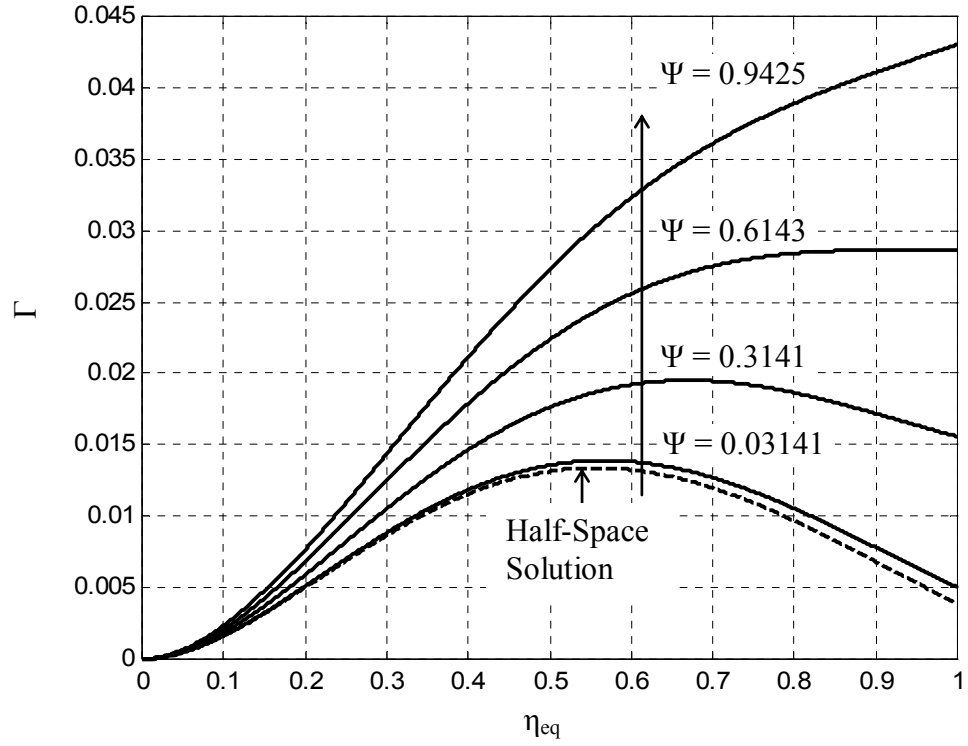

Figure 3.3 The solution space of equation (3.1.17) in the range of $0 \le \eta \le 1$, defining the equilibrium configurations in the case of no solid-solid contact.

solutions merge to one, and the local maximum and the local minimum on the corresponding energy curve merge to an inflection point (Figure 3.2). At the inflection point, the equilibrium is unstable. A global minimum appears at η=1, which indicates a state with solid-solid contact. Thus, whenever there is a disturbance causing a small increase in η beyond this η_{eq}, the system will "slide down" to the point of global minimum free energy (η_{eq}=1) meaning that the solid surfaces jump into contact from finite separation. If Γ increases further, there is no solution in the range of interest, and no

stationary point appears on the energy curve (see Figure 3.2). In this case, the interface will go immediately from its initial configuration to one with solid-solid contact. Therefore, the maximum value of the LHS of equation (3.1.17) for given Ψ is a critical value. When Γ is less than this critical value, the interface can achieve some stable equilibrium configuration without solid-solid contact; when Γ is greater than or equal to this critical value, the interface is unstable with any non-contact configuration and thus solid-solid contact must occur.

When $\Psi \geq 0.6143$, the corresponding curve in Figure 3.3 increases with η monotonically, and reaches a maximum at $\eta = 1$. For those Γ less than the maximum value of the curve, there is only one η_{eq} in the range from 0 to 1. This value corresponds to a local minimum in the total free energy (Figure 3.2). So, for these Γ, stable equilibrium configurations can be achieved in the interface without solid-solid contact. And as Γ increases, the value of η_{eq} approaches unity; i.e., the two surfaces of the interface gradually come into point contact. When Γ is equal to the maximum value of the equilibrium curve (e.g., $\Gamma = 0.043$ for $\Psi = 0.9425$ in Figure 3.3), the solution η_{eq} is equal to 1. The corresponding energy curve (Figure 3.2) attains a minimum at $\eta_{eq} = 1$, where the slope is zero. These results seem to imply a stable equilibrium with point contact configuration. However, to determine the real state of stability of point contact, one needs to know the variation of the system free energy beyond $\eta_{eq} = 1$, which will be studied in the next section.

When Γ is greater than the maximum value of the equilibrium curve, there is no solution in the range of interest. The energy continues to decrease with η, and no

stationary point appears on the energy curve. In this case, the interface cannot achieve an equilibrium without solid-solid contact. So, the maximum value of the LHS function of equation (3.1.17) in the range of $0 \le \eta \le 1$ still is the critical value. When Γ is less than this value, the interface can achieve some stable equilibrium configuration without solid-solid contact; when Γ is greater than or equal to this value, solid-solid contact appears at the interface. This critical value is denoted as Γ_c. For both situations ($\Psi \ge 0.6143$ and $\Psi < 0.6143$), this parameter, which depends on Ψ, defines the boundary between contact and non-contact regions in the Ψ-Γ plane as shown in Figure 3.4. The critical boundary in Figure 3.4 can be fitted by the curve $\Gamma_c(\Psi) = 0.03007\Psi^{1.3955} + 0.01336$ with an error less than 7%.

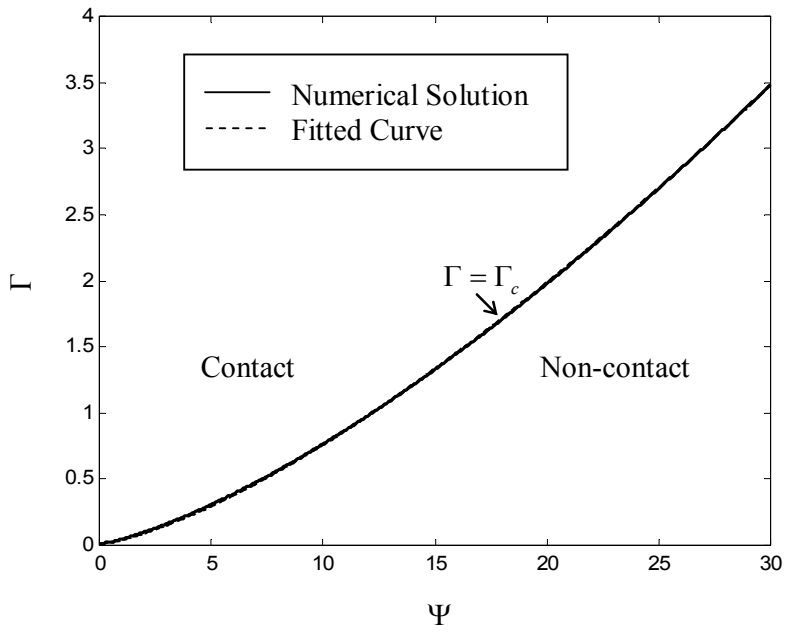

Figure 3.4 The division of contact and non-contact regions in Ψ-Γ space as surfaces approach. When $\Gamma = \Gamma_c$, the surfaces first come into contact.

If the system can achieve stable equilibrium without solid-solid contact, the equilibrium configuration can be found by solving equation (3.1.17) for η_{eq} (i.e., for given values of Γ and Ψ). As there is no closed-form solution of equation (3.1.17). One must find the roots graphically or numerically. When there are two roots in the range ($0 \le \eta \le 1$), the one associated with the local maximum free energy is discarded. The one associated with the local minimum free energy is substituted into equations (3.1.13) and (3.1.14) to calculate b and Δp at equilibrium, respectively. We now define a dimensionless equilibrium wetted-area radius and a dimensionless equilibrium pressure drop as

$$b_{eq}^{*} = b_{eq}\sqrt{\frac{H}{V_o}} = \sqrt{\frac{-2(1-\frac{8}{3\pi}\eta)+2\sqrt{(1-\frac{8}{3\pi}\eta)^2+\frac{\Psi}{\pi}}}{\Psi}} \tag{3.1.18}$$

$$\Delta p_{eq}^{*} = \frac{\Delta p_{eq}}{E'}\sqrt{\frac{V_o}{H^3}} = \frac{\eta_{eq}}{2b_{eq}^{*}} \tag{3.1.19}$$

Figures 3.5-3.7 show the equilibrium surfaces of η_{eq}, b_{eq}^{*} and Δp_{eq}^{*} for various Γ and Ψ. Then the non-dimensional adhesion force at equilibrium, F_{Aeq}^{*}, and the dimensionless equilibrium combined surface deflection, u_{eq}^{*}, can be calculated from equations (2.1.36) and (2.1.39). The dimensionless equilibrium gap, h_{eq}^{*}, is then given by

$$h_{eq}^{*} = 1 + \frac{(r^{*}b_{eq}^{*})^2}{2}\Psi - u_{eq}^{*} \tag{3.1.20}$$

From the above equations, it is seen that the dimensionless system has two degrees of freedom with Γ and Ψ as the control variables.

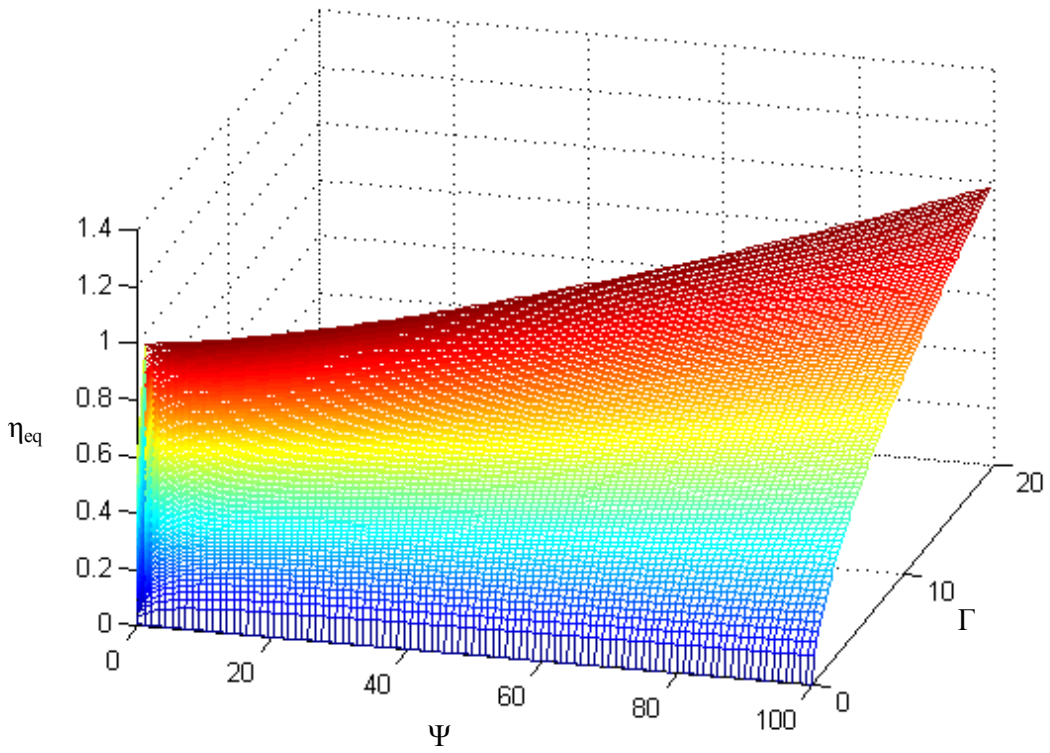

Figure 3.5 Equilibrium surface of η_{eq} before contact for various Γ and Ψ.

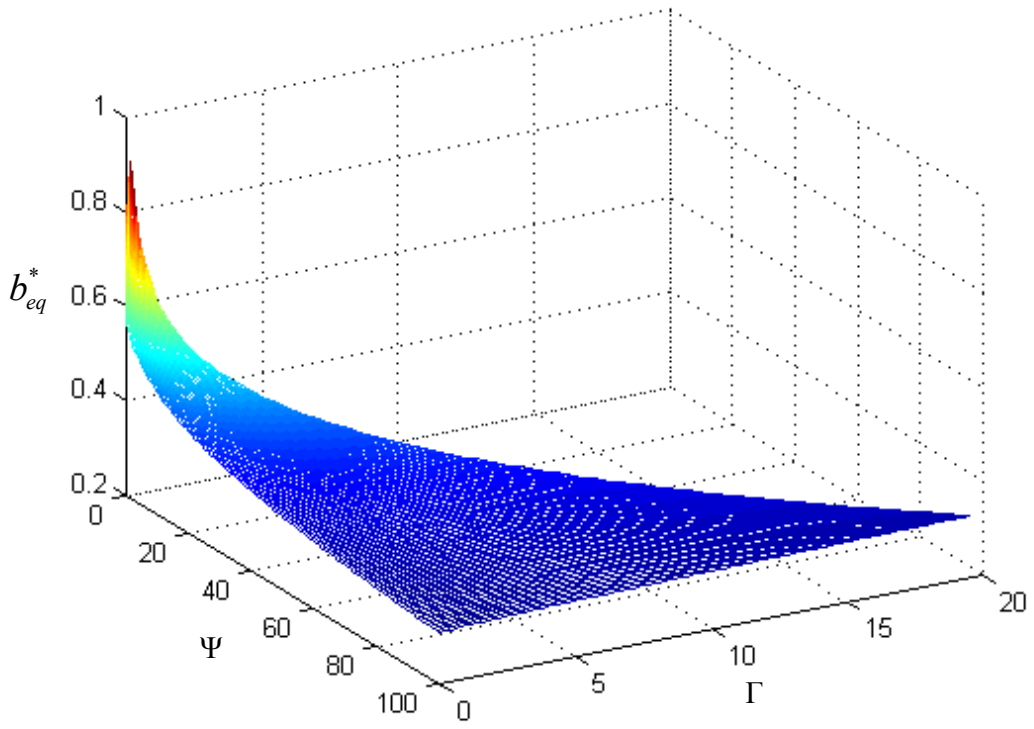

Figure 3.6 Equilibrium surface of b^*_{eq} before contact for various Γ and Ψ.

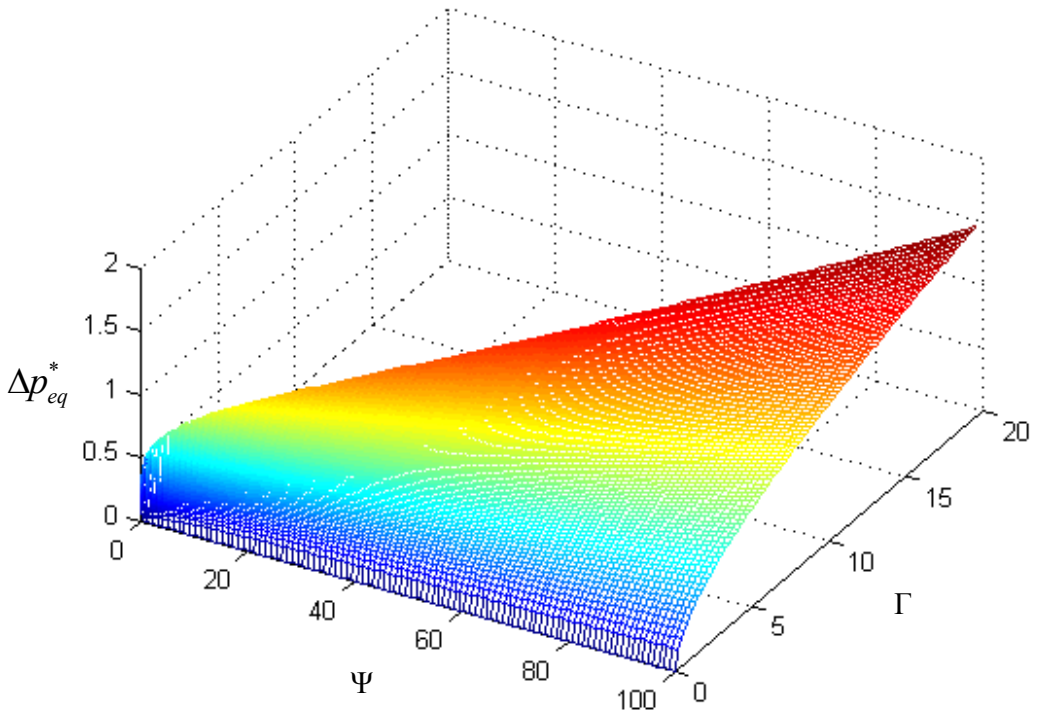

Figure 3.7 Equilibrium surface of Δp^*_{eq} before contact for various Γ and Ψ.

3.2 Equilibrium Configuration with Contact

A schematic of possible equilibrium configuration for sphere-sphere contact is shown in Figure 3.8. As the wetted radius b and the contact radius a are very small compared to the radii of the spheres, R_1 and R_2, one can ignore the influence of body curvature and perform an analysis similar to that done in section 2.3. Again, three quantities, the pressure drop across the meniscus (Δp), the meniscus position (b) and the contact radius (a), are sufficient to specify the equilibrium interface configuration.

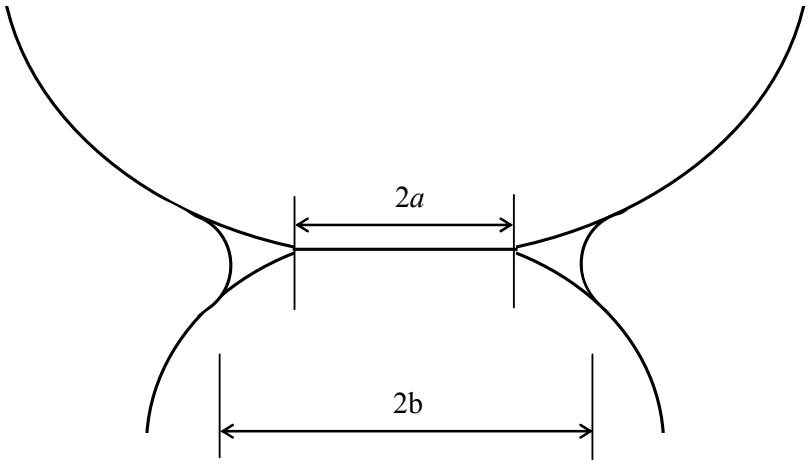

Figure 3.8 Schematic of the deformed interface between two elastic spheres connecting by a liquid bridge of volume V_o, with solid-solid contact.

The pressure distribution and the surface deflection in the interface after contact are summarized as below:

$$p(r)=\begin{cases}? & 0\le r\le a\\ -\Delta p & a<r\le b\\ 0 & r>b\end{cases} \tag{3.2.1}$$

$$u(r)=\begin{cases}H+\dfrac{r^2}{2R} & 0\le r\le a\\ ? & r>a\end{cases} \tag{3.2.2}$$

The unknown pressure distribution within the contact region (i.e., $p(r)$ for $0\le r\le a$) along with the unknown surface deflection outside of the contact region (i.e., $u(r)$ for $r>a$), can be solved using the influence coefficient method shown in section 2.3. The same discretization and influence coefficient matrix can be used here. For convenience, we still use vectors $\{r_{s1}\}$, $\{p_{s1}\}$, $\{u_{s1}\}$ and $\{h_{s1}\}$ to represent the radial position, the pressure distribution, the surface deflection and the gap in the contact region and use $\{r_{s2}\}$, $\{p_{s2}\}$, $\{u_{s2}\}$ and $\{h_{s2}\}$ to represent those out of the contact region. Now we know

$$h_{s1i}=0, \qquad 1\le i\le N+1 \tag{3.2.3}$$

$$p_{s2i}=-\Delta p, \qquad 1\le i\le N \tag{3.2.4}$$

$$u_{s1i}=H+\frac{r_{s1i}^{\ 2}}{2R}, \qquad 1\le i\le N+1 \tag{3.2.5}$$

The unknown pressures, $\{p_{s1}\}$, and deflections, $\{u_{s2}\}$, can then be solved from equations (2.3.15) and (2.3.16) and the gap outside the contact region, $\{h_{s2}\}$, can be computed by

$$h_{s2i}=H+\frac{r_{s2i}^{\ 2}}{2R}-u_{s2i}, \qquad 1\le i\le N \tag{3.2.6}$$

The conserved liquid volume is then represented as

$$\begin{aligned}V_o&=\int_a^b 2\pi r h(r)dr\\ &\approx \pi H(b^2-a^2)+\frac{\pi}{4R}(b^4-a^4)-\sum_{i=1}^{N}2\pi r_{s2i}u_{s2i}\Delta r_{s2}\end{aligned} \tag{3.2.7}$$

The energies stored at the interface can still be determined from equations (2.3.20)-(2.3.22).

For non-dimensionalization, we introduce dimensionless quantities

$$r^* = \frac{r}{b}$$

$$u^* = \frac{u}{H}$$

$$p^* = \frac{p}{\Delta p}$$

$$\eta = \frac{2\Delta p b}{E' H}$$

$$m = \frac{a}{b}$$

$$B = \frac{b^2}{RH}$$

$$\Psi = \frac{V_o}{RH^2}$$

$$\Gamma = \frac{\gamma_{LV}{}^2 \left(\frac{\cos\theta_1 + \cos\theta_2}{2} \right)^2 V_o}{E'^2 H^5}$$

$$\Phi = \frac{(\gamma_{SL_1} + \gamma_{SL_2}) - \gamma_{S12}}{\gamma_{LV}(\cos\theta_1 + \cos\theta_2)} = \frac{\Delta\gamma}{\gamma_{LV}(\cos\theta_1 + \cos\theta_2)} - 1$$

From equations (3.2.4) and (3.2.5), we get

$$p^*_{s2i} = -1, \qquad 1 \le i \le N \tag{3.2.7}$$

$$u^*_{s1i} = 1 + \frac{r^{*\,2}_{s1i}}{2} B, \qquad 1 \le i \le N+1 \tag{3.2.8}$$

For convenience, we decompose $\{u^*_{s1}\}$ into two (N+1) by 1 vectors $\{u^*_{s1H}\}$ and $\{u^*_{s1R}\}$, i.e.,

$$u^*_{s1i} = u^*_{s1Hi} + u^*_{s1Ri} \tag{3.2.9}$$

where

$$u^*_{s1Hi} = 1 \tag{3.2.10}$$

$$u^*_{s1Ri} = \frac{r^{*\,2}_{s1i}}{2} B \tag{3.2.11}$$

The dimensionless unknown pressures, $\{p^*_{s1}\}$, and unknown deflections, $\{u^*_{s2}\}$, can still be solved by equation (2.3.37) and equation (2.3.38) with new deflections in the contact region, $\{u^*_{s1}\}$, shown by equation (3.2.9). Substituting equation (3.2.9) into equation (2.3.37), we get

$$\begin{aligned}\{p^*_{s1}\} &= \frac{\pi E' H}{4b\Delta p}[c^*_{s11}]^{-1}\{u^*_{s1H}\} + \frac{\pi E' b}{8R\Delta p}[c^*_{s11}]^{-1}\{u^*_{s1R}\} - [c^*_{s11}]^{-1}[c^*_{s12}]\{p^*_{s2}\} \\ &= \frac{\pi}{2\eta}\{p^*_{s11}\} + \frac{\pi B}{4\eta}\{p^*_{s13}\} - \{p^*_{s12}\}\end{aligned} \tag{3.2.12}$$

where

$$\{p^*_{s11}\} = [c^*_{s11}]^{-1}\{u^*_{s1H}\} \tag{3.2.13}$$

$$\{p^*_{s12}\} = [c^*_{s11}]^{-1}[c^*_{s12}]\{p^*_{s2}\} \tag{3.2.14}$$

$$\{p^*_{s13}\} = [c^*_{s11}]^{-1}\{u^*_{s1R}\} \tag{3.2.15}$$

Substitute this new equation of $\{p^*_{s1}\}$ into equation (2.3.38). The dimensionless unknown deflections, $\{u^*_{s2}\}$, is given by

$$\begin{aligned}\{u^*_{s2}\} &= \frac{4b\Delta p}{\pi E' H}[c^*_{s21}]\{p^*_{s1}\} + \frac{4b\Delta p}{\pi E' H}[c^*_{s22}]\{p^*_{s2}\} \\ &= \frac{2\eta}{\pi}[c^*_{s21}]\{p^*_{s1}\} + \frac{2\eta}{\pi}[c^*_{s22}]\{p^*_{s2}\} \\ &= \{u^*_{s21}\} + \frac{B}{2}\{u^*_{s24}\} - \frac{2\eta}{\pi}\left(\{u^*_{s22}\} - \{u^*_{s23}\}\right)\end{aligned} \tag{3.2.16}$$

where

$$\{u^*_{s21}\} = [c^*_{s21}][c^*_{s11}]^{-1}\{u^*_{s1H}\} \tag{3.2.17}$$

$$\{u^*_{s22}\} = [c^*_{s21}][c^*_{s11}]^{-1}[c^*_{s12}]\{p^*_{s2}\} \tag{3.2.18}$$

$$\{u^*_{s23}\} = [c^*_{s22}]\{p^*_{s2}\} \tag{3.2.19}$$

$$\{u^*_{s24}\} = [c^*_{s21}][c^*_{s11}]^{-1}\{u^*_{s1R}\} \tag{3.2.20}$$

Non-dimensionalizing equation (3.2.6) leads to

$$\Psi = \pi B(1-m^2) + \frac{\pi}{4}B^2(1-m^4) - 2\pi B\sum_{i=1}^{N} r^*_{s2i}\Delta r^*_{s2}u^*_{s2i} \tag{3.2.21}$$

Substituting equation (3.2.16) into the above equation yields,

$$\Psi = \pi(1-m^2-\lambda_1+\lambda_2\eta)B + \frac{\pi}{4}(1-m^4-\lambda_6)B^2 \tag{3.2.22}$$

where

$$\lambda_1 = 2\sum_{i=1}^{N} r^*_{s2i}\Delta r^*_{s2}u^*_{s21i} \tag{3.2.23}$$

$$\lambda_2 = \frac{4}{\pi}\sum_{i=1}^{N} r^*_{s2i}\Delta r^*_{s2}(u^*_{s22i} - u^*_{s23i}) \tag{3.2.24}$$

$$\lambda_6 = 4\sum_{i=1}^{N} r^*_{s2i}\Delta r^*_{s2}u^*_{s24i} \tag{3.2.25}$$

Solve equation (3.2.22) for B, we get

$$B = \frac{-2X + 2\sqrt{X^2 + \frac{\Psi}{\pi}Y}}{Y} \tag{3.2.26}$$

where

$$X = (1-m^2-\lambda_1+\lambda_2\eta) \tag{3.2.27}$$

$$Y = (1-m^4-\lambda_6) \tag{3.2.28}$$

Non-dimensionalizing the total free energy U_T in equation (2.3.22) according to equation (3.1.10), we get the dimensionless system free energy U_T^* given by

$$\begin{aligned} U_T^* &= -2\sqrt{\frac{\Gamma}{\Psi}}(1+\Phi m^2)B \\ &\quad + \frac{\eta B^{1/2}}{2}\left[\sum_{i=1}^{N+1} r_{s1i}^* p_{s1i}^* u_{s1i}^* \Delta r_{s1}^* + \sum_{i=1}^{N} r_{s2i}^* p_{s2i}^* u_{s2i}^* \Delta r_{s2}^*\right] \end{aligned} \tag{3.2.29}$$

Substituting equations (3.2.12) and (3.2.16) into equation (3.2.29), we get

$$\begin{aligned} U_T{}^* &= -2\sqrt{\frac{\Gamma}{\Psi}}(1+\Phi m^2)B + (\frac{\pi}{4}\lambda_3 - \frac{1}{2}\lambda_4\eta - \frac{1}{\pi}\lambda_5\eta^2)B^{1/2} \\ &\quad + (\frac{\pi}{8}\lambda_7 - \frac{1}{4}\lambda_8\eta)B^{3/2} + \frac{\pi}{16}\lambda_9 B^{5/2} \end{aligned} \tag{3.2.30}$$

where

$$\lambda_3 = \sum_{i=1}^{N+1} r_{s1i}^* \Delta r_{s1}^* p_{s11i}^* u_{s1Hi}^* \tag{3.2.31}$$

$$\lambda_4 = \sum_{i=1}^{N+1} r_{s1i}^* \Delta r_{s1}^* p_{s12i}^* u_{s1Hi}^* - \sum_{i=1}^{N} r_{s2i}^* \Delta r_{s2}^* p_{s2i}^* u_{s21i}^* \tag{3.2.32}$$

$$\lambda_5 = \sum_{i=1}^{N} r_{s2i}^* \Delta r_{s2}^* p_{s2i}^* (u_{s22i}^* - u_{s23i}^*) \tag{3.2.33}$$

$$\lambda_7 = \sum_{i=1}^{N+1} r_{s1i}^* \Delta r_{s1}^* p_{s11i}^* u_{s1Ri}^* + \sum_{i=1}^{N+1} r_{s1i}^* \Delta r_{s1}^* p_{s13i}^* u_{s1Hi}^* \tag{3.2.34}$$

$$\lambda_8 = \sum_{i=1}^{N+1} r_{s1i}^* \Delta r_{s1}^* p_{s12i}^* u_{s1Ri}^* - \sum_{i=1}^{N} r_{s2i}^* \Delta r_{s2}^* p_{s2i}^* u_{s24i}^* \tag{3.2.35}$$

$$\lambda_9 = \sum_{i=1}^{N+1} r_{s1i}^* \Delta r_{s1}^* p_{s13i}^* u_{s1Ri}^* \tag{3.2.36}$$

Factors λ_1~λ_9 depend on N and the dimensionless parameter m. When N goes to infinity, they converge to some functions of m. Comparing these factors with those found in section 2.3, we can see that λ_1~λ_5 listed above are exactly the same as that given by

equations (2.3.48)-(2.3.49) and (2.3.52)-(2.3.54), while λ_6~λ_9 are new factors. Figures 3.9-3.12 show the variations of λ_6~λ_9 with m and the convergence when N becomes large. By curve fitting, one gets

$$\lambda_6 = -0.0251m + 0.2577m^2 + 0.6454m^3 + 0.9474m^4 - 1.8163m^5 \tag{3.2.37}$$

$$\lambda_7 = 0.0444m - 0.0783m^2 + 0.1439m^3 + 0.9920m^4 - 0.5686m^5 \tag{3.2.38}$$

$$\lambda_9 = 0.0935m^2 - 0.4463m^3 + 0.6722m^4 \tag{3.2.39}$$

Again, the relative errors of all these curve fittings are less than 0.3%. Like λ_4, the effect of λ_8 can be neglected, therefore λ_8 is set to be zero for simplicity.

$$\lambda_8 = 0 \tag{3.2.40}$$

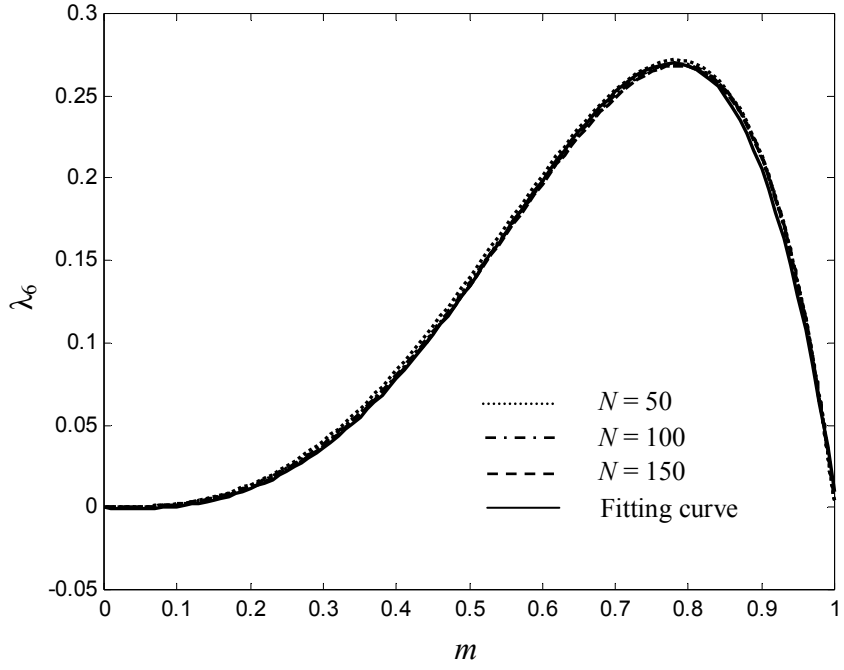

Figure 3.9 Variation of coefficient λ_6 with m and N.

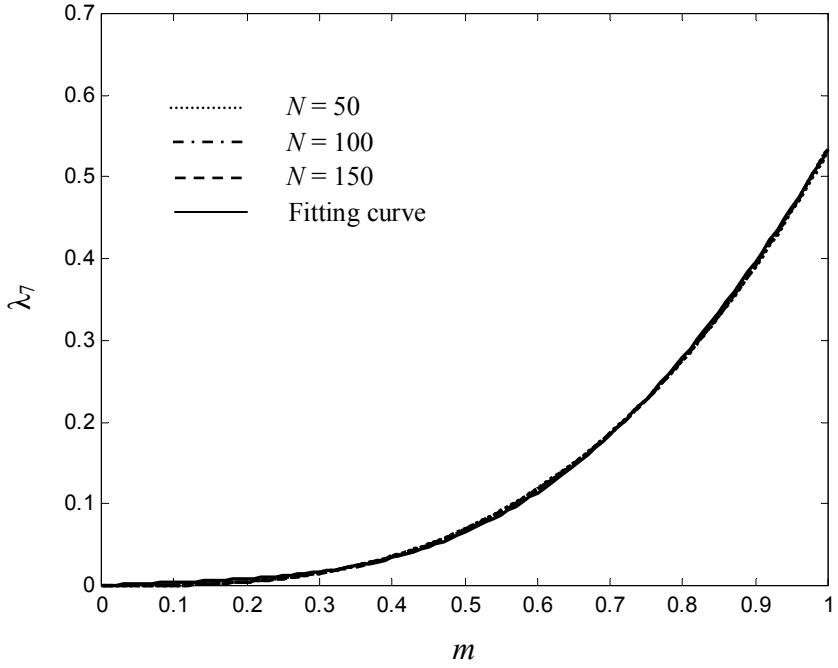

Figure 3.10 Variation of coefficient λ_7 with m and N.

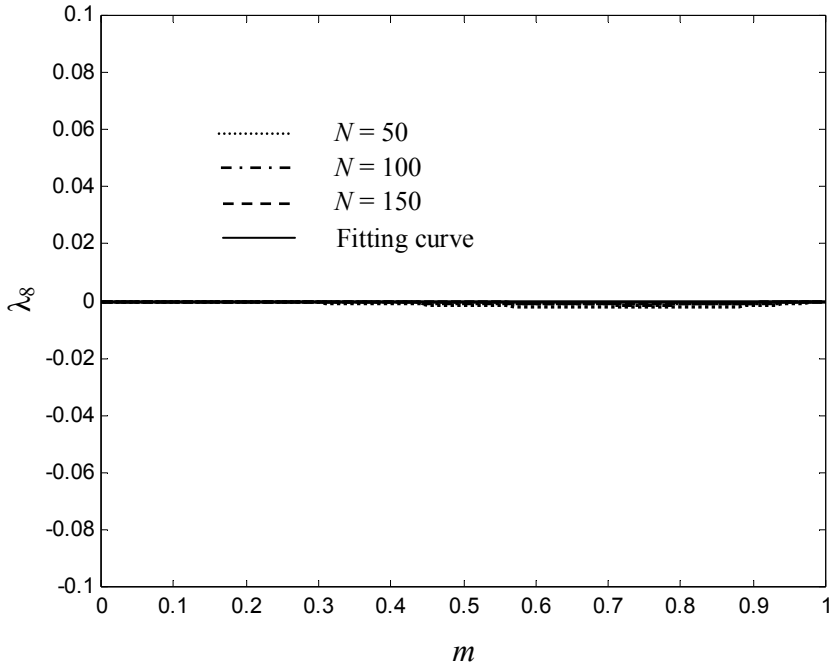

Figure 3.11 Variation of coefficient λ_8 with m and N.

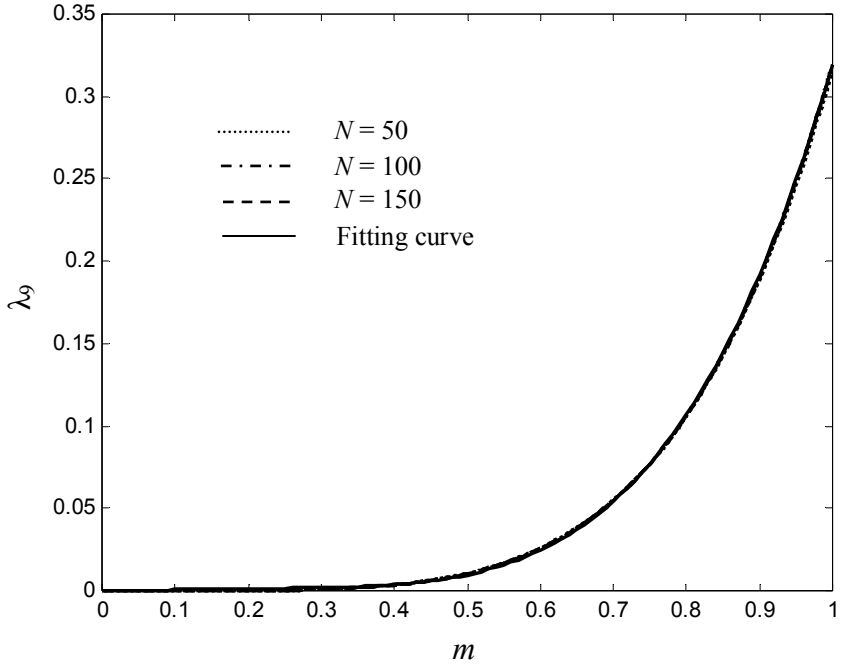

Figure 3.12 Variation of coefficient λ_9 with m and N.

Substituting the fitted equations of factors λ_1~λ_9 into equation (3.2.30), we get a closed-form expression of the dimensionless system free energy U_T^*. We can see that U_T^* depends on η, m, Γ, Ψ, and Φ. For given Γ, Ψ, and Φ, a particular combination of η and m represents a provisional equilibrium contact configuration as described in section 2.3. There are physical constraints on η and m to form a provisional equilibrium contact configuration. First, m must be greater than or equal to 0 by definition.

$$m \geq 0 \tag{3.2.41}$$

Second, in order to obtain a real, positive value of B and hence a practical wetted radius b, equation (3.2.26) requires that

$$X^2 + \frac{\Psi}{\pi} Y \geq 0 \tag{3.2.42}$$

i.e.,

$$(1 - m^2 - \lambda_1 + \lambda_2 \eta)^2 + \frac{\Psi}{\pi}(1 - m^4 - \lambda_6) \geq 0 \tag{3.2.43}$$

Equation (3.2.43) sets up the upper bound of *m*. When plotting the left-hand-side function vs. *m* for various η and Ψ, one can see that the maximum possible value of *m* increases with increasing η and decreases with increasing Ψ. In all the cases of interest in the present work, this maximum value falls in a narrow region from 0.9922 to 1. For simplicity, the upper bound of *m* is set as 0.9922 in this study. Because only a small fraction of configurations would have a ratio of a/b greater than 0.99, there is little loss of generality with this assumption.

When a provisional configuration corresponds to a local energy minimum, a stable equilibrium is reached, at which point the following conditions are satisfied

$$\frac{\partial U_T^*}{\partial \eta} = 0 \tag{3.2.44}$$

$$\frac{\partial U_T^*}{\partial m} = 0 \tag{3.2.45}$$

$$\frac{\partial^2 U_T^*}{\partial \eta^2} > 0 \tag{3.2.46}$$

$$\frac{\partial^2 U_T^*}{\partial \eta^2} \frac{\partial^2 U_T^*}{\partial m^2} - \left(\frac{\partial^2 U_T^*}{\partial \eta \partial m} \right)^2 > 0 \tag{3.2.47}$$

Solving equations (3.2.44) and (3.2.45) simultaneously for η and *m*, and checking with inequalities (3.2.46) and (3.2.47), we can find the stable equilibrium contact

configuration, represented by a solution of equations (3.2.44) and (3.2.45), for a given set of parameters Γ, Ψ, and Φ. Thus the dimensionless system of liquid-mediated sphere contact has three degrees of freedom with Γ, Ψ, and Φ as the control variables.

Numerical solutions of equations (3.2.44) and (3.2.45) are pursued here. The numerical method and the following description are borrowed from Feng's paper[34]. To solve the equation set (equations (3.2.44) and (3.2.45)), the Newton-Raphson method[49] is used. The equations can be rewritten in a vector form:

$$\underline{F}(\underline{x}) = \underline{0} \tag{3.2.48}$$

Where $\underline{x} \equiv (\eta, m)^T$ and $\underline{F} \equiv (\partial U_T^* / \partial \eta, \partial U_T^* / \partial m)^T$, with superscript T denoting the transpose. Starting from an initial guess $\underline{x}_{(0)}$, successive iterates are determined by

$$\underline{x}_{(i+1)} = \underline{x}_{(i)} + \delta \underline{x} \tag{3.2.49}$$

with the solution of

$$\underline{\underline{J}}(\underline{x}_{(i)})\, \delta \underline{x} = -\underline{F}(\underline{x}_{(i)}) \tag{3.2.50}$$

where $\underline{\underline{J}}$ is the Jacobian matrix, i.e.,

$$\underline{\underline{J}} = \begin{bmatrix} \dfrac{\partial^2 U_T^*}{\partial \eta^2} & \dfrac{\partial^2 U_T^*}{\partial \eta \partial m} \\ \dfrac{\partial^2 U_T^*}{\partial m \partial \eta} & \dfrac{\partial^2 U_T^*}{\partial m^2} \end{bmatrix} \quad \text{or} \quad \underline{\underline{J}} \equiv \underline{F}_{,\underline{x}} \tag{3.2.51}$$

At each iteration, the Jacobian matrix $\underline{\underline{J}}$ is evaluated with the values of unknowns $\underline{x}_{(i)}$ determined in the previous iteration and the resulting system is solved for $\delta \underline{x}$. The iteration is continued until both the uniform norm $\|\underline{F}\|$ and relative error of the solution, defined as $\max\left(\left|\delta\eta/\eta\right|, \left|\delta m/m\right|\right)$, become less than 10^{-6}.

The Newton-Raphson method usually exhibits quadratic convergence to the solution. It is critical here to make an initial estimate of the solution $\underline{x}_{(0)}$ that falls within the domain of convergence. In the present work, when necessary, an initial guess of the solution can be made graphically by looking for a local minimum on the contour figure of U_T^* computed from equation (3.2.30).

For a given set of the parameters Γ, Ψ, and Φ, the equation set (3.2.48) may admit a unique solution, multiple solutions or no solution. To investigate the structure of the solution space, continuation from an existing solution is desirable by varying a physical parameter in the governing equation, such as Γ, Ψ, or Φ. For example, a solution at $\Gamma = \Gamma_0 + \delta\Gamma$ may be obtained by the Newton-Raphson method in four or five iterations, using an existing solution at Γ_0 as the initial guess $\underline{x}_{(0)} = \underline{x}(\Gamma_0)$. Such a simple procedure is called zeroth-order continuation. With the available Jacobian matrix $\underline{\underline{J}}(\Gamma_0)$ already computed for Newton iterations for $\underline{x}(\Gamma_0)$, a more cost-effective approach would be the first-order continuation[36] because the corresponding initial guess

$$\underline{x}_{(0)} = \underline{x}(\Gamma_0) - \underline{\underline{J}}^{-1}(\Gamma_0)\underline{F}_{,\Gamma}(\Gamma_0)(\Gamma - \Gamma_0) \tag{3.2.52}$$

is often closer to the sought solution $\underline{x}(\Gamma)$ than $\underline{x}(\Gamma_0)$, where $\underline{F}_{,\Gamma}$ stands for the derivative of $\underline{F}$ with respect to Γ. However, zeroth-order and first-order continuations fail at bifurcation points and turning points in the solution space where the Jacobian matrix becomes singular and the solution is not unique. Turning points in the solution space of contacting elastic spheres have been shown to appear in the non-contact configurations (see Figure 3.3) and reported by Greenwood[32] and Feng[34] for dry contact with folded load-approach curves for large values of Tabor's parameter. To

obtain solutions using continuation near a turning point, Keller's method of arc-length continuation[36,37] is used. The essence of Keller's method is to treat the arc-length along a solution branch as the continuation parameter, with respect to which the solution becomes unique at the turning points. In other words, the solution $\underline{x}$ and the physical parameter (e.g. Γ) are both parameterized by the arc-length, s, along the solution branch; namely, $\underline{x} = \underline{x}(s)$ and $\Gamma = \Gamma(s)$. The equation defining the arc-length along the solution branch is[34]:

$$\left\langle \underline{x}_{,s}, \underline{x}_{,s} \right\rangle + \Gamma_{,s}{}^2 - 1 = 0 \tag{3.2.53}$$

where the subscript s stands for differentiation with respect to s and $< , >$ is the Euclidean inner product of vectors. Linearized around a known solution $(\underline{x}(s_0), \Gamma(s_0))$, equation (3.2.53) becomes

$$\begin{aligned} G(\underline{x}(s), \Gamma(s), s) \equiv & \left\langle \underline{x}_{,s}(s_0), (\underline{x}(s) - \underline{x}(s_0)) \right\rangle \\ & + \Gamma_{,s}(s_0)(\Gamma(s) - \Gamma(s_0)) - (s - s_0) \\ & = 0 \end{aligned} \tag{3.2.54}$$

To satisfy equation (3.2.54), the new solution must lie on a hyperplane perpendicular to the tangent vector evaluated at $s = s_0$ and at a distance $|s - s_0|$ from $(\underline{x}(s_0), \Gamma(s_0))$. Simultaneously solving equations (3.2.48) and (3.2.54) by the Newton-Raphson method means to iteratively determine $\delta\underline{x}$ and $\delta\Gamma$ as solution of

$$\begin{bmatrix} \underline{F}_{,\underline{x}} & \underline{F}_{,\Gamma} \\ G_{,\underline{x}} & G_{,\Gamma} \end{bmatrix} \begin{bmatrix} \delta\underline{x} \\ \delta\Gamma \end{bmatrix} = -\begin{bmatrix} \underline{F} \\ G \end{bmatrix} \tag{3.2.55}$$

The augmented Jacobian is non-singular at turning points. Therefore, turning points can be passed smoothly along a solution branch and quadratic convergence of Newton

iteration can be sustained. The entries in the last row of the augmented Jacobian, i.e. $G_{,\underline{x}} = \underline{x}_{,s}(s_0)$ and $G_{,\Gamma} = \Gamma_{,s}(s_0)$, are obtained by solving

$$\underline{\underline{J}}\,\underline{x}_{,\Gamma} = -\underline{F}_{,\Gamma}(s_0) \tag{3.2.56}$$

for $\underline{x}_{,\Gamma}$ at s=s_0, and then determining $\Gamma_{,s}(s_0)$ and $\underline{x}_{,s}(s_0)$ as:

$$\Gamma_{,s}(s_0) = \pm(1 + \langle \underline{x}_{,\Gamma}, \underline{x}_{,\Gamma} \rangle)^{-1/2} \tag{3.2.57}$$

and

$$\underline{x}_{,s}(s_0) = \Gamma_{,s}(s_0)\underline{x}_{,\Gamma} \tag{3.2.58}$$

Both positive and negative signs can be used in front of the square root term in equation (3.2.57). The positive sign is used when Γ and s increase in the same direction and the negative sign is used when Γ and s increase in the opposite direction. Because the last row equation (3.2.55) in corresponds to a linear equation (3.2.54) with respect to the unknowns $\underline{x}(s)$ and $\Gamma(s)$, computations of equations (3.2.56)-(3.2.58) for $\Gamma_{,s}(s_0)$ and $\underline{x}_{,s}(s_0)$ are needed only once before starting the iterations. As in first-order continuation, the Jacobian matrix $\underline{\underline{J}}(\Gamma_0)$ computed for Newton iteration at the previous step of convergence for $\underline{x}(\Gamma_0)$ can be used for the next step of solving equation (3.2.56), by virtue of the bordering algorithm for arc-length continuation[37] as follows.

At each Newton-Raphson iteration, two equations

$$\underline{\underline{J}}\,\underline{y} = \underline{F}_{,\Gamma} \tag{3.2.59}$$

and

$$\underline{\underline{J}}\,\underline{z} = -\underline{F} \tag{3.2.60}$$

are solved, where $\underline{y}$ and $\underline{z}$ are two intermediate variables; then $\delta\underline{x}$ and $\delta\Gamma$ are determined by

$$\delta\Gamma = (\langle G_{,\underline{x}}, \underline{z} \rangle + G) / (\langle G_{,\underline{x}}, \underline{y} \rangle - G_{,\Gamma}) \tag{3.2.61}$$

and

$$\delta\underline{x} = \underline{z} - \delta\Gamma\, \underline{y} \tag{3.2.62}$$

Thus, one factorization of $\underline{\underline{J}}$ can be used several times in solving equations in (3.2.56), (3.2.59) and (3.2.60). The bordering algorithm can be used as long as $\underline{\underline{J}}$ is non-singular; namely, as long as the continuation straddles the turning point instead of "hitting" a very small neighborhood around the turning point. In the present work, the latter never occurred when using the bordering algorithm. As a summary, the flow chart of the calculation is shown in Figure 3.13.

The solution space of the equation set (3.2.44) and (3.2.45) is shown in Figure 3.14, where η_{eq}, m_{eq} represent the value of η and m satisfying equations (3.2.44) and (3.2.45) for a given set of Γ, Ψ, and Φ. When (η_{eq}, m_{eq}) satisfy the inequalities (3.2.46) and (3.2.47), they represent a stable equilibrium contact configuration. From this combination of (η_{eq}, m_{eq}), we can calculate the dimensionless equilibrium wetted radius, contact radius and pressure drop as

$$b^*_{eq} = b_{eq}\sqrt{\frac{H}{V_o}} = \sqrt{\frac{B_{eq}}{\Psi}} \tag{3.2.63}$$

$$a^*_{eq} = a_{eq}\sqrt{\frac{H}{V_o}} = m_{eq} b^*_{eq} \tag{3.2.64}$$

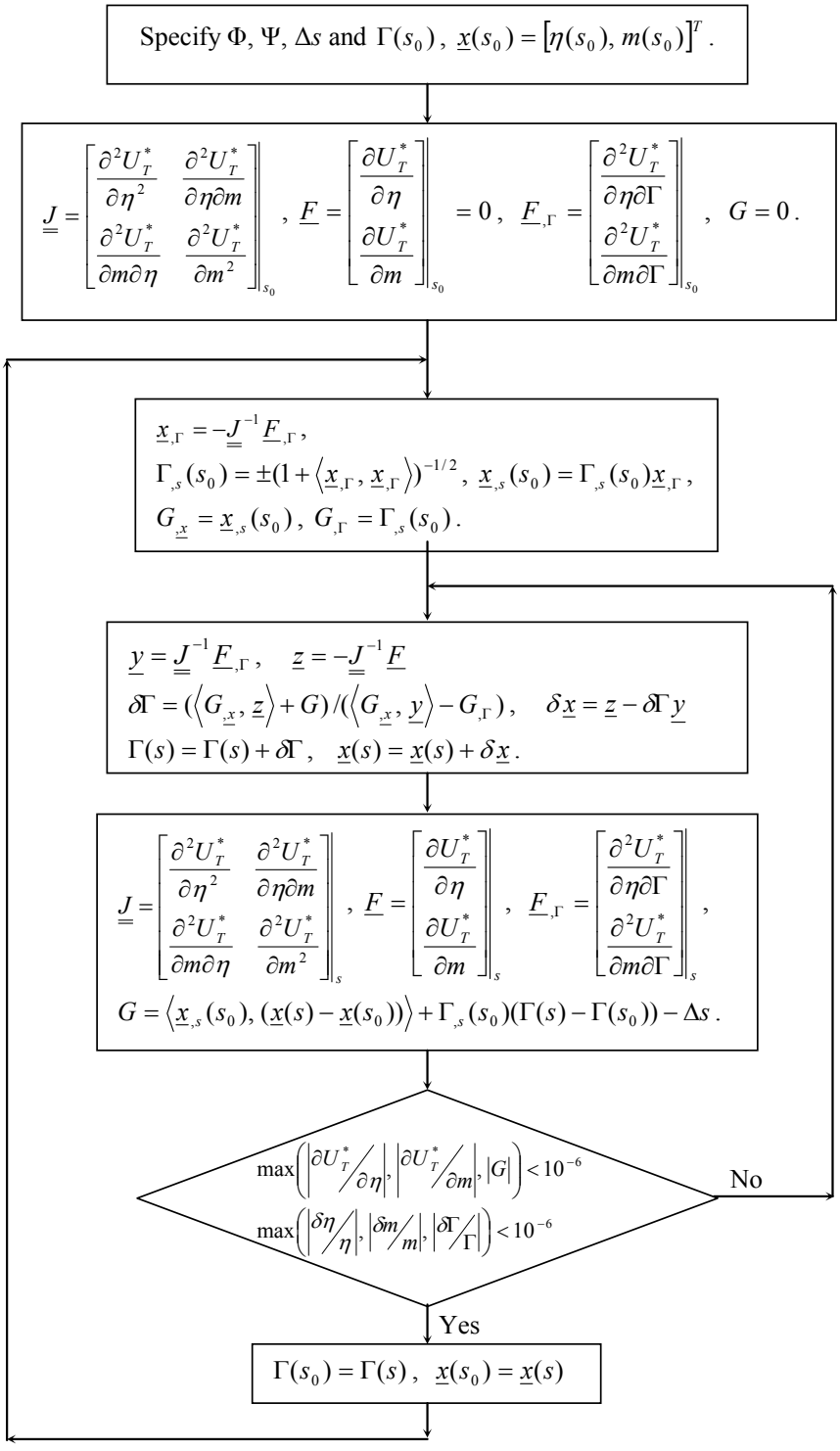

Figure 3.13 Flow chart of Newton-Raphson iteration with arc-length continuation for investigation of the structure of the solution space of equation set (3.2.44) and (3.2.45).

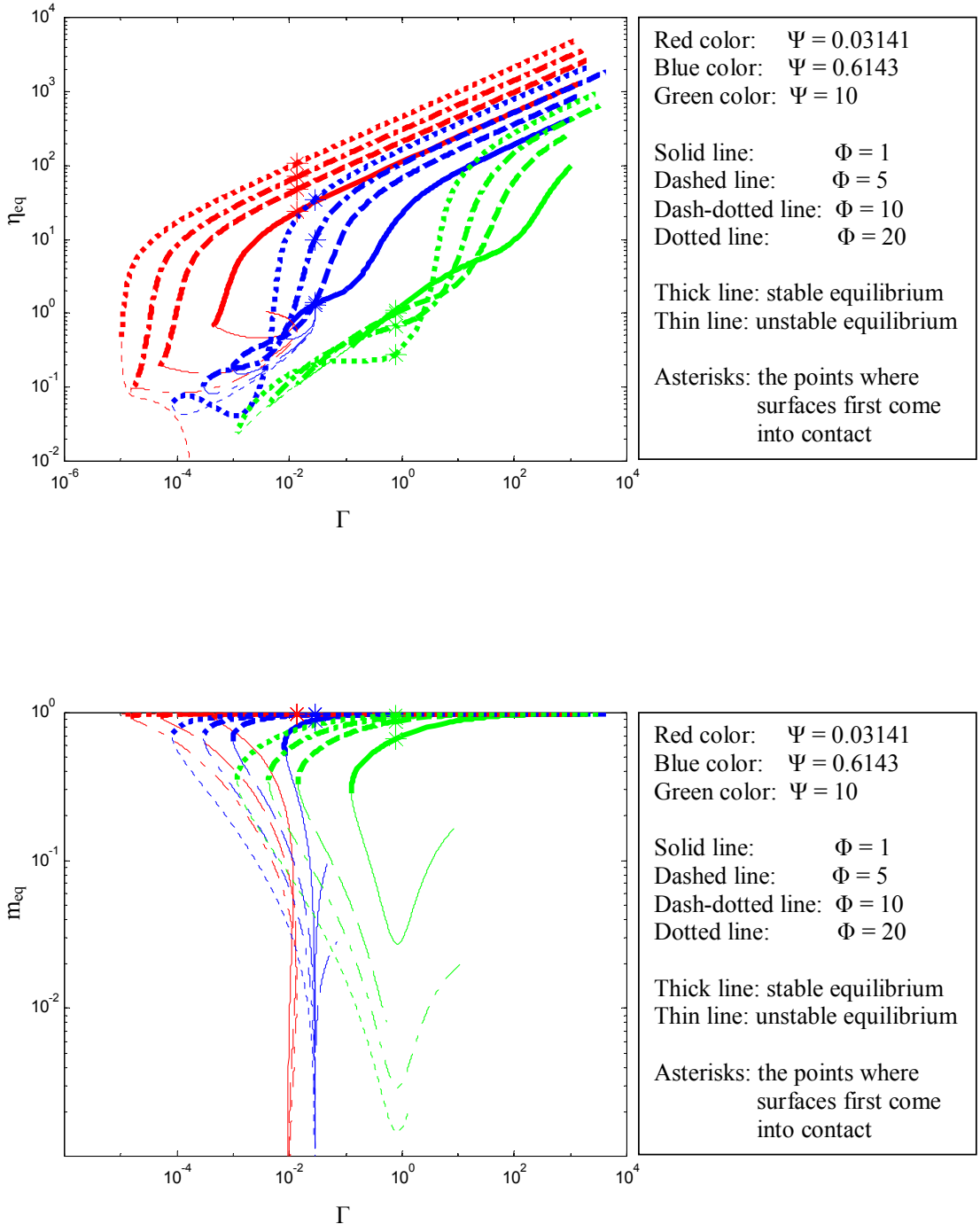

Figure 3.14 The solution space of the equation set (3.2.44) and (3.2.45) for various Φ and Ψ.

$$\Delta p_{eq}^{*} = \frac{\Delta p_{eq}}{E'}\sqrt{\frac{V_o}{H^3}} = \frac{\eta_{eq}}{2b_{eq}^{*}} \tag{3.2.65}$$

where B_{eq} can be calculated by substituting (η_{eq}, m_{eq}) into equation (3.2.26). The results are shown in Figures 3.15-3.17.

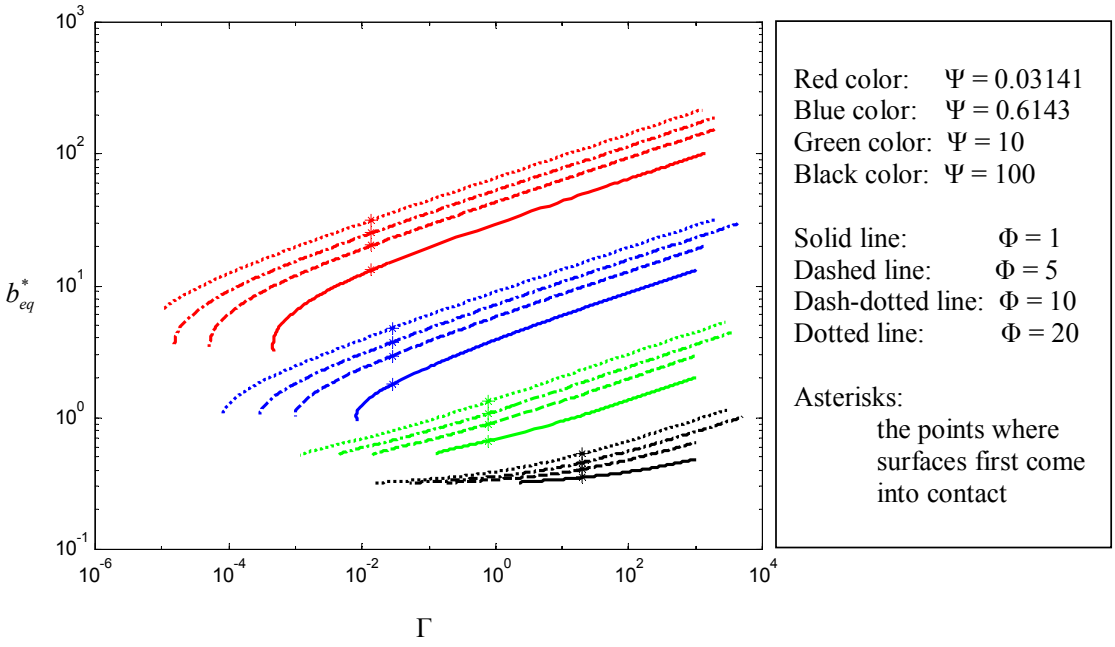

Figure 3.15 Variation of dimensionless equilibrium wetted radius, b_{eq}^{*}, with control variables Γ, Ψ and Φ for positive rigid surface separation, H.

Figure 3.15 shows the variation of the dimensionless wetted radius, b_{eq}^{*} with Γ for various Ψ and Φ. In general, for given Ψ and Φ, the dimensionless wetted radius, b_{eq}^{*} increases with increasing Γ, and when Γ is fixed, b_{eq}^{*} decreases with increasing Ψ and decreasing Φ. For very large Ψ and small Γ, b_{eq}^{*} tends to be independent of Φ and Γ. This

is because, for these combinations of Ψ and Γ, the capillary effect is weak, and the influence of surface deformation, which is caused by the capillary force and solid-solid interaction, on the interfacial space is negligible, considering the large size of the liquid bridge.

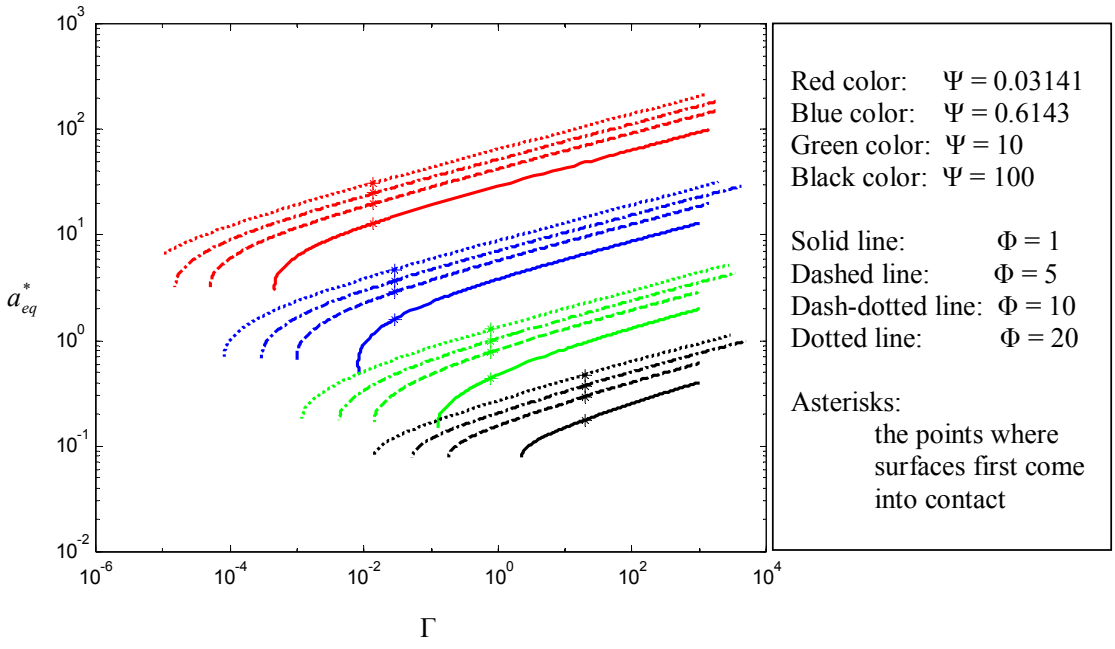

Figure 3.16 Variation of dimensionless equilibrium contact radius, a^*_{eq}, with control variables Γ, Ψ and Φ for positive rigid surface separation, H.

Figure 3.16 shows how the dimensionless contact radius, a^*_{eq} depends on Γ, Ψ and Φ. For given Ψ and Φ, a^*_{eq} increases with increasing Γ. When Γ is large, the curve in the log-log plot is linear. But for small Γ, the curve curls down. As Γ decreases, the slope of the curve gradually increases and becomes infinity at certain value of Γ, indicating a

jump at the interface. When Ψ increases, a_{eq}^{*} decreases and the linear region of the curve shrinks, i.e., the non-linearity appears at relative higher value of Γ. When Φ increases, a_{eq}^{*} increases and the linear region of the curve enlarges, i.e., the non-linearity appears at relative lower value of Γ.

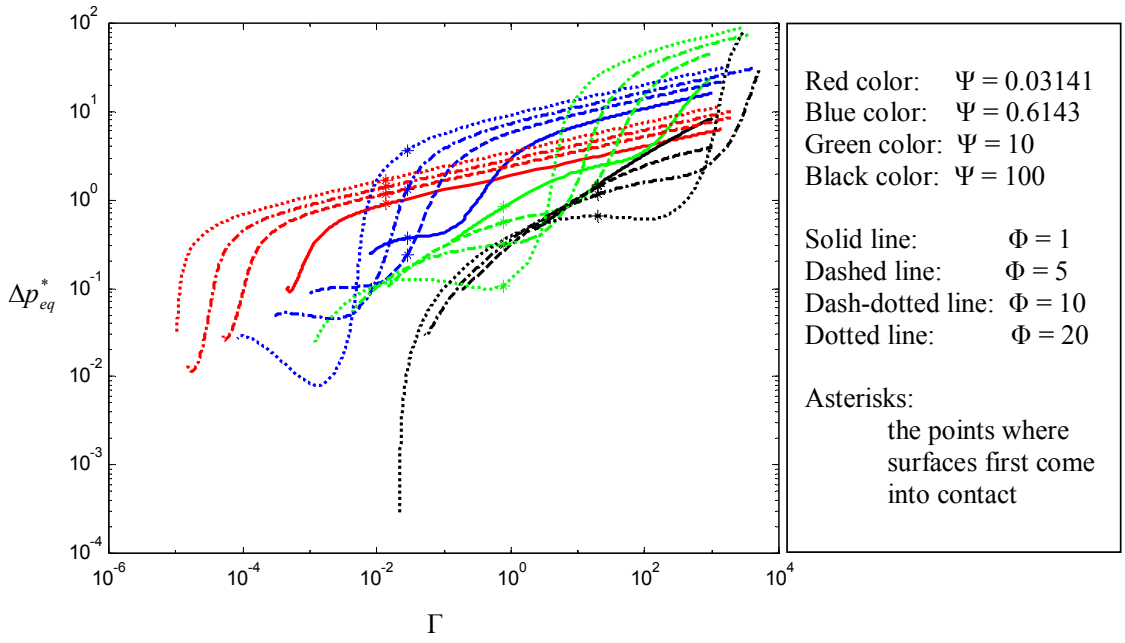

Figure 3.17 Variation of dimensionless equilibrium pressure drop, Δp_{eq}^{*}, with control variables Γ, Ψ and Φ for positive rigid surface separation, *H*.

For large Γ , small Ψ, the curves in Figure 3.16 are linear and can be fitted by

$$a_{eq}^{*} = \beta(\Phi)\Gamma^{1/6}\Psi^{-2/3} \tag{3.2.66}$$

where

$$\beta(\Phi) = 2.342(\Phi + 1)^{1/3} \tag{3.2.67}$$

If we substitute for Φ, Ψ and Γ, the dimensional equilibrium contact radius, a_{eq}, is then given by

$$a_{eq} = 1.859\left(\frac{R^2\Delta\gamma}{E'}\right)^{1/3} \tag{3.2.68}$$

Equation (3.2.68) is very close (within 1.4% relative error) to the JKR prediction of equilibrium contact radius at zero interference ($a_{eq} = \left(\frac{2\pi R^2\Delta\gamma}{E'}\right)^{1/3}$)[24], which deals with the contact of spheres in the absence of liquid. It shows that the equilibrium contact radius is independent of both the liquid volume of the bridge, V_o, and the original minimum sphere-sphere separation, H. The result makes sense because when the original minimum sphere-sphere separation, H, goes to zero (zero interference), Γ goes to infinity. For moderate R, small Ψ with small H implies very small V_o. But since $\frac{\Gamma}{\Psi} = \frac{\gamma_{LA}^2\left(\frac{\cos\theta_1 + \cos\theta_2}{2}\right)^2 R}{E'^2 H^3}$, Γ becomes much greater than Ψ as $H \to 0$. Thus large Γ and small Ψ can be interpreted as correspond to small H and small V_o. In this case, the liquid in the bridge is squeezed out to form a large but thin annulus around the contact region, and the wetted area on the surface becomes so small comparing with the large contact area that its influence on the contact can be neglected. Therefore, the equilibrium contact radius converges to the dry contact radius at zero interference when Γ goes to infinity and Ψ goes to zero.

For small Γ and large Ψ, the curves in Figure 3.16 are nonlinear. If we still fit the nonlinear part curves with a function in the form of

$$a_{eq}^{*} = \beta(\Phi)\Gamma^{x_1}\Psi^{-x_2}, \tag{3.2.69}$$

we can see that both x_1 and x_2 increases with decreasing Γ, but x_2 grows a little faster. These effects make the dimensional equilibrium contact radius, a_{eq}, decrease with increasing H and V_o.

Negative *H*

It should be pointed out that the above analysis is done with a positive H in consideration. For sphere contact, negative H is possible, which means that the two spheres are pressed together. The analysis for a negative H is nearly the same as the one for a positive H. Only now $H = -|H|$, so we define

$$u^{*} = \frac{u}{|H|} \tag{3.2.70}$$

$$\eta = \frac{2\Delta pb}{E'|H|} \tag{3.2.71}$$

$$B = \frac{b^2}{R|H|} \tag{3.2.72}$$

$$\Psi = \frac{V_o}{R|H|^2} = \frac{V_o}{RH^2} \tag{3.2.73}$$

$$\Gamma = \frac{\gamma_{LV}{}^2\left(\dfrac{\cos\theta_1 + \cos\theta_2}{2}\right)^2 V_o}{E'^2|H|^5} \tag{3.2.74}$$

The negative sign of H creates differences in the expressions for dimensionless surface deformations and pressure distributions.

$$u_{s1i}^{*} = -1 + \frac{r_{s1i}^{*\,2}}{2}B = -u_{s1Hi}^{*} + u_{s1Ri}^{*}, \qquad 1 \le i \le N+1 \tag{3.2.75}$$

$$\begin{aligned}\left\{p_{s1}^{*}\right\} &= -\frac{\pi E^{'}\left|H\right|}{4b\Delta p}\left[c_{s11}^{*}\right]^{-1}\left\{u_{s1H}^{*}\right\}+\frac{\pi E^{'}b}{8R\Delta p}\left[c_{s11}^{*}\right]^{-1}\left\{u_{s1R}^{*}\right\}-\left[c_{s11}^{*}\right]^{-1}\left[c_{s12}^{*}\right]\left\{p_{s2}^{*}\right\} \\ &= -\frac{\pi}{2\eta}\left\{p_{s11}^{*}\right\}+\frac{\pi B}{4\eta}\left\{p_{s13}^{*}\right\}-\left\{p_{s12}^{*}\right\}\end{aligned} \tag{3.2.76}$$

$$\begin{aligned}\left\{u_{s2}^{*}\right\} &= \frac{4b\Delta p}{\pi E^{'}\left|H\right|}\left[c_{s21}^{*}\right]\left\{p_{s1}^{*}\right\}+\frac{4b\Delta p}{\pi E^{'}\left|H\right|}\left[c_{s22}^{*}\right]\left\{p_{s2}^{*}\right\} \\ &= \frac{2\eta}{\pi}\left[c_{s21}^{*}\right]\left\{p_{s1}^{*}\right\}+\frac{2\eta}{\pi}\left[c_{s22}^{*}\right]\left\{p_{s2}^{*}\right\} \\ &= -\left\{u_{s21}^{*}\right\}+\frac{B}{2}\left\{u_{s24}^{*}\right\}-\frac{2\eta}{\pi}\left(\left\{u_{s22}^{*}\right\}-\left\{u_{s23}^{*}\right\}\right)\end{aligned} \tag{3.2.77}$$

Different from equations (3.2.21) and (3.2.22), the conservation of the non-dimensionalized liquid volume Ψ is now expressed as

$$\begin{aligned}\Psi &= -\pi B(1-m^{2})+\frac{\pi}{4}B^{2}(1-m^{4})-2\pi B\sum_{i=1}^{N}r_{s2i}^{*}\Delta r_{s2}^{*}u_{s2i}^{*} \\ &= -\pi(1-m^{2}-\lambda_{1}-\lambda_{2}\eta)B+\frac{\pi}{4}(1-m^{4}-\lambda_{6})B^{2}\end{aligned} \tag{3.2.78}$$

Therefore

$$B = \frac{-2X+2\sqrt{X^{2}+\dfrac{\Psi}{\pi}Y}}{Y} \tag{3.2.79}$$

with

$$X = -(1-m^{2}-\lambda_{1}-\lambda_{2}\eta) \tag{3.2.80}$$

$$Y = (1-m^{4}-\lambda_{6}) \tag{3.2.81}$$

And the dimensionless system free energy U_{T}^{*} is now given by

$$\begin{aligned}U_{T}^{*} &= -2\sqrt{\frac{\Gamma}{\Psi}}(1+\Phi m^{2})B+(\frac{\pi}{4}\lambda_{3}+\frac{1}{2}\lambda_{4}\eta-\frac{1}{\pi}\lambda_{5}\eta^{2})B^{1/2} \\ &\quad +(-\frac{\pi}{8}\lambda_{7}-\frac{1}{4}\lambda_{8}\eta)B^{3/2}+\frac{\pi}{16}\lambda_{9}B^{5/2}\end{aligned} \tag{3.2.82}$$

Based on equation (3.2.82), the equilibrium configuration for negative H can be found using the same method mentioned above. The results are shown in Figures 3.18-3.20.

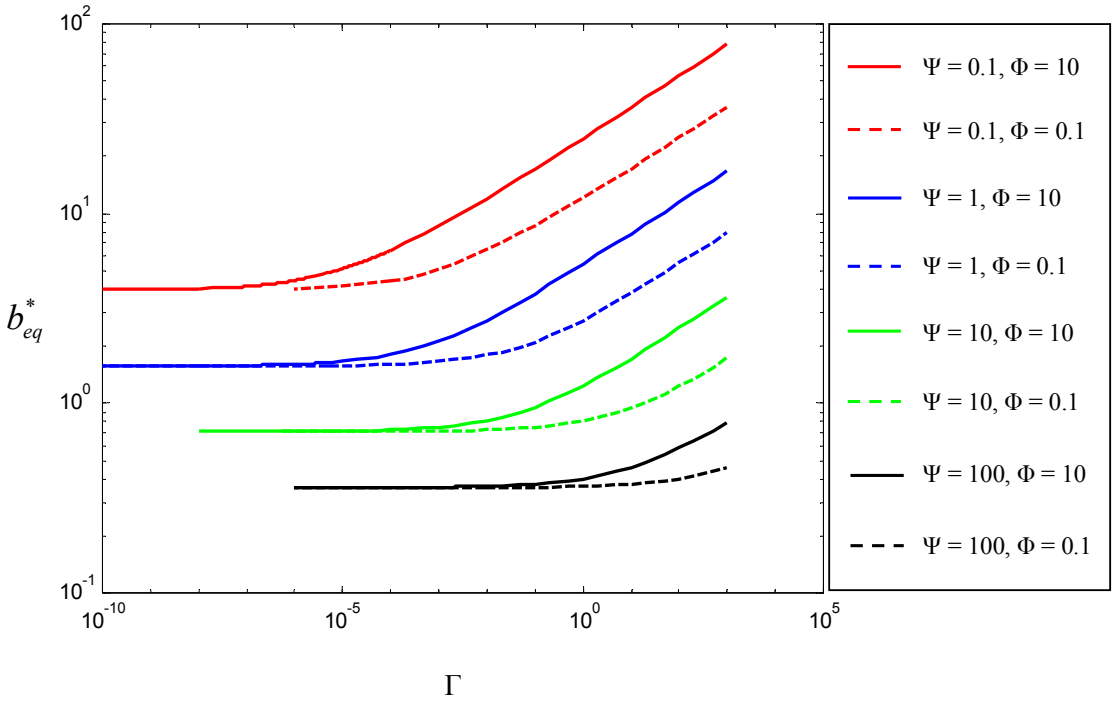

Figure 3.18 Variation of dimensionless equilibrium wetted radius, b^*_{eq}, with control variables Γ, Ψ and Φ for negative rigid surface separation, H.

Figure 3.18 shows the variation of the dimensionless wetted radius, b^*_{eq} with Γ for negative H. For large Γ and small Ψ, the dimensionless wetted radius, b^*_{eq} depends on all three control variables, Γ, Ψ and Φ. It increases with increasing Γ, decreasing Ψ and increasing Φ. But for small Γ and large Ψ, b^*_{eq} becomes independent of Φ and Γ and only depends on Ψ.

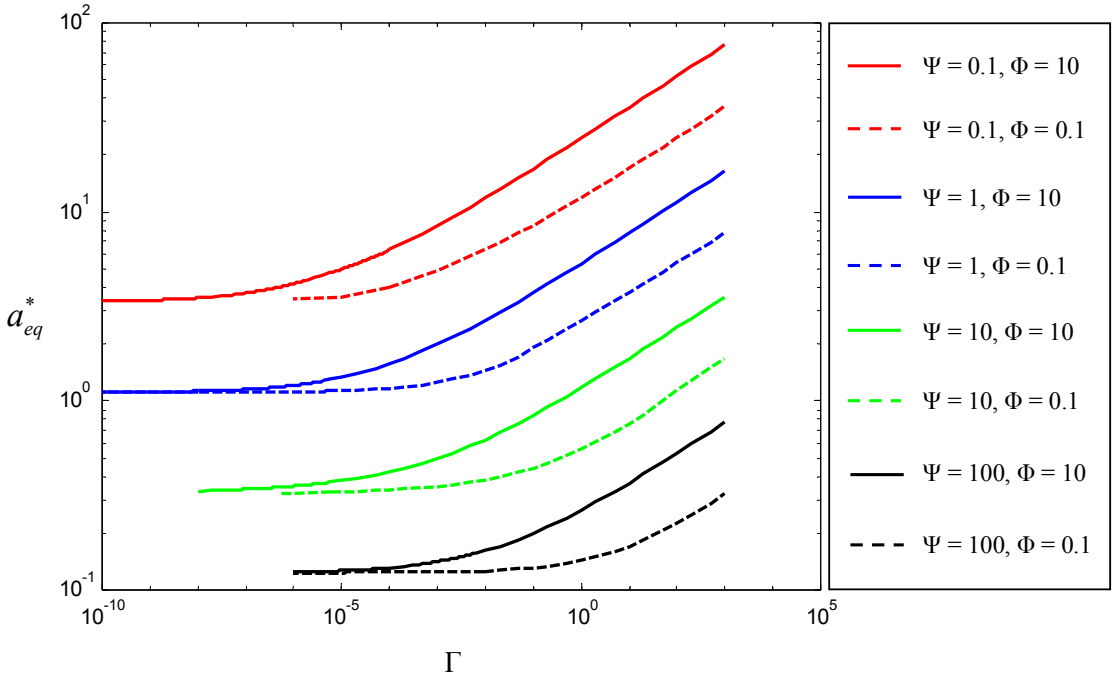

Figure 3.19 Variation of dimensionless equilibrium contact radius, a^*_{eq}, with control variables Γ, Ψ and Φ for negative rigid surface separation, H.

Figure 3.19 shows the variation of the dimensionless contact radius, a^*_{eq} with Γ for negative H. For given Ψ and Φ, a^*_{eq} still increases with increasing Γ. When Γ is large, the curve in the log-log plot is linear, just like what has been observed for positive H. But for small Γ, the situation is different from what has been observed for positive H. The curve levels out instead of curling down. As Γ decreases, the slope of the curve tends to zero. When Ψ increases, the dimensionless equilibrium contact radius a^*_{eq} decreases, and the level-out appears at a relative higher value of Γ. When Φ increases, a^*_{eq} increases, and the non-linearity appears at relative lower value of Γ.

For large Γ and small Ψ, the curves in the log-log plot of Figure 3.19 still can be fitted by

$$a_{eq}^{*} = 2.342(\Phi + 1)^{1/3}\,\Gamma^{1/6}\Psi^{-2/3} \tag{3.2.83}$$

i.e., the dimensional equilibrium contact radius, a_{eq}, converges to the dry contact radius at zero interference ($a_{eq} = \left(\frac{2\pi R^2 \Delta\gamma}{E'}\right)^{1/3}$) now from the negative side. This result reveals a continuity at $H = 0$. And the convergence can still be interpreted as a result of a negligible wetted area compared to a relatively large contact zone.

At the other end of the spectrum, for small Γ and large Ψ (i.e., small value of μ), the curves in the log-log plot of Figure 3.19 converge to

$$a_{eq}^{*} = \Psi^{-1/2} \tag{3.2.84}$$

which is independent of Φ. If we substitute for Ψ, the dimensional equilibrium contact radius, a_{eq}, is given by

$$a_{eq} = \sqrt{R|H|} \tag{3.2.85}$$

Equation (3.2.85) is the equilibrium contact radius predicted by Hertz contact model[24], with $|H|$ replacing the interference (δ) in the Hertz contact model. This convergence is easy to understand because, for small Γ and large Ψ, the capillary effect and the solid-solid interaction are weak and negligible when compared to the relative strong elastic effect.

As a summary, let us consider the situations for both positive *H* and negative *H*. When *H* decreases from positive to negative, we can see that Γ first increases from zero (where $H = +\infty$) to infinity (where $H = 0$), then goes back from infinity toward zero

(where H takes large negative value). For given Ψ and Φ, the equilibrium contact radius continuously transits from a pre-JKR radius, which is achieved before the JKR predication is reached at the interface and is smaller than the JKR radius, at small values of Γ (large positive *H*) to a JKR radius at $\Gamma = \infty$ ($H = 0$) and then to a Hertz radius at $\Gamma = 0$ (large negative *H*). Increasing Ψ or decreasing Φ shrinks the near-JKR region, i.e., makes the pre-JKR radius and the Hertz radius appears at relative higher value of Γ (corresponding to smaller $|H|$).

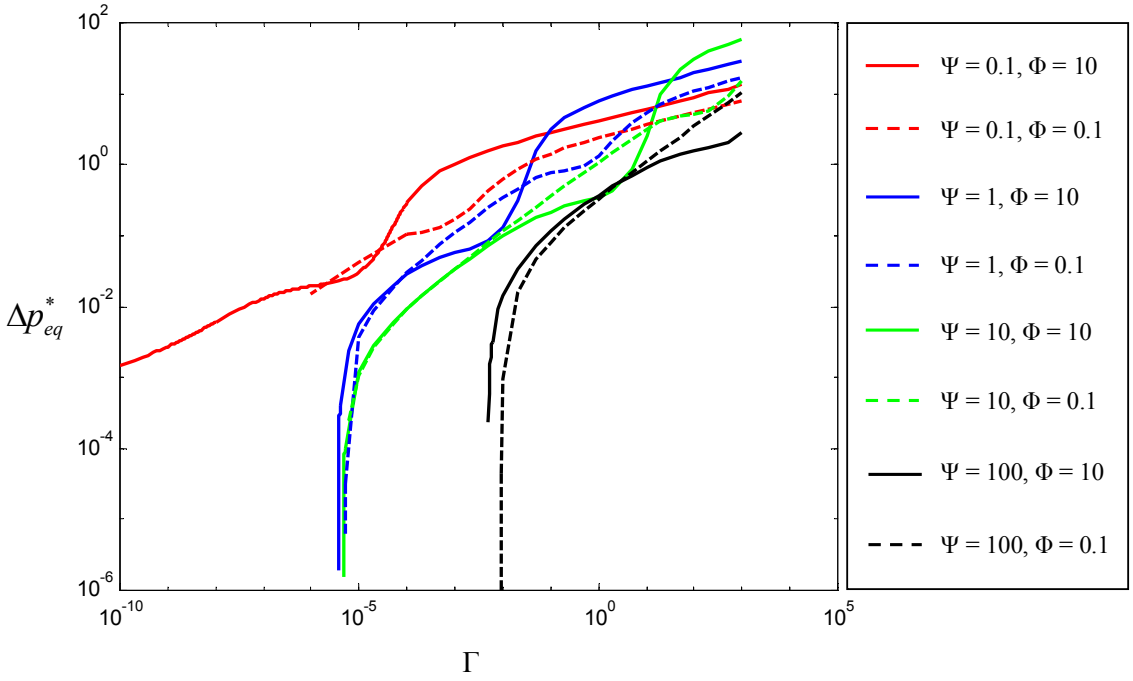

Figure 3.20 Variation of dimensionless equilibrium pressure drop, Δp^{*}_{eq}, with control variables Γ, Ψ and Φ for negative rigid surface separation, *H*.

The equilibrium contact profile can be shown by the dimensionless gap h_{eq}^{*}, which is given by

$$h_{eq}^{*} = \begin{cases} 0, & r^{*} \le m_{eq} \\ sign(H) + \dfrac{B_{eq}}{2} r^{*2} - u_{s2eq}^{*}, & m_{eq} < r^{*} \le 1 \end{cases} \tag{3.2.86}$$

and where u_{s2eq}^{*} is determined from equation (3.2.16) (for positive *H*) or equation (3.2.77) (for negative *H*) with all the equilibrium parameters. In Figures 3.21-3.22, the profiles show the same transition from a pre-JKR profile at small values of Γ (large positive *H*), which has a slimmer but more stretched neck, to a JKR profile at $\Gamma = \infty$ ($H = 0$) and then to a Hertzian one at $\Gamma = 0$ (large negative *H*). A similar result has been obtained by Maugis and Gauthier-Manuel[43] for a sphere in contact with an elastic plane in the presence of a liquid meniscus. They gave an analytical analysis using a Dugdale model and demonstrated that there is a continuous transition from a JKR profile to a Hertzian profile as a parameter λ defined as

$$\lambda = \frac{2\sigma_o}{(\pi w K^2 / R)^{1/3}} \tag{3.2.87}$$

decreases from infinity to zero, where σ_o is equal to the Laplace pressure drop, Δp, and w is equal to $2\gamma_{LV}$, and $K = 4/3\, E'$. Thus, Maugis and Gauthier-Manuel pointed out that the contact profile changes from JKR profile to Hertzian profile when the size of the meniscus increases, which is reflected as decreasing σ_o. The result was also confirmed by some experimental observation on contact of crossed mica cylinders[38-40].

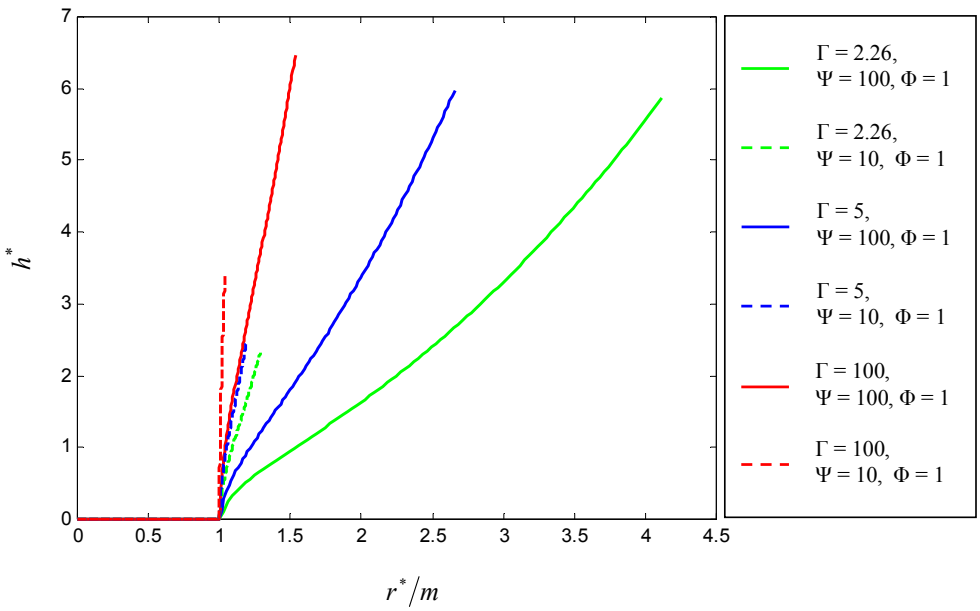

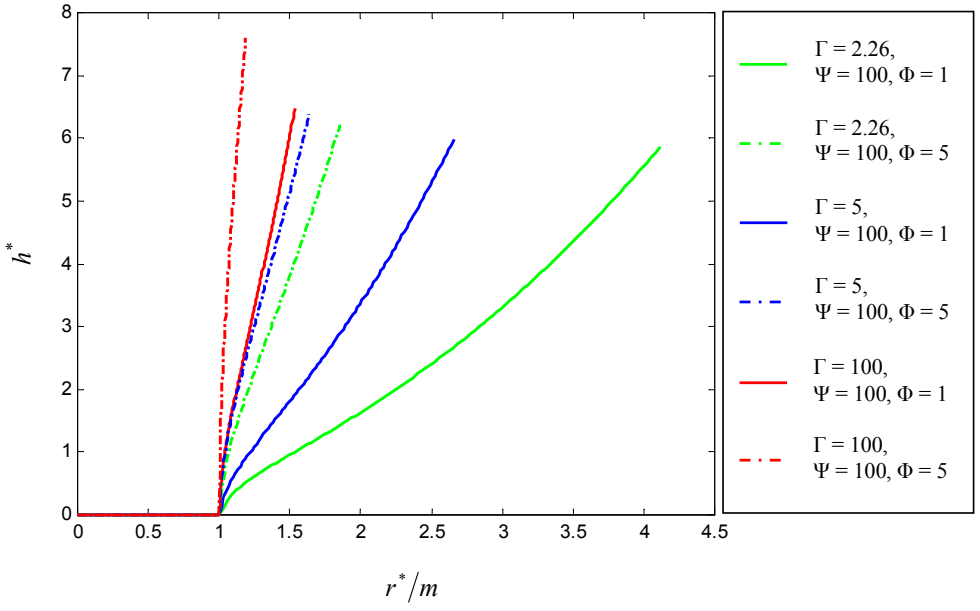

Figure 3.21 The transition of contact profiles for positive *H*.

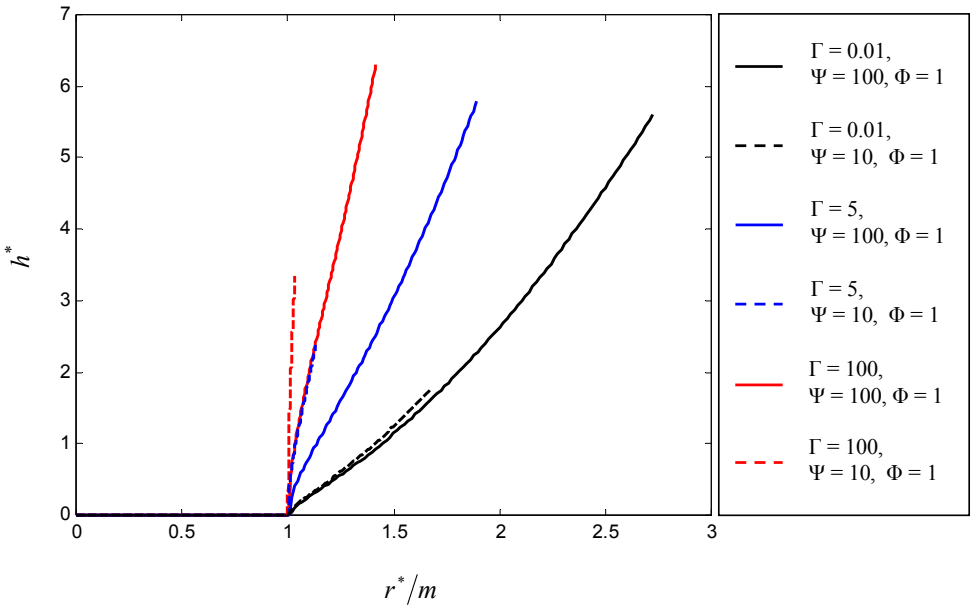

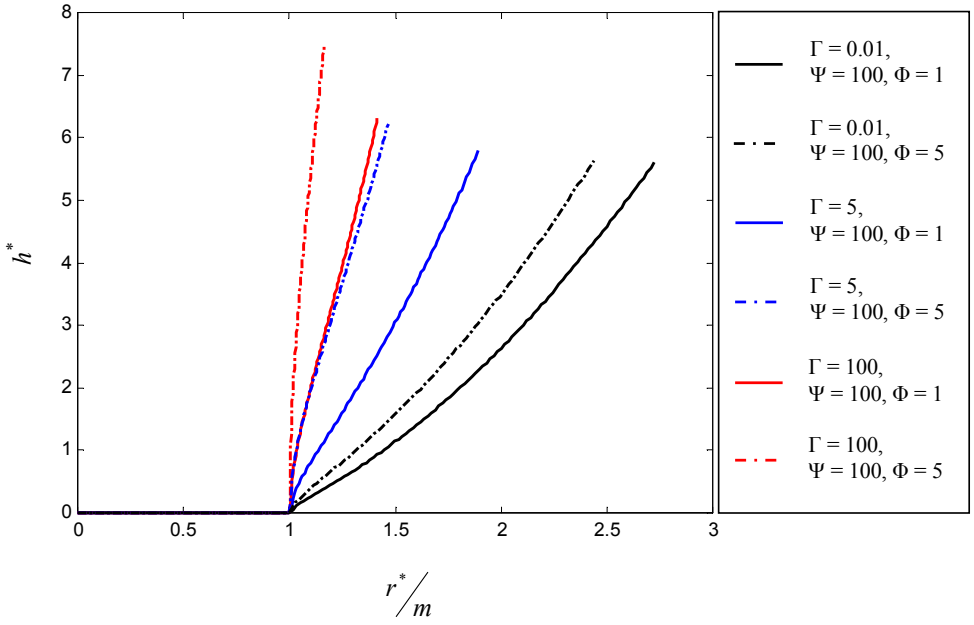

Figure 3.22 The transition of contact profiles for negative *H*.

3.3 Jump-on Condition

The results in section 3.1 revealed a kind of instability at the interface, that is, under certain condition, surfaces jump into contact (jump-on). It was found that when $\Gamma \geq \Gamma_c(\Psi) = 0.03007\Psi^{1.3955} + 0.01336$, the interface is unstable with any non-contact configuration and must come into solid-solid contact. And when $\Psi < 0.6143$, the surfaces jump into contact from a finite separation; when $\Psi \geq 0.6143$, the surfaces gradually come into point contact. The stability of the point contact configuration is not determined in section 3.1 because of the lack of information on the variation of energy beyond $\eta_{eq} = 1$. This stability problem can now be solved with the results from section 3.2.

In Figure 3.16, asterisks mark out the points where the surfaces first come into contact (at $\Gamma = \Gamma_c$). Equilibrium configurations for lower values of Γ can only be achieved during the detachment process, in which the surfaces are pulled apart. In the figure, the dimensionless equilibrium contact radii a_{eq}^* at these points are non-zero, but the values decrease when Ψ increases for given Φ. One may wonder what occurs if Ψ keeps increasing. Will the value of a_{eq}^* at $\Gamma = \Gamma_c$ finally become zero? Calculation shows that for given Φ, when Ψ reaches certain value, a_{eq}^* at $\Gamma = \Gamma_c$ does become zero, which indicates a stable point contact configuration. Figure 3.23 shows this critical value of Ψ at different Φ. The curve can be fitted by $\Psi_c(\Phi) = 33.25 + 1083.40\Phi + 9938.64\Phi^2$ with an error less than 5%, where Ψ_c denoted the critical values. When $\Psi < \Psi_c(\Phi)$, point contact is unstable at $\Gamma = \Gamma_c$. Once solid-solid contact is initiated, it spontaneously grows to

finite area, i.e., the surfaces jump into a finite area contact. When $\Psi \geq \Psi_c(\Phi)$, the interface achieves a stable point contact configuration at $\Gamma = \Gamma_c$. Therefore, the change of interface configuration from non-contact to contact is a smooth process.

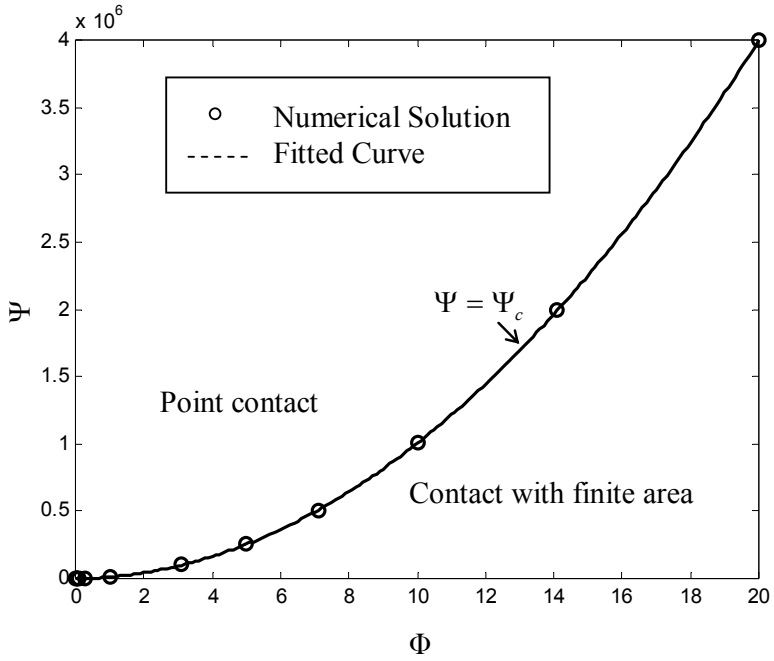

Figure 3.23 Critical values of Ψ, which determine the manner of the interface getting into contact. When $\Psi < \Psi_c$, the interface jumps into finite area contact. When $\Psi \geq \Psi_c$, the interface gradually goes through point contact.

In summary, the jump-on condition can be expressed as the following: When $\Gamma \geq 0.03007\Psi^{1.3955} + 0.01336$ and $\Psi < 33.25 + 1083.40\Phi + 9938.64\Phi^2$, the interface jumps-on. And if $\Psi < 0.6143$, the surfaces jump from finite separation into finite area contact. If $\Psi \geq 0.6143$, the surfaces jump from point contact to finite area contact.

3.4 Jump-off Condition

The solution space of the equation set (3.2.44) and (3.2.45) shows that for given Ψ and Φ, when Γ is reduced to a certain value, the solution branch folds back, and there is no solution for the equation set for Γ less than that value (Figure 3.14). At the turning point, the tangent to the curve becomes vertical, which implies that a jump is going to occur at that point[32]. It is also shown in Figure 3.16 that the curve of dimensionless equilibrium contact radius a_{eq}^* vs Γ has a slope of infinity at the critical value and the corresponding value of a_{eq}^* at the point is finite, which indicate that the surface is going to jump out of contact (jump-off). We denote this critical value as Γ_s, i.e., Γ at separation.

It can be seen from Figure 3.14 and Figure 3.16 that Γ_s depends on Ψ and Φ. When Ψ increases or Φ decreases, the value of Γ_s increases. To quantify the relation between Γ_s and Ψ and Φ, one needs to determine the value of Γ_s at various combinations of Ψ and Φ. However, finding Γ_s by tracking the turning point on the solution space curve is laborious. In order to obtain the value of Γ_s more efficiently, the corresponding dimensionless free energy U_T^* was checked at the turning points in Figure 3.14. It was found that, at the turning points, there is always a saddle point on the energy surface, and the energy curve at the saddle point inflects in the *m*-direction with a global minimum appearing at $m = 0$ (Figure 3.24). This feature causes the surfaces jump out of contact. Since an inflection point on an energy curve in *m*-direction can be determined by

$$\frac{\partial^2 U_T^*}{\partial m^2} = 0 \tag{3.3.1}$$

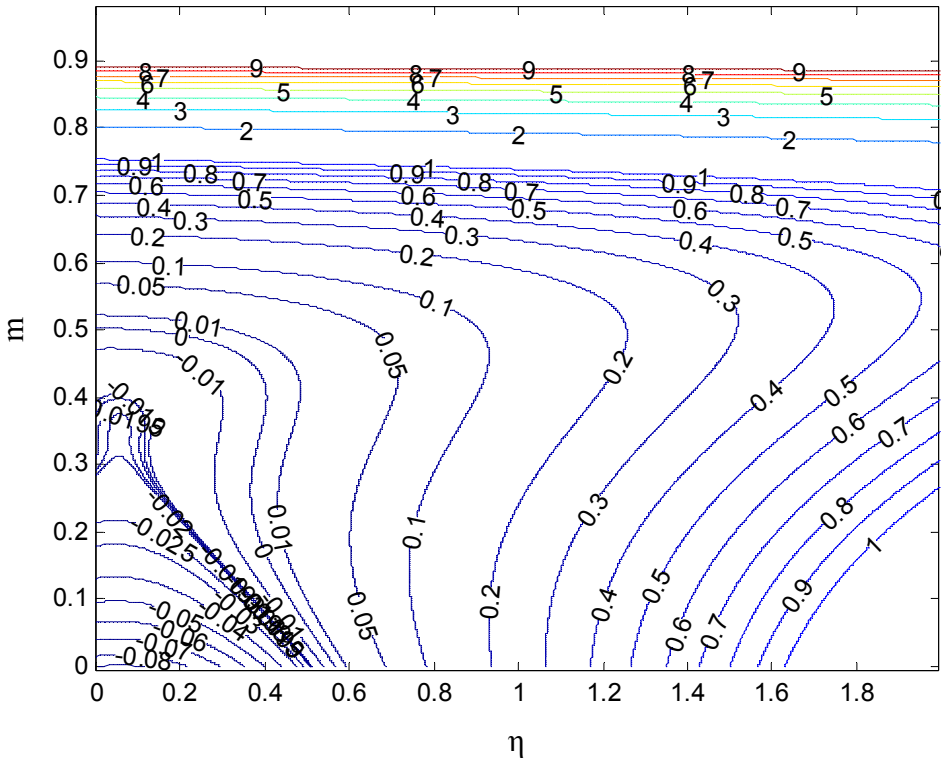

Figure 3.24 Typical contour of the dimensionless free energy U_T^* at the turning points in the solution space of equation set (3.2.44) and (3.2.45).

a turning point on a solution branch of given Ψ and Φ can be located efficiently by solving equations (3.2.44), (3.2.45) and (3.3.1) simultaneously for Γ, η and m. The solution yields the value of Γ_s for the given set of Ψ and Φ and the corresponding equilibrium configuration (unstable). The Newton-Raphson method is used to solve the equation set. Because the solution of the non-linear equation set is not unique, it is important to start from a correct point and maintain continuity of the solution. Some starting points can be obtained from Figure 3.14 and it turns out that a zeroth-order continuation is sufficient.

Figure 3.25 shows the variation of Γ_s with Ψ, where several curves are given for various Φ. For a given Φ, the curve can be roughly fitted by $\Gamma_s = c_1\Psi^{2.4} + c_2\Psi$, where the

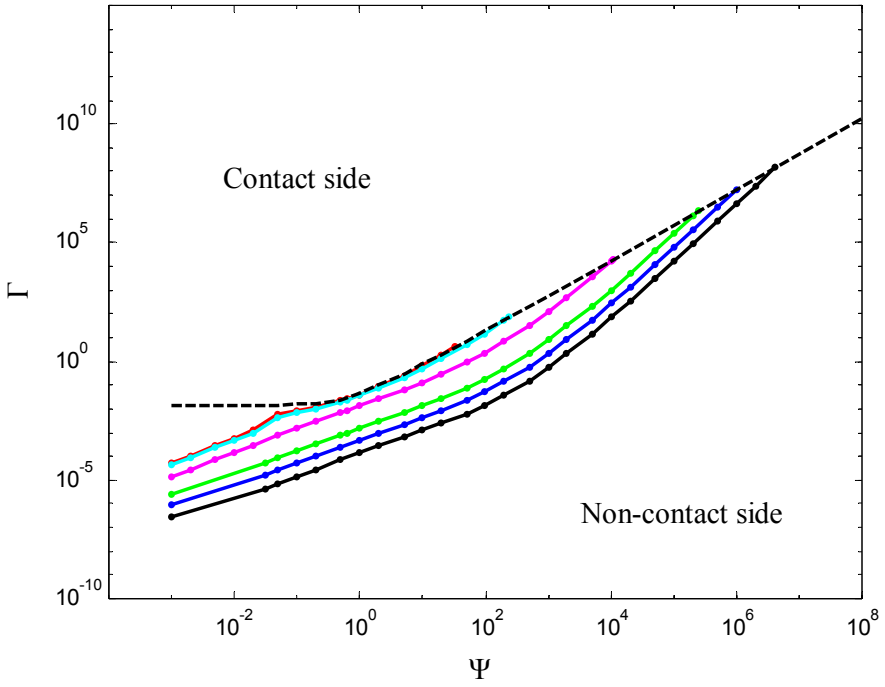

Figure 3.25 Critical values of Γ, at which the surfaces jumps apart. Red color is for $\Phi = 0$. Cyan color is for $\Phi = 0.1$. Magenta color is for $\Phi = 1$. Green color is for $\Phi = 5$. Blue color is for $\Phi = 10$. Black color is for $\Phi = 20$. Dashed line is the jump-on condition as a reference.

numerical values of c_1 and c_2 are listed in Table 3.1 for different Φ. It can be seen that both c_1 and c_2 depend on the value of Φ. Thus, more generally, one can write $\Gamma_s = c_1(\Phi)\Psi^{2.4} + c_2(\Phi)\Psi$. The precise determination of the form of the functions $c_1(\Phi)$ and $c_2(\Phi)$ as well as a comprehensive assessment of their accuracy, which requires

extensive calculations, is reserved for a later investigation. When $\Gamma > \Gamma_s$, the interface can achieve some stable equilibrium contact configuration. When $\Gamma \le \Gamma_s$, the interface becomes unstable with any contact configuration and must depart from solid-solid contact.

Table 3.1 The numerical values of coefficients c_1 and c_2 in the jump-off condition (obtained by curve fitting).

Φ	c_1	c_2
20	0.08	0.001667
10	0.18	0.002
5	0.6	0.002222
1	4.0	0.003571
0.1	2.5	0.02
0	1.0	0.05

From Figure 3.25, we can also see that all curves end at the jump-on boundary $\Gamma = \Gamma_c = 0.03007\Psi^{1.3955} + 0.01336$ (dashed line in the figure), and the intersection coincides with $\Psi = \Psi_c = 33.25 + 1083.40\Phi + 9938.64\Phi^2$. When $\Psi < \Psi_c$, at $\Gamma = \Gamma_s$, the surfaces jump out off contact from finite area contact. The value of Γ_s is always lower than the corresponding Γ_c, which indicates a hysteresis and hence energy consumption in the approach and detachment process. As Ψ increases or Φ decreases, the difference between Γ_s and Γ_c decreases. When $\Psi \ge \Psi_c$, $\Gamma_s = \Gamma_c$; the surfaces smoothly come into and get out of contact through point contact at the same value of Γ.

Therefore, the jump-off condition can be summarized as follows: When $\Gamma \le \Gamma_s$ and $\Psi < \Psi_c$, the interface jumps off from finite area contact.

3.5 Conclusions

The interaction between two elastic spheres coupled via a small liquid bridge was investigated and the mechanical stability of the interface was examined. Stable equilibrium configurations were determined. From the analysis, the following conclusions can be drawn:

1) The non-dimensionalized system before contact has two degrees of freedom with Γ and Ψ as the control variables, where $\Gamma = \dfrac{\gamma_{LV}{}^2\left(\dfrac{\cos\theta_1+\cos\theta_2}{2}\right)^2 V_o}{E'^2 H^5}$, $\Psi = \dfrac{V_o}{RH^2}$.

2) The non-dimensionalized system after contact has three degrees of freedom with Γ, Ψ and Φ as the control variables, where $\Phi = \dfrac{\Delta\gamma}{\gamma_{LV}(\cos\theta_1+\cos\theta_2)} - 1$.

3) When $\Gamma < 0.03007\Psi^{1.3955} + 0.01336$, the interface can achieve some stable equilibrium configuration without solid-solid contact.

4) When $\Gamma \ge 0.03007\Psi^{1.3955} + 0.01336$ and $\Psi < 33.25 + 1083.40\Phi + 9938.64\Phi^2$, the interface jumps into contact. Additionally if $\Psi < 0.6143$, the surfaces jump from finite separation into finite area contact. If $\Psi \ge 0.6143$, the surfaces jump from point contact to finite area contact.

5) When $\Gamma \ge 0.03007\Psi^{1.3955} + 0.01336$ and $\Psi \ge 33.25 + 1083.40\Phi + 9938.64\Phi^2$, the interface comes into and gets out of contact smoothly through point contact configuration.

6) In the case of solid-solid contact, for given Ψ and Φ, the equilibrium contact radius continuously transits from a pre-JKR radius at small values of Γ (large positive *H*) to a JKR radius at $\Gamma = \infty$ ($H = 0$) and then to a Hertz radius at $\Gamma = 0$ (large negative *H*). Increasing Ψ or decreasing Φ shrinks the near-JKR region, i.e., makes the pre-JKR radius and the Hertz radius appears at relative higher value of Γ (corresponding to smaller $|H|$). A similar transition exists in the contact profile.

7) When $\Gamma > c_1(\Phi)\Psi^{2.4} + c_2(\Phi)\Psi$, the interface can achieve some stable equilibrium configuration with solid-solid contact.

8) When $\Gamma \le c_1(\Phi)\Psi^{2.4} + c_2(\Phi)\Psi$ and $\Psi < 33.25 + 1083.40\Phi + 9938.64\Phi^2$, the interface jumps-off from finite area contact.

9) When $\Psi \ge 33.25 + 1083.40\Phi + 9938.64\Phi^2$, the interface smoothly gets out of contact via point contact configuration at $\Gamma = 0.03007\Psi^{1.3955} + 0.01336$.

CHAPTER IV

SURFACE APPROACH AND DETACHMENT OF TWO ELASTIC SPHERES IN PRESENCE OF A LIQUID BRIDGE

4.1 Paths of Surface Approach and Detachment

The analysis in Chapter III is for static systems. However, the results can be used to study the approach and detachment of two elastic spheres in presence of a small liquid bridge when the process is slow enough to allow a quasi-static assumption. Consider the same system as shown in Figures 3.1 and 3.8. From the analysis in Chapter III, one can see that, in a Γ-Ψ plane, whenever the system condition moves toward the jump-on boundary from the non-contact side (Figure 3.14), the surfaces of two spheres approach and finally will jump into finite contact when the jump-on condition is reached; whenever the system condition moves toward the jump-off boundary from the contact side (Figure 3.14), the surfaces of two spheres retract and finally will jump out of contact when the jump-off condition is reached. Theoretically, there are infinite ways to induce jump-on and jump-off at the interface. One can arbitrarily vary one or more of the physical parameters in the definitions of Γ and Ψ to bring the system to the critical conditions. But practically, among the parameters, only the rigid surface separation H and the applied liquid volume V_o can be changed continuously, so the surface approach and detachment are usually achieved by continuously varying H or V_o. The paths of surface approach and detachment can be shown in a Γ-Ψ plane.

Because

$$\Gamma = \frac{\gamma_{LV}{}^2 \left(\frac{\cos\theta_1 + \cos\theta_2}{2} \right)^2 V_o}{E'^2 H^5} \tag{4.1.1}$$

$$\Psi = \frac{V_o}{RH^2} \tag{4.1.2}$$

when R, E', γ_{LV}, θ, $\Delta\gamma$, V_o are fixed and only H is varying, the paths of surface approach and detachment are lines with a slope of 5/2 in a log-log plot of Γ vs. Ψ and the intercepts of the lines at the Y-axis are determined by a dimensionless factor

$$\chi = \frac{\Gamma}{\Psi^{5/2}} = \frac{\gamma_{LV}^2 \left(\frac{\cos\theta_1 + \cos\theta_2}{2} \right)^2 R^{5/2}}{E'^2 V_o^{3/2}} \tag{4.1.3}$$

With a certain value of χ, as H is varying, the system condition shifts along a specific line. To locate a point for a prescribed value of H on the specific line, a dimensionless minimum rigid surface separation H^* is defined as

$$H^* = H\sqrt{\frac{R}{V_o}} = \sqrt{\frac{1}{\Psi}} \tag{4.1.4}$$

For such a system, with R, E', γ_{LV}, θ, $\Delta\gamma$, V_o and H at each step assumed to be known, one can compute the values of χ and H^* and follow the steps of surface approach and detachment easily on the log-log plot of Γ vs. Ψ.

On the other hand, if a system has the values of R, E', γ_{LV}, θ, $\Delta\gamma$, H, fixed with V_o as the only variable, the paths of surface approach and detachment are lines with a slope of 1 in a log-log plot of Γ vs. Ψ and the intercepts of the lines at Y-axis are determined by a dimensionless factor μ, which is given by

$$\mu^3 = \frac{\Gamma}{\Psi} = \frac{\gamma_{LV}^2 \left(\frac{\cos\theta_1 + \cos\theta_2}{2} \right)^2 R}{E'^2 H^3} \tag{4.1.5}$$

A certain value of μ corresponds to a specific line, and to locate a point for a prescribed value of V_o on the line, we need to know the dimensionless liquid volume, V_o^*, which is defined as

$$V_o^* = \frac{V_o}{RH^2} = \Psi \tag{4.1.6}$$

Figure 4.1 shows these paths along with the jump-on and jump-off boundaries. In the

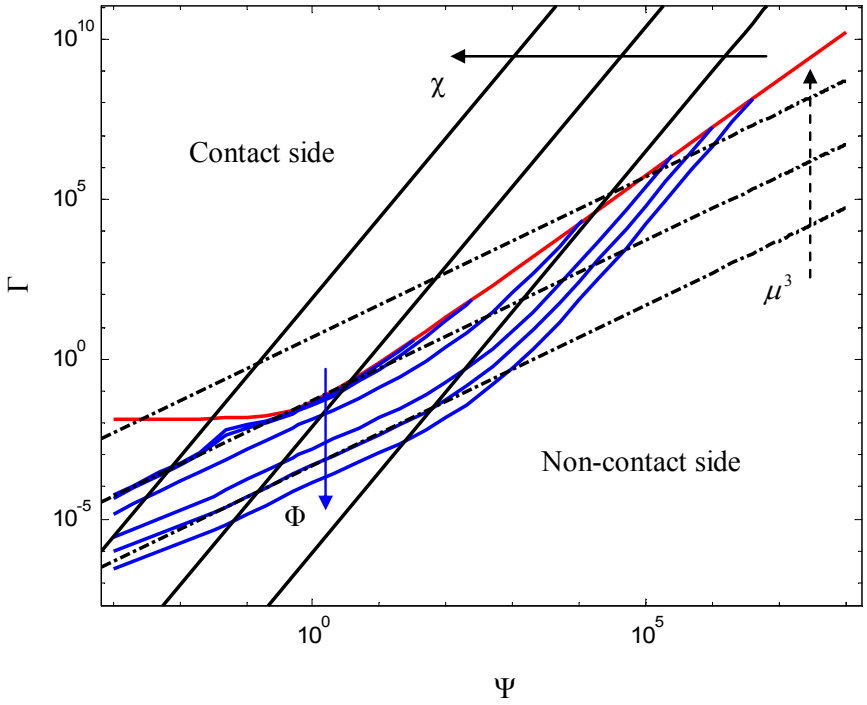

Figure 4.1 Paths of surface approaching and detachment. The red curve is the jump-on boundary. The blue curves are the jump-off boundaries for different Φ, from top to bottom $\Phi = 0, 0.1, 1, 5, 10, 20$. The solid lines are paths by changing H. From right to left, $\chi = 10^{-6}, 10^{-2}, 100$. The dash-dotted lines are paths by changing V_o. From right to left, $\mu^3 = 5\times10^{-4}, 5\times10^{-2}, 5$.

figure, the red line is the jump-on boundary and the blue lines are jump-off boundaries for different Φ. The solid black lines correspond to the paths for the cases where only H is controlled. The dash-dotted black lines correspond to the paths for the cases where only V_o is controlled. When R, E', γ_{LV}, θ, $\Delta\gamma$, V_o are fixed and only H is varying, the system condition moves along one of the solid black lines according to the values of χ and H^*. When H^* is very large, the interface achieves a non-contact equilibrium configuration. As H^* decreases, the system condition moves upward along the line specified by the value of χ. When it reaches the jump-on boundary, the interface comes into contact. If H^* decreases further, the contact region grows. If H^* increases, the contact region shrinks and the system condition moves back along the line. When it reaches the corresponding jump-off boundary (depends on the value of Φ), the surfaces separate. Similarly, when R, E', γ_{LV}, θ, $\Delta\gamma$, H are fixed and only V_o is varying, the system condition moves along one of the dash-dotted black lines according to the values of μ and V_o^*. Whenever the jump-on boundary is reached from the non-contact side, the interface comes into contact, and whenever the jump-off boundary is reached from the contact side, the interface gets out of contact.

4.2 Critical Values of Changing Variables at Jump-on and Jump-off

From Figure 4.1, one can clearly see the paths passing through the boundaries. The intersections of the path and the boundaries define the critical values of H^* or V_o^* at jump-on and jump-off for certain χ or μ[3]. These critical values can be easily extracted

from Figure 4.1. For convenience in analyzing certain effects, another non-dimensional system is adopted, which is similar to that commonly used in the studies of contact. A new dimensionless minimum rigid surface separation $H^{'}$ as

$$H^{'} = \frac{H}{\left(\frac{R\gamma_{LV}^{2}\left(\frac{\cos\theta_1 + \cos\theta_2}{2} \right)^{2}}{E^{'2}} \right)^{1/3}} = \left(\frac{\Psi}{\Gamma} \right)^{1/3} = \left(\frac{1}{\Gamma H^{*2}} \right)^{1/3} \tag{4.2.1}$$

and a new dimensionless liquid volume, $V_o^{'}$, as

$$V_o^{'} = \frac{V_o}{\left(\frac{R^5\gamma_{LV}^{4}\left(\frac{\cos\theta_1 + \cos\theta_2}{2} \right)^{4}}{E^{'4}} \right)^{1/3}} = \left(\frac{\Psi^5}{\Gamma^2} \right)^{1/3} = \left(\frac{V_o^{*5}}{\Gamma^2} \right)^{1/3} \tag{4.2.2}$$

The variations of critical $H^{'}$ with χ, and the variations of critical $V_o^{'}$ with μ^3 are shown in Figure 4.2 and Figure 4.3, respectively.

It can be seen that, for the cases where H is varying, the situation is relatively simple. For certain Φ, there is one critical $H^{'}$ at jump-on and one critical $H^{'}$ at jump-off for any given value of χ which satisfies $\chi > 1.84\times10^{-6}\left(\Phi + 0.054\right)^{-2}$. The critical $H^{'}$ at jump-on is always smaller than the critical $H^{'}$ at jump-off. For these combinations of Φ and χ, the interface will jump into and out of contact with a finite area, and once the jump-on occurs, in order to separate the surfaces, one has to pull them further away from the jump-on *H*, meaning there is a hysteresis or energy dissipation in this process. When $\chi \le 1.84\times10^{-6}\left(\Phi + 0.054\right)^{-2}$, the jump-on and the jump-off curves merge in Figure 4.2.

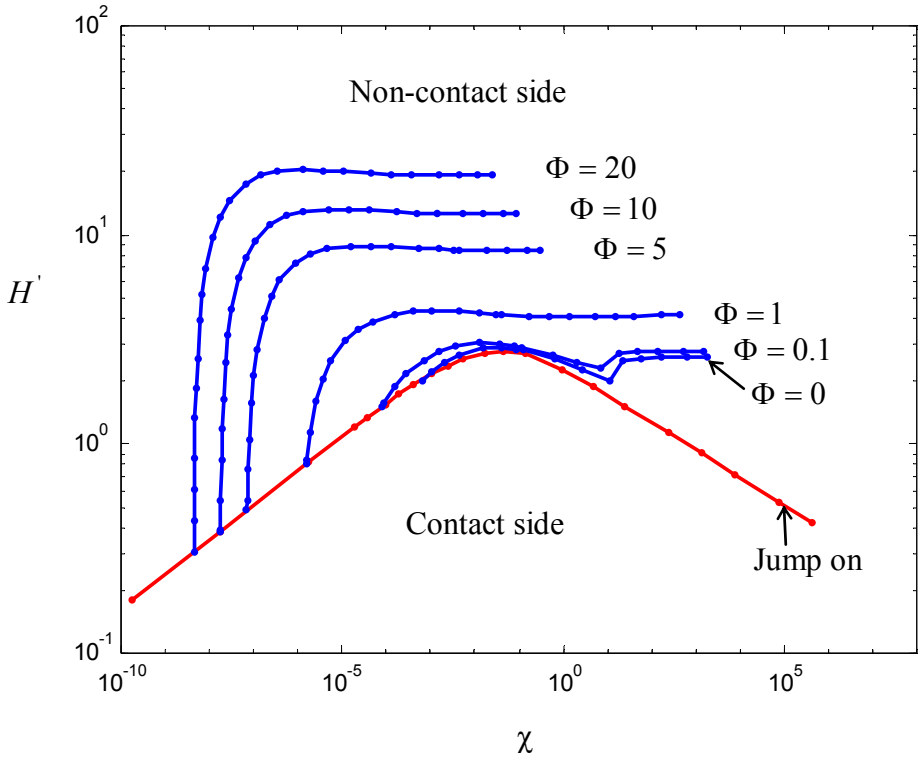

Figure 4.2 The critical values of H' at jump-on and jump-off as a function of χ. The red curve is the jump-on condition. The blue curves are the jump-off conditions for different Φ, from top to bottom, $\Phi = 20, 10, 5, 1, 0.1, 0$.

The above equation can be derived from equations $\Gamma_c(\Psi) = 0.03007\Psi^{1.3955} + 0.01336$ and $\Psi_c(\Phi) = 33.25 + 1083.40\Phi + 9938.64\Phi^2$ (see section 3.3), but was obtained by direct curve fitting with an error less than 4%. For any given value of χ in this region, there will be no jump at the interface. The surfaces get into and out of contact smoothly through a point contact configuration. No hysteresis appears. The critical values of H' shown at these values of χ correspond to the moment when an equilibrium point contact configuration is assumed at the interface. The above results are supported by some

experimental observations. Both Christenson[40] and Maugis[43] have reported that for small liquid annuli the jump apart occurs with the surfaces still flattened, but for large menisci the separation of the two solids occurs after a point contact.

Looking at the jump-on curve (red curve in Figure 4.2), we can see that the curve tops at $\chi = 0.04577$ and $H^{'} = 2.7956$ (corresponds to $H^{*} = \sqrt{\frac{1}{\Psi}} = 1.0000$). When χ is larger or smaller, the critical value of $H^{'}$ at jump-on decreases. Therefore, the interface with $\chi = 0.04577$ is the most susceptible to the jump-on instability. In Figure 4.2, the linear part of the jump-on curve at large χ can be fitted by $H' = 2.273\chi^{-0.132}$ with relative error less than 3%. Therefore, when $\chi \to \infty$, $H^{'} \to 0$. If we take $\chi \to \infty$ as the result of $V_o \to 0$, this means that in dry contact the two surfaces jump into contact at zero interference ($H = 0$). The prediction agrees with the JKR model[23,24].

The jump-off condition is shown as the blue curves in Figure 4.2. Each of these curves is associated with a different value of Φ. For any given Φ, first the critical value of $H^{'}$ at jump-off increases quickly for small values of χ which are just above the value of $1.84\times10^{-6}\left(\Phi + 0.054\right)^{-2}$. Soon the curve reaches a peak and then drops a little and plateaus afterward for relative large χ. When Φ increases, the curve shifts up and the peak moves toward lower χ. The jump-off values of $H^{'}$ at large values of χ (the plateau height) can be fitted by $H^{'} = 2.621\left(\Phi + 1\right)^{2/3}$ with an error less than 3%. If we substitute for $H^{'}$, the jump-off values of H at large values of χ is given by $H = 1.651\left(\frac{R\Delta\gamma^{2}}{E^{'2}}\right)^{1/3}$. The equation can be taken as an estimation of the jump-off

separation for dry contact. It is close (within 3% relative error) to the JKR prediction of dry-contact jump-off displacement for fixed-grips device[24], which gives $\delta = -H = -\frac{3\pi^{2/3}}{4}\left(\frac{R\Delta\gamma^2}{E'^2}\right)^{1/3}$.

For the cases where V_o is varying, the situation is complicated. First, from Figure 4.3, it can be seen that, as revealed by the studies on fly/stiction phenomenon[15,16], changing V_o surely can cause instability at some interfaces. Given Φ, for any given value of μ^3 in

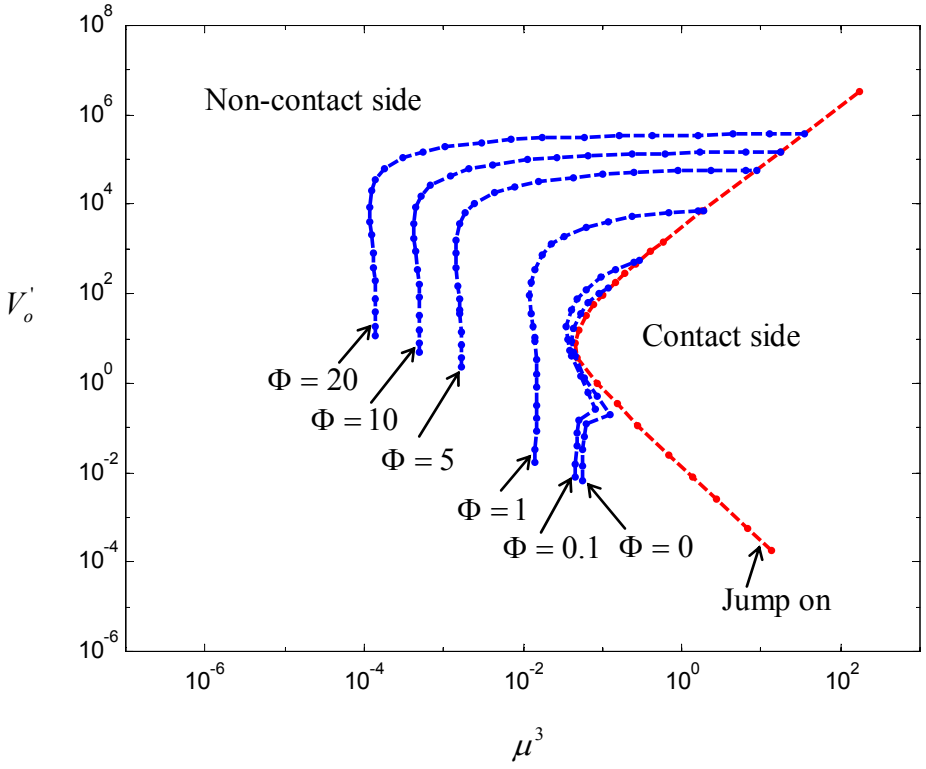

Figure 4.3 The critical values of V_o' at jump-on and jump-off as a function of μ^3. The red curve is the jump-on condition. The blue curves are the jump-off conditions for different Φ, from left to right, $\Phi = 20, 10, 5, 1, 0.1, 0$.

the range of $0.04577 \le \mu^3 < 1.872(\Phi + 0.0577)^{0.98}$, there are two critical values of $V_o^{'}$ for jump-on and one critical value of $V_o^{'}$ for jump-off. For moderate liquid volume V_o which makes $V_o^{'}$ in between the two jump-on values, the interface is unstable with any non-contact configuration and hence must collapse into intimate contact. For smaller or larger V_o which is out of the region between the two jump-on values, the interface will not collapse if it was initially out of contact. In this range of μ^3, the jump-off value of $V_o^{'}$ is larger than both of the two jump-on values of $V_o^{'}$. So, even though the interface may be caused to collapse by increasing or decreasing the liquid volume V_o, depending on the initial liquid volume in the interface is small or large, there is only one way to separate the contacted surfaces by increasing the liquid volume V_o until it reaches the jump-off value of $V_o^{'}$.

When $\mu^3 \ge 1.872(\Phi + 0.0577)^{0.98}$, the jump-off curve merges with the higher branch of the jump-on curve. Again, the equation is obtained from direct curve fitting with an error less than 6%. For any values of these μ^3, if the initial liquid volume V_o in a non-contact interface is very small, the interface is still going to jump into contact when V_o increases and reaches the lower jump-on value of $V_o^{'}$. However, the critical $V_o^{'}$ shown on the high branch is now corresponding to the one at which the interface going through an equilibrium point contact configuration. Therefore, if the initial liquid volume V_o in a non-contact interface is very large, when V_o decreases and reaches this value of $V_o^{'}$, the interface will smoothly come into contact through an equilibrium point-contact configuration and no jump is going to happen. Once the interface is in solid-solid contact, no matter how it gets there, through a jump or a smooth transition, there will not be a

jump-off behavior. When the liquid volume V_o is increased in order to separate the surfaces from contact, the interface configuration will gradually evolve and reach a point-contact equilibrium at the high branch critical value of $V_o^{'}$ and then separate.

For small values of μ^3 which satisfy $\mu^3 < 0.04577$, there is no jump-on value of $V_o^{'}$. This means that if the interface is initially non-contacted, it will remain non-contacted and never collapse no matter how the liquid volume V_o in the interface changes. For μ^3 in the range of $0.04577(\Phi+1)^{-2} < \mu^3 < 0.04577$, there is at least one jump-off value of $V_o^{'}$. This means that if the interface is initially in contact, it will jump out off contact at these values of $V_o^{'}$. The situation can be achieved if the presence of liquid in the interface occurs following the presence of solid contact, such as with liquid condensation around the contact zone. Even though our analysis assumed a pre-existing liquid bridge, in the calculations it was found that there is only one equilibrium contact configuration for a given condition specified by a set of μ^3 and $V_o^{'}$. Once μ^3 and $V_o^{'}$ are given, the equilibrium contact configuration is set. The interface is indifferent as to when the liquid is introduced. So, the analysis is applicable to these situations with later-introduced liquid in the interface. When $\mu^3 < 0.04577(\Phi+1)^{-2}$, there is no critical value of $V_o^{'}$ associated with any kind of contact/non-contact transition. The interface is always free of contact. It is impossible to achieve an equilibrium contact configuration for these values of μ^3.

Figures 4.2 and 4.3 provide some valuable information for understanding and preventing fly/stiction failure in hard disk interface. According to Gui and Marchon[15], the fly/stiction phenomenon is related to the collapse of the head-disc interface, triggered by the excessive accumulation of the liquids in the interface. Unlike the normal stiction

values, fly/stiction values exhibit a unique bi-modal distribution (Figure 4.4). In Figure 4.3, one can clearly see the collapse of the interface at some values of μ^3, caused by varying liquid volume in the interface. Since the liquid transfer at the head-disc interface is a random process and occurs in both directions, jump-on may randomly occur at the high jump-on $V_o^{'}$ or the low jump-on $V_o^{'}$. After jump-on, i.e., the collapse of the interface, if we start to pull off the head, the interface then goes through a process with fixed liquid volume and changing H. Because the interface may have a high volume or a low volume of liquid after jump-on, it may precede on a path with a small value of χ or a relatively large value of χ. In the next section, it will be shown that different paths lead to different pull-off forces. And this may be the reason for the bi-modal distribution of the fly/stiction

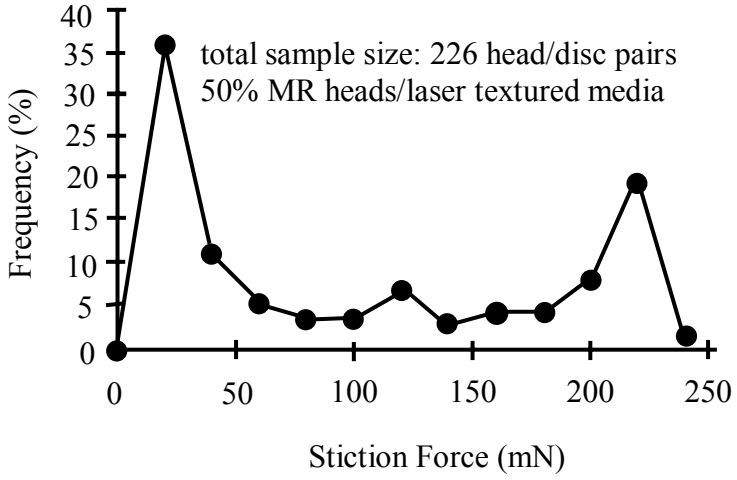

Figure 4.4 The bi-modal distribution of fly/stiction values. The forces were measured after 18-hour on-track flying in the data zone plus 2-hour rest dwell in the laser texture zone. Bump height = 20 nm, lube thickness = 2.5 nm. (Copy from Gui and Marchon[15], 1998).

forces. To prevent fly/stiction, one can try to make μ^3 less than 0.04577 by changing R, E', γ_{LV}, θ and H, which means carefully choosing the size of the crown on the head, the head/disk material, the lubricant, the shape and the height of the laser texture in the landing zone. Alternatively, one can try to control the amount of the liquid at the head-disc interface and let the volume vary in a safe region, say, beyond the high jump-on V_o'.

4.3 Evolution of the Interface Configuration for Controlled *H*

From Figure 4.1, one can see that when the interface condition lies below the corresponding jump-off condition, the interface assumes an equilibrium configuration without solid-solid contact. When the point lies above the corresponding jump-on condition, the interface assumes an equilibrium configuration with solid-solid contact. When the point lies in between the corresponding jump-on and jump-off conditions, the equilibrium configuration of the interface depends on the history of the interfacial evolvement; that is if the interface was out of contact before it reaches the point, it will remain out of contact whereas if the interface was in contact before it reaches the point, it will remain in contact. As the system condition moving along a certain path, the equilibrium configurations of the interface can then be easily found out by computing Γ, Ψ, Φ, using the methods shown in section 3.1 or 3.2. In order to see the evolution of the interface configuration, radius-approach curves, load-approach curves and the change of interface profiles are shown in Figures 4.5-4.11 for some cases with controlled *H*.

New dimensionless quantities are used to reflect the variations of corresponding dimensional quantities. The new dimensionless equilibrium wetted radius, $b_{eq}^{'}$ is defined as

$$b_{eq}^{'} = \frac{b_{eq}}{\left(\frac{R^2 \gamma_{LV} \left(\frac{\cos\theta_1 + \cos\theta_2}{2} \right)}{E^{'}} \right)^{1/3}} = b_{eq}^{*} \Gamma^{-1/6} \Psi^{2/3} \tag{4.3.1}$$

The new dimensionless equilibrium contact radius, $a_{eq}^{'}$ is defined as

$$a_{eq}^{'} = \frac{a_{eq}}{\left(\frac{R^2 \gamma_{LV} \left(\frac{\cos\theta_1 + \cos\theta_2}{2} \right)}{E^{'}} \right)^{1/3}} = a_{eq}^{*} \Gamma^{-1/6} \Psi^{2/3} \tag{4.3.2}$$

The new dimensionless adhesion force, $F_A^{'}$, is defined as

$$F_A^{'} = \frac{F_A}{2\pi R \gamma_{LV} (\cos\theta_1 + \cos\theta_2)} = \frac{1}{4\pi} \frac{\Psi}{\sqrt{\Gamma}} F_A^{*} \tag{4.3.3}$$

where

$$F_A^{*} = \frac{F_A}{E^{'} \sqrt{H V_o}} = b_{eq}^{*\,2} \Delta p_{eq}^{*} \int_0^1 2\pi r^{*} p^{*}(r) dr^{*} \tag{4.3.4}$$

The new dimensionless radial position, $r^{'}$, is defined as

$$r^{'} = \frac{r}{\left(\frac{R^2 \gamma_{LV} \left(\frac{\cos\theta_1 + \cos\theta_2)}{2} \right)}{E^{'}} \right)^{1/3}} = r^{*} b_{eq}^{*} \Gamma^{-1/6} \Psi^{2/3} \tag{4.3.5}$$

The new dimensionless gap, $h^{'}$, is defined as

$$h' = \frac{h}{\left(\frac{R\gamma_{LV}^2 \left(\frac{\cos\theta_1 + \cos\theta_2}{2} \right)^2}{E'^2} \right)^{1/3}} = h^* \left(\frac{\Psi}{\Gamma} \right)^{1/3} \tag{4.3.6}$$

These new dimensionless quantities are proportional to the corresponding dimensional ones.

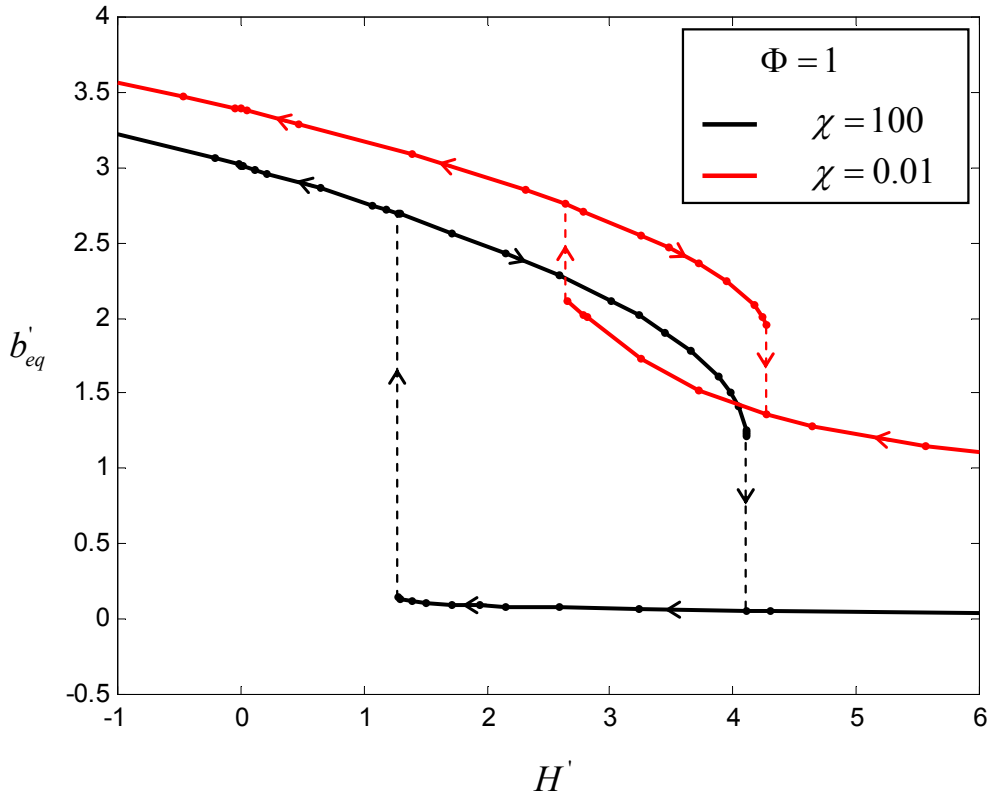

Figure 4.5 Effect of χ on the variation of wetted radius b'_{eq} with the original separation H'.

From Figures 4.5-4.8, one can see that the wetted radius and contact radius increase as the solid bodies approach. The load-approach curves in Figures 4.9-4.10 reaches a maximum tensile force at some positive $H^{'}$ and the tangents to the curves become vertical at jumps. Jumps and hystereses are clearly shown in the figures. Changing χ or Φ affects the jumps and the hystereses. For the cases shown in the figures, it can be seen that as χ or Φ decreases, the hystereses decrease, indicating less energy dissipation. However, to fully investigate the effect of χ and Φ, more cases need to be studied. This will be done in the future.

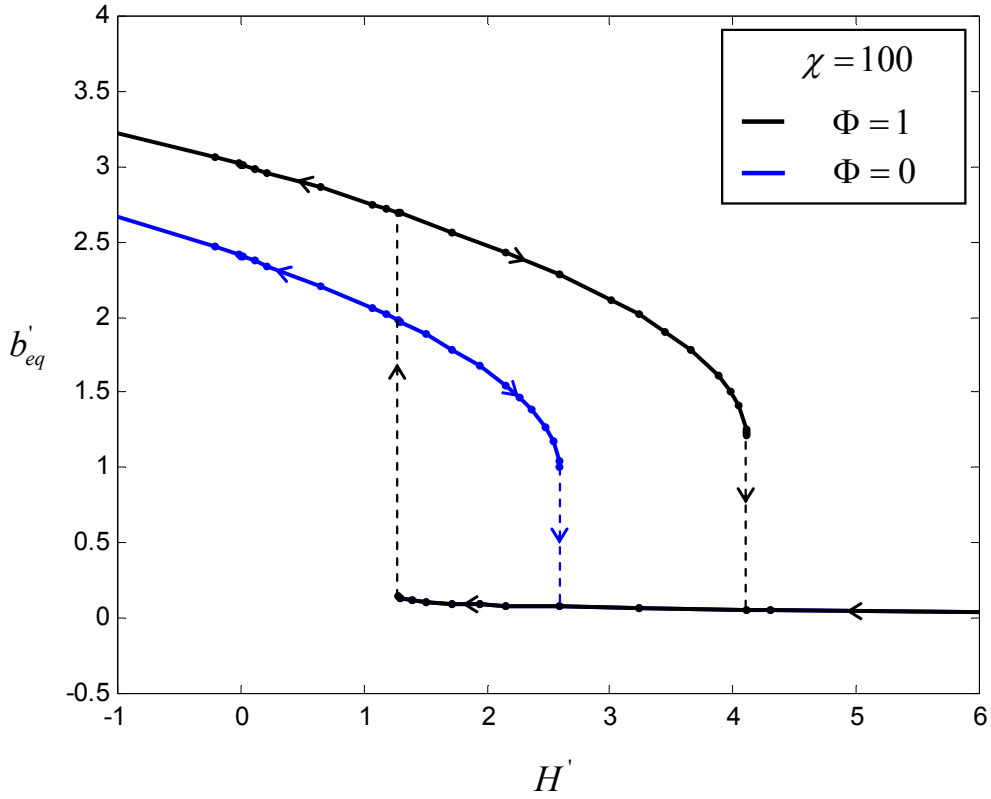

Figure 4.6 Effect of Φ on the variation of wetted radius $b_{eq}^{'}$ with the original separation $H^{'}$.

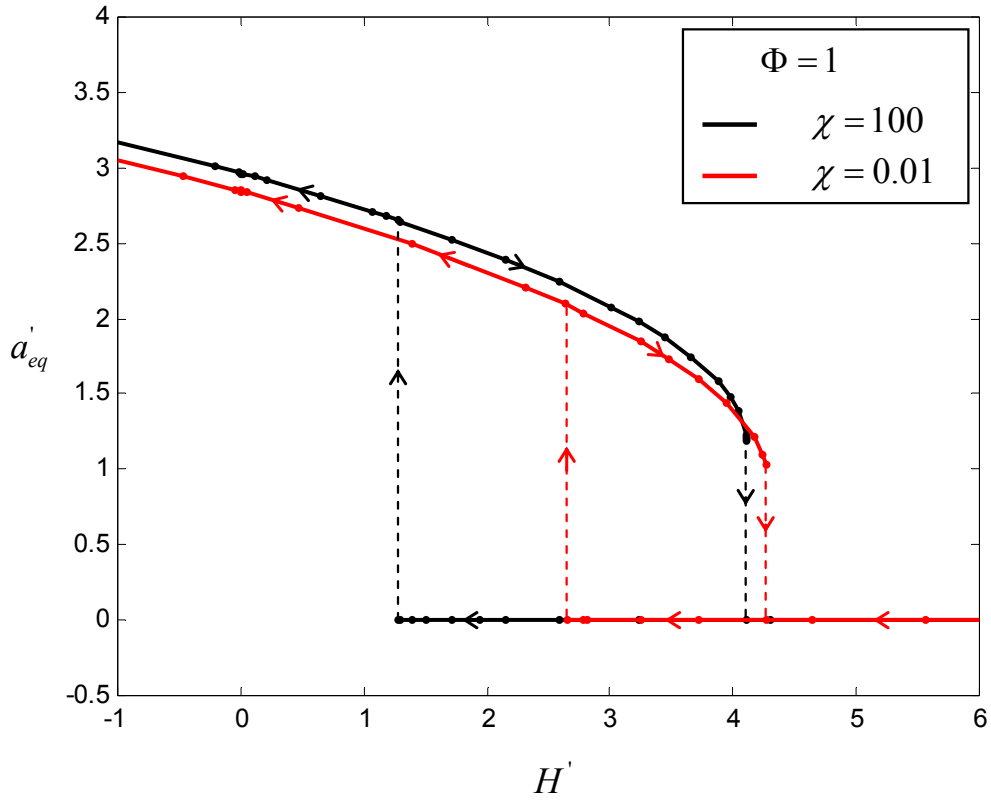

Figure 4.7 Effect of χ on the variation of contact radius a'_{eq} with the original separation H'.

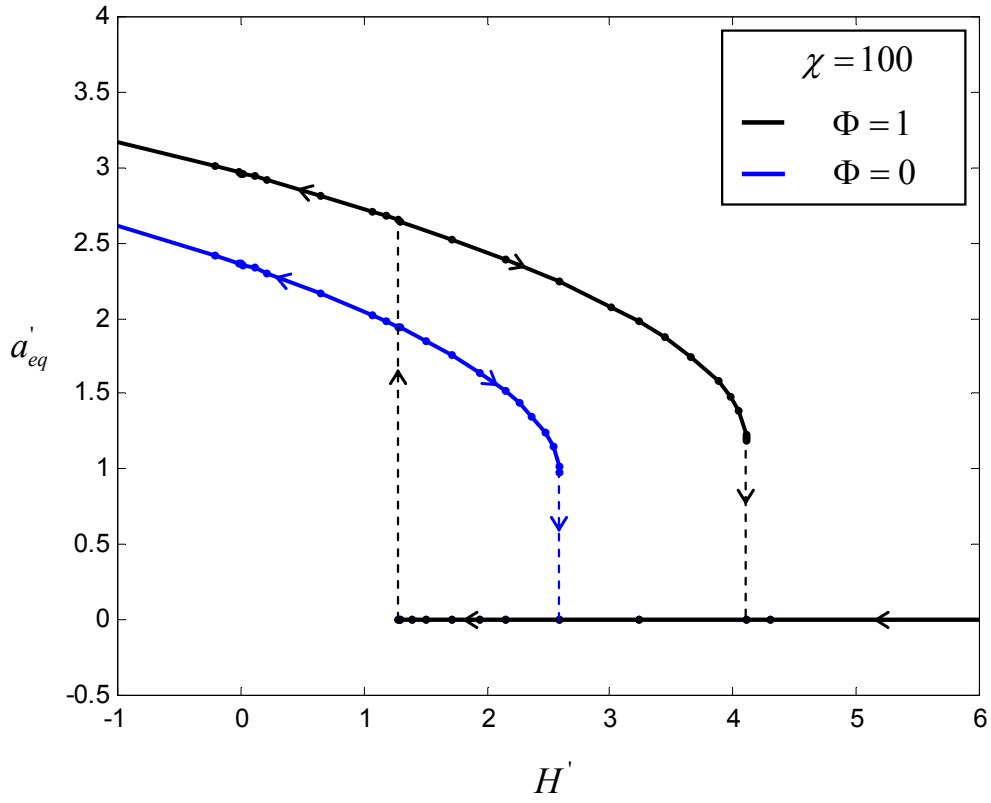

Figure 4.8 Effect of Φ on the variation of contact radius a'_{eq} with the original separation H'.

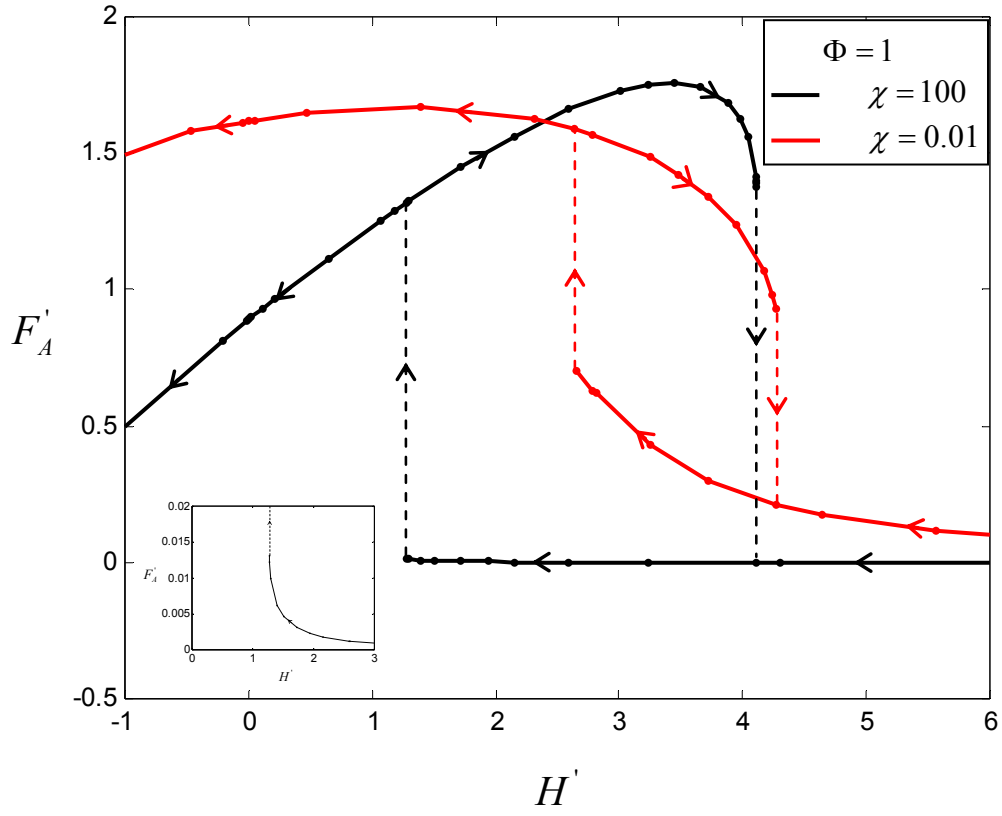

Figure 4.9 Effect of χ on the variation of adhesion force $F_A^{'}$ with the original separation $H^{'}$.

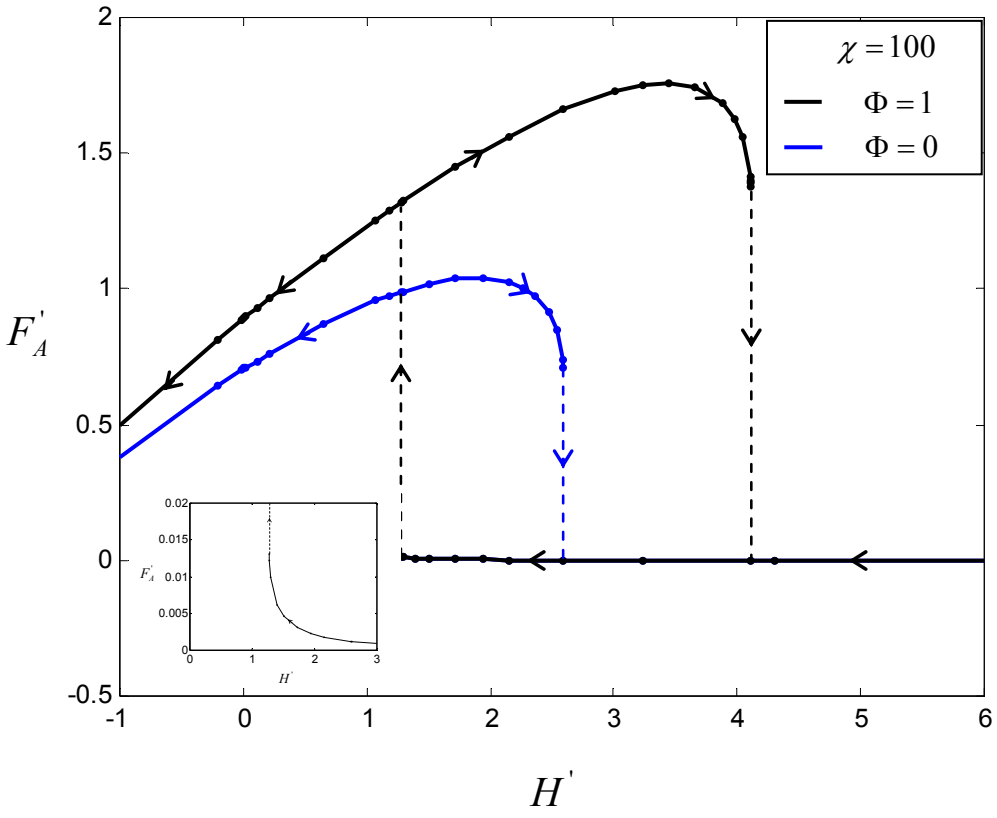

Figure 4.10 Effect of Φ on the variation of adhesion force $F_A^{'}$ with the original separation $H^{'}$.

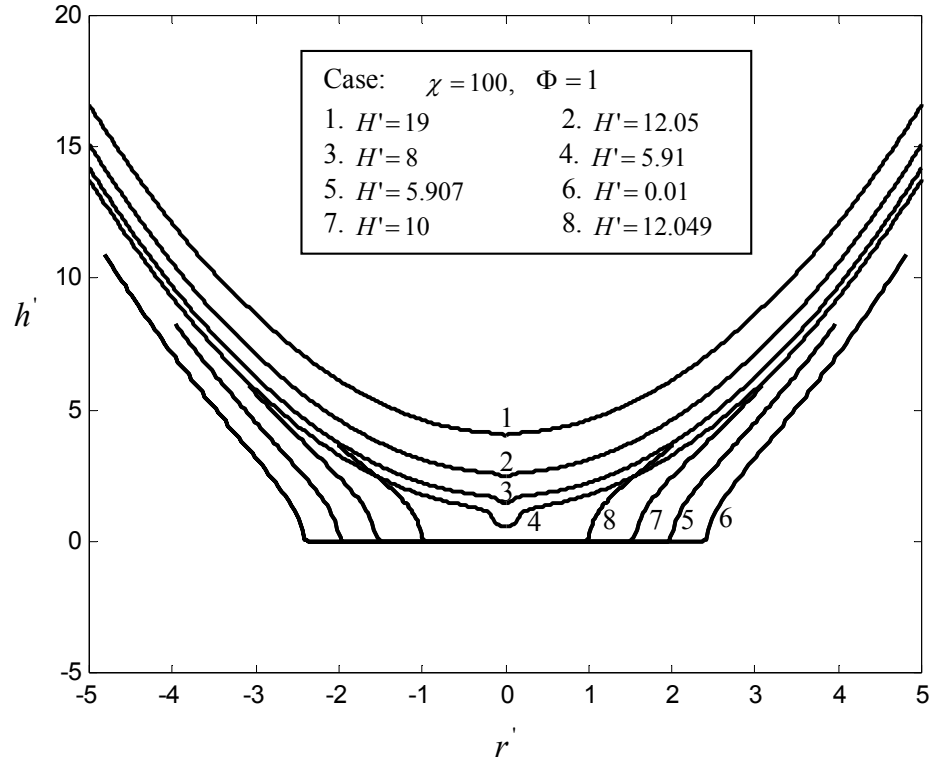

Figure 4.11 Evolution of the interface profile as the original separation H' changes.

4.4 Pull-off Force

The pull-off force is a measure of interfacial adhesion, and is sometimes called the force of adhesion. It is the adhesive force measured at the point of separation of two joined surfaces. It is also the maximum tensile force that the interface can sustain. In dry contact, there is no ambiguity about the separation of the solid bodies, which is the contact/non-contact transition. But in wet conditions, the concept of separation may cause confusion. As pointed out in section 4.2, for small liquid annuli the separation occurs

with the surfaces still flattened, therefore the separation of the solid bodies coincides with the contact/non-contact transition. However, for large menisci the surfaces get out of contact after a point contact configuration, but the liquid bridge remains, and the final jump-apart of the bodies corresponds to the instability of the liquid bridge. Clearly, it is not the contact/non-contact transition any more. Since the instability of the liquid bridge is not within the scope of this research, the contact/non-contact transition is always chosen as the separation of the solids in this study, and the pull-off force is defined as the equilibrium adhesive force achieved at the interface immediately before the surfaces get out of contact. This pull-off force may be different from that measured in experiments when the liquid meniscus is large and the jump-apart of the bodies is due to the collapse of the liquid bridge.

For a given set of condition of the interface, we can find the corresponding jump-off value of H and the equilibrium configuration a, b and Δp right before jump-off. The pressure distribution at this equilibrium can then be determined from equations (2.3.10)-(2.3.12) using the equilibrium parameters. And the pull-off force, F_p, can be computed from

$$F_p = \int_0^b 2\pi r p(r) dr \tag{4.4.1}$$

The dimensionless pull-off force, F_p^*, may be defined as

$$F_p^* = \frac{F_p}{E' \sqrt{H V_o}} = b_{eq}^{*\,2} \Delta p_{eq}^* \int_0^1 2\pi r^* p^*(r) dr^* \tag{4.4.2}$$

The dimensionless pull-off force can be computed for any given set of Φ and χ. In order to compare with others' results, an alternative method of scaling is adopted. The new dimensionless pull-off force is defined as

$$F_p^{'} = \frac{F_p}{2\pi R\gamma_{LV}(\cos\theta_1 + \cos\theta_2)} = \frac{1}{4\pi}\frac{\Psi}{\sqrt{\Gamma}} b_{eq}^{*\,2}\Delta p_{eq}^{*}\int_0^1 2\pi r^{*} p^{*}(r)dr^{*}$$
$$= \frac{1}{4\pi}\frac{\Psi}{\sqrt{\Gamma}} F_p^{*} \qquad (4.4.3)$$

where the value of Ψ and Γ can be computed from χ and the corresponding jump-off value of $H^{'}$. Figures 4.12 and 4.13 show the values of $F_p^{'}$ as a function of χ for $\Phi = 0$ and $\Phi = 1$, respectively. In order to see the effect of liquid volume, $F_p^{'}$ is plotted vs. $\chi^{-2/3}$.

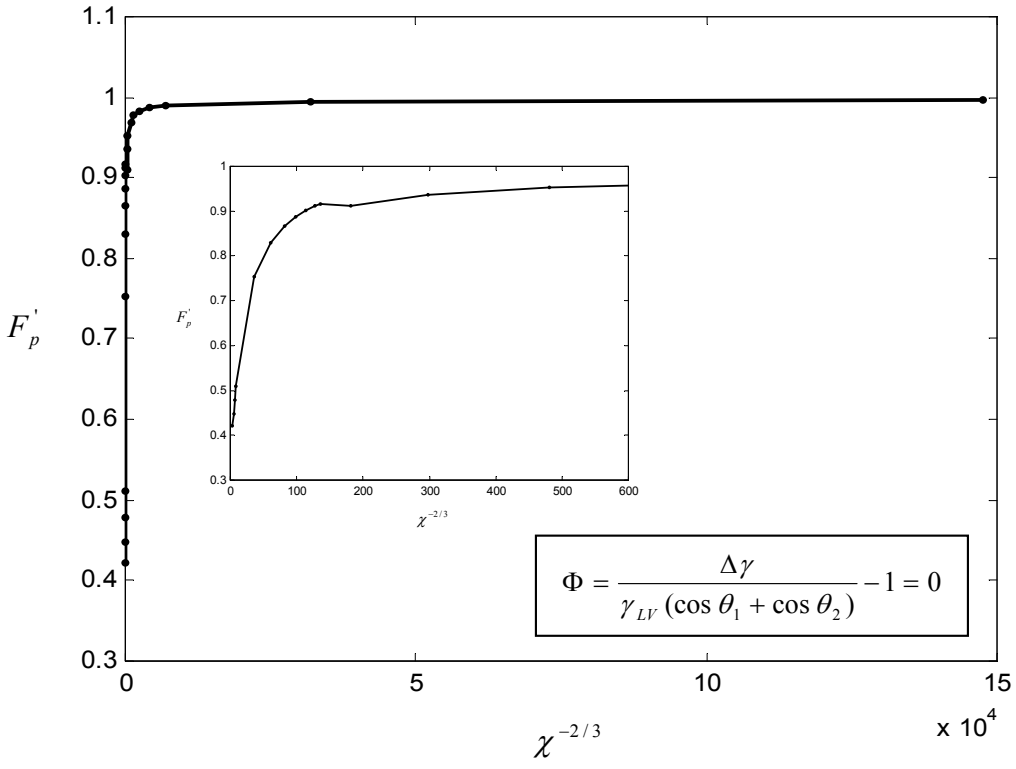

Figure 4.12 The dimensionless pull-off force, $F_p^{'}$, as a function of $\chi^{-2/3}$ for $\Phi = 0$. The inset is a zoom-in figure showing the variations $F_p^{'}$ at small $\chi^{-2/3}$.

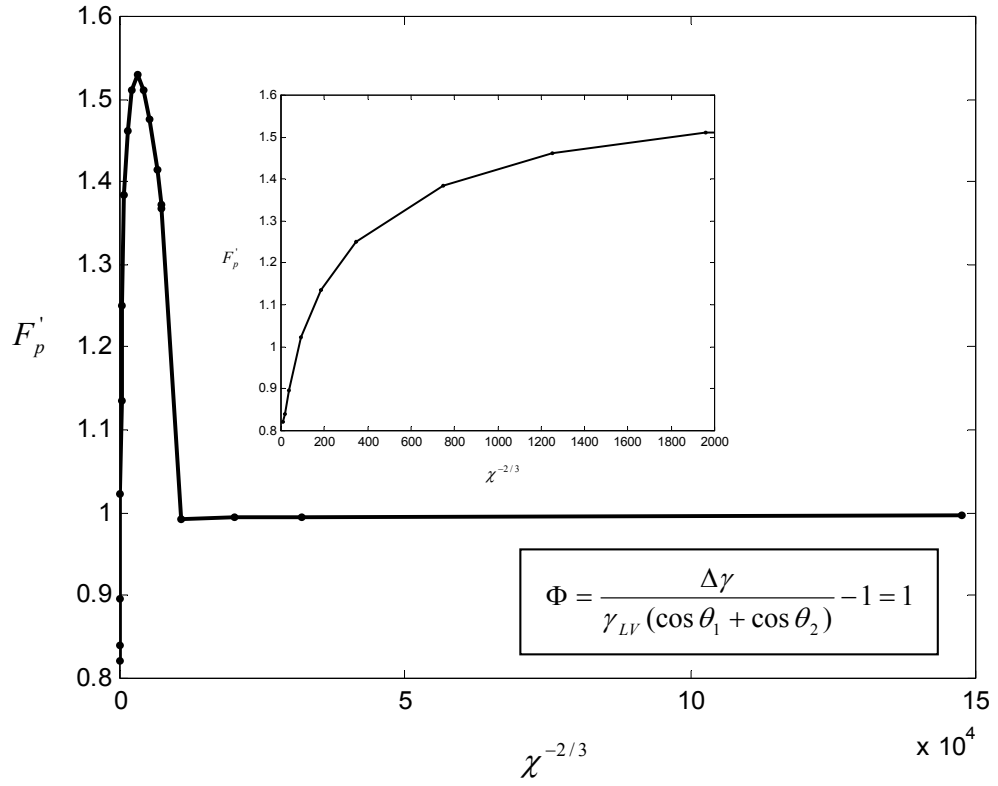

Figure 4.13 The dimensionless pull-off force, $F_p^{'}$, as a function of $\chi^{-2/3}$ for $\Phi = 1$. The inset is a zoom-in figure showing the variations $F_p^{'}$ at small $\chi^{-2/3}$.

From the figures it can be seen that when the liquid volume in the interface is large, $F_p^{'} = 1$, i.e., the pull-off force is equal to $2\pi R\gamma_{LV}(\cos\theta_1 + \cos\theta_2)$, which is the Laplace pressure force between two rigid bodies[48]. The contribution of the solid-solid interaction can be neglected; the capillary force completely determines the interfacial adhesion. When the liquid volume in the interface goes to zero, $F_p^{'}$ approaches 0.4221 for the case with $\Phi = 0$ and 0.8219 for the case with $\Phi = 1$. Thus the pull-off force is $0.8442\pi R\gamma_{LV}(\cos\theta_1 + \cos\theta_2)$ when $\Phi = 0$ and $1.6438\pi R\gamma_{LV}(\cos\theta_1 + \cos\theta_2)$ when $\Phi = 1$.

Recalling that $\gamma_{LV}(\cos\theta_1+\cos\theta_2)=\frac{\Delta\gamma}{(\Phi+1)}$, these results yield a pull-off force of $0.8442\pi R\Delta\gamma$ for $\Phi=0$ and $0.8219\pi R\Delta\gamma$ for $\Phi=1$. It is noted that the JKR model for dry contact predicts a pull-off force equal to $\frac{5}{6}\pi R\Delta\gamma$ in a fixed-grips analysis[24]. Considering the error in the calculation, the present values are very close to the JKR prediction. Therefore, one can say that, at dry contact, the pull-off force can be predicted by the JKR model. When $\Phi=0$, as the liquid volume increases, the pull-off force increases from the JKR prediction at dry contact limit to the Laplace pressure force for rigid spheres at large liquid volume regime. When $\Phi=1$, the pull-off force first increases then decreases with increasing liquid volume, but still approaches the JKR prediction at dry contact limit and the Laplace pressure force for rigid spheres at large liquid volume regime.

On the curves in Figures 4.12 and 4.13, there is a jump in F_p' at $\chi=1.84\times10^{-6}(\Phi+0.054)^{-2}$. This effect becomes clearer when Φ getting larger. This is a result of the sudden change of the contact radius at separation, because the surfaces jump out of contact from a finite contact area when $\chi>1.84\times10^{-6}(\Phi+0.054)^{-2}$ and go through a point contact when $\chi\le1.84\times10^{-6}(\Phi+0.054)^{-2}$.

Figure 4.14 show some experimental results of the pull-off forces between two crossed mica cylinders measured by Christenson[41]. In the figures, $F_p/4\pi R$ is plotted as a function of the relative vapor pressure. For the same liquid, according to Kelvin equation (equation 1.2), a higher relative vapor pressure means a larger Kelvin radius, r_K, and hence a larger liquid volume V_o. When the contact angles at the two surfaces are

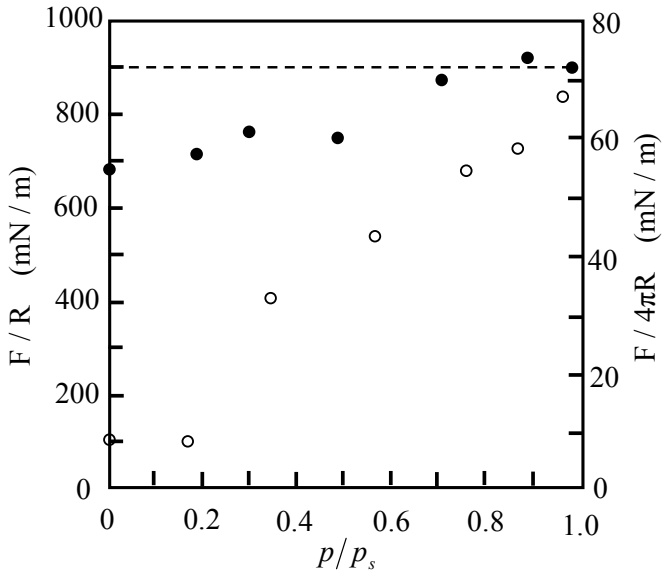

(a)

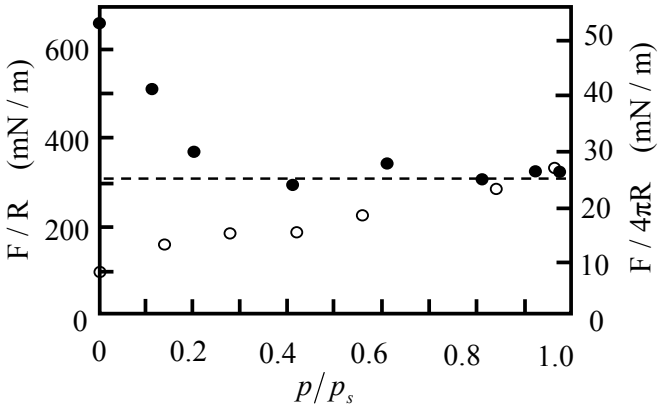

(b)

Figure 4.14 Measured pull-off force as a function of the relative vapor pressure. (a) Water with normal mica surfaces. (b) Cyclohexane. Open circles were obtained using a leaf spring and solid circles with a double cantilever spring. The dashed line corresponds to the bulk surface tension of water. The dashed line corresponds to the bulk surface tension of liquid (72 mN/m for water, 25 mN/m for cyclohexane). (copy from Christenson[41], 1988).

same, the rigid Laplace pressure force equals $4\pi R\gamma_{LV}\cos\theta$ where $\theta=\theta_1=\theta_2$. If the pull-off force equals to this rigid Laplace pressure force and the contact angle θ is close to zero (for the liquids in the experiments θ is less than 2°), $F_p/4\pi R$ gives the surface tension of the liquid, which is shown as a dashed line in the figures. The open circles in the figures are the forces measured with a leaf spring. The closed circles are the results of an experiment using a double cantilever spring, and are believed to be a better measurement of the pull-off force. The results in Figure 4.7(a) are for water with normal (potassium) mica surfaces, and the results in Figure 4.7(b) are for cyclohexane. It can be seen that for both liquids, in the large-liquid-volume regime as the relative pressure $p/p_s\to 1$, the pull-off force is as expected from the Laplace pressure in a capillary-condensed annulus around rigid surfaces. When normalized by $4\pi R$ (right-hand ordinate) it is only slightly larger than the bulk surface tension of the liquids. In dry contact at $p/p_s=0$, $F_p/4\pi R$ is around 55 mN/m in both Figure 4.7(a) and Figure 4.7(b), i.e., the measured pull-off force for dry contact is $F_p=220\pi R$ (mN). Since the JKR prediction for a fixed-load device, such as the surface force apparatus(SFA) used in this experiment, is $\frac{3}{2}\pi R\Delta\gamma$. Fitting the measured pull-off force with the JKR prediction gives a value of $\Delta\gamma$ around 146 mN/m for the mica surfaces. Therefore, the value of Φ for the system with water (Figure 4.7(a)) is close to zero, and the value of Φ for the system with cyclohexane (Figure 4.7(b)) is close to two. According our theory, the pull-off force for should increasingly approach the rigid Laplace pressure $4\pi R\gamma_{LV}\cos\theta$ the system with water, and decreasingly for the system with cyclohexane. The experiment data confirms these trends. So qualitatively the theoretical predictions are in good

agreement with the experiment results. Unfortunately, we cannot quantitively compare our fixed-grips prediction with the fixed-load experiment results. In order to do that, one has to plot the whole load-approach curve (F_p vs. H) to get the fixed-load predictions for various conditions. That will be done in the near future.

4.5 Conclusions

The approach and detachment processes of two elastic spheres in the presence of a liquid bridge were studied with the theory presented in Chapter III. Critical values of the control variables at jump-on and jump-off were found. The pull-off force was calculated as a measure of interfacial adhesion. The results were compared with existing experimental data on crossed mica cylinders. The following conclusions can be drawn:

1) The approach and detachment of the surfaces can practically be achieved by varying H or V_o.

2) In the cases where H is the only variable at the interface, when $\chi = \dfrac{\gamma_{LA}^2 \left(\dfrac{\cos\theta_1 + \cos\theta_2}{2} \right)^2 R^{5/2}}{E'^2 V_o^{3/2}} > 1.84 \times 10^{-6} \left(\Phi + 0.054 \right)^{-2}$, the interface jumps into and out of finite contact; when $\chi \le 1.84 \times 10^{-6} \left(\Phi + 0.054 \right)^{-2}$, the interface smoothly comes into and out of contact through a point contact.

3) The interface is the most susceptible to the jump-on instability at $\chi = 0.04577$.

4) For dry contact, the surfaces jump on at $H = 0$ and jump off at $H = 1.651\left(\frac{R\Delta\gamma^2}{E'^2}\right)^{1/3}$.

5) In the cases where V_o is the only variable at the interface, when $0.04577 \le \mu^3 < 1.872(\Phi + 0.0577)^{0.98}$, the interface may jump on with a low liquid volume or a high liquid volume. And this may be the reason for the bi-modal distribution of the fly/stiction force.

6) When $\mu^3 < 0.04577$, varying V_o will not cause the interface collapse, and thus fly/stiction can be prevented.

7) The pull-off force at the interface transitions from the JKR prediction ($\frac{5}{6}\pi R\Delta\gamma$) to the rigid Laplace pressure force ($2\pi R\gamma_{LV}(\cos\theta_1 + \cos\theta_2)$) as the liquid volume increases from zero to a large value.

8) The theoretical predictions of jump-on and jump-off displacements and pull-off force at dry-contact limit are in good agreement with JKR model.

CHAPTER V

CONCLUSIONS AND RECOMMENDATIONS

The interaction between two elastic bodies coupled via a small liquid bridge was investigated. Geometries of two half-spaces and two sphere contact were considered. Stable equilibrium configurations were determined, and the mechanical stability of the interface was examined. Jump-on and jump-off conditions were determined. The theory was then applied to study the approach and detachment processes of two elastic spheres in the presence of a liquid bridge. Critical values of the control variables at jump-on and jump-off were found. The pull-off force was calculated. The results provide valuable information on the fly/stiction phenomenon in HDI, and qualitatively agree with experimental results on crossed mica cylinders. From the analysis, the following conclusions and recommendations can be drawn:

1) The interaction between two elastic bodies coupled via a small liquid bridge is governed by three dimensionless parameters: $\Gamma = \dfrac{{\gamma_{LV}}^2 \left(\dfrac{\cos\theta_1 + \cos\theta_2}{2} \right)^2 V_o}{E'^2 |H|^5}$, $\Psi = \dfrac{V_o}{R|H|^2}$ and $\Phi = \dfrac{\Delta\gamma}{\gamma_{LV}(\cos\theta_1 + \cos\theta_2)} - 1$, or alternatively, by combinations of these three. For example, $\mu = \left(\dfrac{\Gamma}{\Psi} \right)^{1/3} = \left(\dfrac{R{\gamma_{LV}}^2 \left(\dfrac{\cos\theta_1 + \cos\theta_2}{2} \right)^2}{E'^2 |H|^3} \right)^{1/3}$ is often a convenient replacement to Γ.

2) For positive H, the size of the liquid bridge determines the manner by which the interface goes into and out of contact. When $\Psi < 33.25 + 1083.40\Phi + 9938.64\Phi^2$, the interface jumps into and out of finite contact, and the jumps are the origin of adhesion hysteresis; when $\Psi \geq 33.25 + 1083.40\Phi + 9938.64\Phi^2$, the interface comes into and out of contact smoothly through a point contact. When $\Gamma \geq 0.03007\Psi^{1.3955} + 0.01336$, the interface can only achieve stable equilibrium configuration with solid-solid contact; when $\Gamma \leq c_1(\Phi)\Psi^{2.4} + c_2(\Phi)\Psi$, the interface can only achieve stable equilibrium configuration without solid-solid contact; when $c_1(\Phi)\Psi^{2.4} + c_2(\Phi)\Psi < \Gamma < 0.03007\Psi^{1.3955} + 0.01336$, the equilibrium interface configuration depends on the history of the interfacial evolvement, i.e., if the interface was non-contacted before it reaches the current condition, it will remain non-contacted and if the interface was contacted before it reaches the current condition, it will remain contacted.

3) In the case of solid-solid contact, for given Ψ and Φ, the equilibrium contact radius continuously transitions from a pre-JKR radius at small values of Γ (large positive H) to a JKR radius at $\Gamma = \infty$ ($H = 0$) and then to a Hertz radius at $\Gamma = 0$ (large negative H). Increasing Ψ or decreasing Φ shrinks the near-JKR region, i.e., makes the pre-JKR radius and the Hertz radius appears at relative higher value of Γ (corresponding to smaller $|H|$). A similar transition exists in the contact profile.

4) The approach and detachment of the surfaces can practically be achieved by varying the rigid surface separation, H or the liquid volume, V_o. In the case of varying H, the interface is the most vulnerable to the jump-on instability at $\chi = 0.04577$. And for dry contact, the surfaces jump on at $H = 0$ and jump off at $H = 1.651\left(\frac{R\Delta\gamma^2}{E'^2}\right)^{1/3}$. In the

case of varying V_o, when $0.04577 \le \mu^3 < 1.872(\Phi + 0.0577)^{0.98}$, there are two critical values of V_o for jump-on and one critical value of V_o for jump-off; when $\mu^3 < 0.04577$, varying V_o will not cause the interface collapse.

5) The fly/stiction phenomenon can be related to the interface instability caused by the change of V_o, and should be prevented by choosing the size of the crown on the head, the head/disk material, the lubricant, the shape and the height of the laser texture in the landing zone to make μ^3 less than 0.04577, or by controlling the amount of the liquid in the head-disc interface to let the volume varying in a safe region beyond the high jump-on value of V_o.

6) The pull-off force at the interface changes from a JKR prediction at dry contact to a rigid Laplace pressure force at large liquid volume.

7) The theoretical predictions at the dry-contact limit are in good agreement with the JKR model.

This study represents a fundamental study of the interaction between two elastic bodies with an intervening liquid bridge. Surface roughness is not considered in the model even though it can play a significant role in adhesion. Nevertheless, the study may still have some practical value. For example, if the surface roughness is small compared to the nominal surface separation, its presence will not significantly alter the non-contact equilibrium state nor the jump-on condition. Only when the interface collapses, will asperity contact significantly influence the resulting adhesion forces and the jump-off condition. Meanwhile, one may apply the present theory to each liquid meniscus and asperity contact, and thus extend the theory to rough surface interaction.

Another issue that is not considered is the stability of liquid bridge. One can see from the Laplace-Young equation that when the radii of meniscus curvature are very small, the pressure drop across the meniscus can be very large. For example, water in a 100 nm gap will create 1.5 MPa pressure drop. In this case, the liquid in the bridge is under large negative pressure. Cavitation may occur at this situation, making the present analysis invalid. However, experiments on crossed mica cylinders[39] obtained small radii of meniscus curvature down to 1-2 nm without cavitation. The tested surfaces are atomic smooth and the liquid annulus is formed by condensation. Lacking of the heterogeneous nuclei may be the reason of the absence of cavitation. For rough surfaces and regular lubricants, the cavitation condition needs to be determined and incorporated into the theory.

In general, since many assumptions and simplifications were made in the analysis, the validity of the theory needs to be verified. Even though it has been shown that the theoretical results are qualitatively in agreement with some experimental data in the literature, direct quantitative comparison should be done in the future.

As a summary, the following future work is recommended:

1) Incorporation of the effect of surface roughness,
2) Incorporation of the stability of liquid bridge,
3) Experimental verification of the theory.

REFERENCES

1. Bhushan, B., (1996), "Tribology and mechanics of magnetic storage devices", Springer, New York.

2. Maboudin, R. and Howe, R. T., (1997), "Critical Review: Adhesion in Surface Micromechanical Structures", Journal of Vacuum Science and Technology B, Vol. 15, no. 1, pp. 1-20.

3. Maboudin, R., (1998), "Adhesion and Friction Issues Associated with Reliable Operation of MEMS", MRS Bulletin, Vol. 23, no. 6, pp. 47-51.

4. van Spengen, W. M., Puers, R. and De Wolf, I., (2003), "On the Physics of Stiction and its Impact on the Reliablity of Microstructures", J. Adhes. Sci. Technol, v 17, n 4, pp. 563-582.

5. Bowden, F. P. and Tabor, D., (1986), "The Friction and Lubrication of Solids", Claredon, Oxford.

6. Bhushan, B. and Dugger, M., (1990), "Liquid-Mediated Adhesion at the Thin-Film Magnetic Disk/Slider Interface", ASME Journal of Tribology, 112, pp. 217-223.

7. Li, Y. and Talke, F., (1990), "A model for the Effect of Humidity on Stiction of the Head/Disk Interface", Tribology and Mechanics of Magnetic Storage Systems, Vol. 7, pp. 79-84.

8. Tian, H., and Matsudaira, T., (1993), "The Role of Relative Humidity, Surface Roughness, and Liquid Build-up on the Static Friction Behavior of the Magnetic Head/Disk Interface", ASME Journal of Tribology, Vol. 115, pp. 28-35.

9. Gao, C., Tian, X. and Bhushan, B., (1995), Tribology Transactions, 38, pp. 201.

10. Gui, J., and Marchon, B., (1995), "A Stiction Model for a Head-Disk Interface of a Rigid Disk Drive", Journal of Applied Physics, Vol. 78, no. 6, pp.4206-4217.

11. van Spengen, W. M., Puers, R. and De Wolf, I., (2002), "A Physical Model to Predict Stiction in MEMS", Journal of Micromechanics and Microengineering, 12, pp. 702-713.

12. Mastrangelo, C. H. and Hsu, C. H., (1993), "Mechanical Stability and Adhesion of Microstructures under Capillary Forces – Part I: Basic Theory", Journal of Microelectromechanical Systems, Vol. 2, no. 1, pp. 33-43.

13. Mastrangelo, C. H. and Hsu, C. H., (1993), "Mechanical Stability and Adhesion of Microstructures under Capillary Forces – Part II: Experiments", Journal of Microelectromechanical Systems, Vol. 2, no. 1, pp. 44-55.

14. Mastrangelo, C. H., (1997), "Adhesion-related Failure Mechanisms in Micromechanical Devices", Tribology Letters, Vol. 3, no. 3, pp. 223-238.

15. Gui, J., and Marchon, B., (1998), "Fly/Stiction: Mechanical Instability of Head-Disk Interface", IEEE Transactions on Magnetics, Vol. 34, no. 4, pp.1804-1806.

16. Schouterden, K., Gillis, D., and Wolter, R., (2000), "Functional Collapse of Designed Surface Texture for Stiction Prevention in Storage Disk Drives", Tribology Transactions, Vol. 43, no. 3, pp. 559-563.

17. Guckel, H., and Burns, D. W., (1989), "Fabrication of Micromechanical Devices from Polysilicon Films with Smooth Surfaces", Sensors and Actuators, Vol. 20, pp. 117-122.

18. Arnold, V. I., (1986), "Catastrophe Theory", Springer-Verlag, New York.

19. Saunders, P. T., (1980), "An Introduction to Catastrophe Theory", Cambridge University Press, Cambridge.

20. El Naschie, M. S., (1990), "Stress, Stability, and Chaos in Structure Engineering: An energy Approach", McGraw-Hill, New York.

21. Fowler, D. E., Geiss, R. H., Eldridge, D. and Schreck, E., (1999), "Observation of Slider Droplet Formation during Fly Ftiction Tests with a Real Time Visualization Instrument", IEEE Transactions on Magnetics, Vol. 35, no. 5, pt. 1, pp. 2409-2411.

22. Zhao, Z. and Bhushan, B., (2001), "Studies of Fly Stiction", Proc. Inst. Mech. Eng. Part J J. Eng. Tribol., Vol. 215, no. 1, pp. 63-76.

23. Johnson, K. L., Kendall, K. and Roberts, A. D., (1971), "Surface Energy and the Contact of Elastic Solids", Proc. R. Soc. Lond, A 324, pp. 301-313.

24. Johnson, K. L., (1985), "Contact Mechanics", Cambridge University Press, New York.

25. Muller, V. M., Yuschenko, V. S. and Derjaguin, B. V., (1980), "On the Influence of Molecular Forces on the Deformation of an Elastic Sphere and Its Sticking to a Rigid Plane", Journal of Colloid Interface Science, 77, pp. 91-101.

26. Maugis, D., (1992), "Adhesion of Spheres: the JKR-DMT Transition Using a Dugdale Model", Journal of Colloid and Interface Science, Vol. 150, no. 1, pp. 243-269.

27. Pethica, J. B. and Sutton, A. P., (1988), "On the Stability of a Tip and Flat at Very Small Separations", Journal of Vacuum Science and Technology, A 6, pp. 2490-2498.

28. Smith, J. R., Bozzolo, G., Banerjea, A. and Ferrante, J., (1989), Physical Review Letter A 63, pp. 1269.

29. Maugis, D., (2000), “Contact, adhesion, and rupture of elastic solids”, Springer, Berlin; New York.

30. Attard, P. and Parker, J. L., (1992), "Deformation and Adhesion of Elastic Bodies in Contact", Physical Review A 46, pp. 7959-7971.

31. Attard, P., (2000), “Interaction and Deformation of Elastic Bodies: Origin of Adhesion Hysteresis”, Journal of Physical Chemistry B 104, pp. 10635-10641.

32. Greenwood, J. A., (1997), “Adhesion of Elastic Spheres”, Proc. R. Soc. Lond, A 453, pp. 1277-1297.

33. Tabor, D., (1977), “Surface Forces and Surface Interactions”, Journal of Colloid Interface Science, 58, pp. 2-13.

34. Feng, J. Q., (2000), “Contact Behavior of Spherical Elastic Particles: a Computational Study of Particle Adhesion and Deformations”, Colloids and Surfaces A 172, pp. 175-198.

35. Iooss, G. and Joseph, D. D., (1990), “Elementary Stability and Bifurcation Theory”, Springer-Verlag, New York.

36. Keller, H. B., (1997), “Numerical Solution of Bifurcation and Non-linear Eigenvalue Problems”, Applications of Bifurcation Theory: Proceedings of an Advanced Seminar, pp. 359-384, Rabinowitz, P. (Ed.), Academic Press, New York.

37. Keller, H. B., (1983), “The bordering algorithm and path following near singular points of high nullity”, SIAM J. Sci. Stat. Comput., Vol. 4, no. 4, pp. 573-582.

38. Ouyang, Q., Ishida, K. and Okada, K., (2001), “Investigation of Micro-Adhesion by Atomic Force Microscopy”, Applied Surface Science, Vol. 169-170, pp. 644-648.

39. Fisher, L. R. and Israelachvili, J. N., (1981), “Direct Measurement of the Effect of Meniscus Forces on Adhesion: a Study o f the Applicability of Macroscopic Thermodynamics to Microscopic Liquid Interfaces”, Colloids and Surfaces 3, pp. 303-319.

40. Christenson, H. K., (1985), “Capillary Condensation in Systems of Immiscible Liquids”, Journal of Colloid and Interface Science, Vol. 104, no. 1, pp. 234-249.

41. Christenson, H. K., (1988), “Adhesion between Surfaces in Undersaturated Vapors—A Reexamination of the Influence of Meniscus Curvature and Surface Forces”, Journal of Colloid and Interface Science, Vol. 121, no. 1, pp. 170-178.

42. Fogden, A. and White, L. R., (1990), “Contact Elasticity in the Presence of Capillary Condensation I. the Nonadhesive Hertz Problem”, Journal of Colloid and Interface Science, Vol. 138, no. 2, pp. 414-430.

43. Maugis, D. and Gauthier-Manuel, B., (1994), "JKR-DMT Transition in the Presence of a Liquid Meniscus", Journal of Adhesion Science and Technology, Vol. 8, no. 11, pp. 1311-1322.

44. Adamson, A. W., (1976), "Physical Chemistry of Surfaces", John Wiley & Sons, New York.

45. Makhovskaya, Yu. Yu. and Goryacheva, I. G., (1999), "The Combined Effect of Capillarity and Elasticity in Contact", Tribology International, Vol. 32, pp. 507-515.

46. Atkins, P. W., (1990), "Physical Chemistry", W. H. Freeman & Co., New York.

47. Black, W. Z. and Hartley, (1996), "Thermodynamics", 3rd edn., English/SI Version, HarperCollins, New York.

48. Israelachvili, J., (1991), "Intermolecular & Surface Forces", Academic Press, San Diego.

49. Chapra, S. C. and Canale, R. P., (2002), "Numerical Methods for Engineers", 4th edn., McGraw-Hill, New York.

50. Horn, R.G., Israelachvili, J. N. and Pribac, F., (1986), "Measurement of the Deformation and Adhesion of Solid in Contact", Journal of Colloid and Interface Science, Vol. 115, no. 2, pp. 480-492.

51. Derjaguin, B.V., Muller, V. M. and Toporov, Y. P., (1975), "Effect of Contact Deformations on the Adhesion of Particles", Journal of Colloid and Interface Science, Vol. 53, pp. 314-326.